UC San Diego

UC San Diego Electronic Theses and Dissertations

Title

Novel role for iron in modulating organismal metabolism and host defense during enteric infection

Permalink

https://escholarship.org/uc/item/21m3d85d

Author

Romero, Alicia Raquel

Publication Date

2022

Peer reviewed|Thesis/dissertation

eScholarship.org Powered by the California Digital Library
University of California

UNIVERSITY OF CALIFORNIA SAN DIEGO

Novel role for iron in modulating organismal metabolism and host defense during enteric infection

A dissertation submitted in partial satisfaction of the
requirements for the degree Doctor of Philosophy

in

Biology

by

Alicia Raquel Romero

Committee in charge:

Professor Janelle Ayres, Chair
Professor Randolph Hampton
Professor Stephen Hedrick
Professor Manuela Raffatellu
Professor Gerald Shadel

2022

Copyright
Alicia Raquel Romero, 2022
All rights reserved.

The Dissertation of Alicia Raquel Romero is approved, and it is acceptable in quality and form for publication on microfilm and electronically.

University of California San Diego

2022

EPIGRAPH

“But man is a part of nature, and a war against nature is a war against himself”

Silent Spring 1962

Rachel Carson

DEDICATION

This work is dedicated to my grandmother Amparo Ramirez (1931-2012)—mother to eleven first generation American children, and an ingenious and tenacious scientist of everyday life.

TABLE OF CONTENTS

LIST OF FIGURES

ACKNOWLEDGEMENTS

First, I would like to express my sincere gratitude to my mentor, Janelle Ayres. I am continually inspired by your ingenuity and pioneering spirit in science and it has been a pleasure to train at your side as the foundation of my career in science. I hope to bring your relentless pioneer spirit to my future endeavors in science and incorporate your transformative perspective into how I approach the fields of health and disease from here on out. I am grateful not only for the “food” but also for the proverbial “plate”—by this I mean, the methods by which the lessons were served. I appreciate the challenges and opportunities that I was given in your lab and for your patience and continued support by every means of the word.

I would like to thank all current and former members of the Ayres Lab who, whether or not they realize it, have contributed to my growth and journey in science: Sheila, Grischa, Katia, Vic, Andre, Justin, Dani, Sarah, Jose, Sara, Ari, Abby, Natalia, Robert, Alex, Sam, Michelle. To my various bay-mates: Abby, Justin, Dani, Robert, Sam— I thank you for the insightful discussions, the useless discussions, and the occasional snack sessions. I would like to thank Karina, who was never allowed to be my bay-mate for fear that we would make the lab an obnoxiously fun zone—thank you for the unforgettable hours spent in lab and money spent at UTC. You are the main character of the Ayres Lab and we would all be useless without your attention to detail and relentless perfectionism in lab. To Sam, my cohort buddy, for embarking on journeys in the lab and in the ocean with me (and for always reminding me when BGSE was). To Robert, my runner-turned-swimmer buddy, for enriching chats and for the energizing atmosphere that surrounds you everywhere you go. To Alex, for thinking of the most outrageous questions and even more outrageous solutions to the

problems of the world and the “smaller” ones in lab. No stone left unturned, no topic too taboo for us to tackle. To Sheila, for embodying the best aspects of science and never taking a joke too seriously. You’re the coolest square I will ever know. Grischa, there is no sound more satisfying than your laugh because it’s so unexpected, and it became my mission to make you laugh—unfortunately, it was not often enough. Thank you for your wisdom as the resident microbiologist. To Katia, for the stone cold dedication to science and skincare. I thank you for making sure I started tretinoin at a young age. To Justin, for always asking for a daily report of what I am doing with my life and a corresponding insight to move said life forward. I admire your Canadian spirit and your immunity to “hours-at-the-bench-back pain” (also, my favorite era of lab was when we had a minifridge stocked with *La Croix*). To Andre, the resident bioinformatician who was the most polite (and remote) member of the Ayres Lab yet. Thank you for the chalk talks and crossing the sea for us.

I would like to thank members of the Evan’s Lab: Sihao, Eman, Ming, Gencer, and Hunter. Eman, I appreciate your cynical spirit that was only matched by mine on my worst days. You told me the hard painful truths of graduate school alongside the perks. To Ming, for making me feel like a celebrity for bringing microwave burritos for lunch. To Sihao, for dropping whatever you were doing (*no matter what it was*) to answer my questions about anything—whether it was finance, mTOR, high fat diets or metabolic software. I hope to embody half your zeal for research and recall ability in my future endeavors.

I would like to thank my committee members: Manuela, Steve, Randy, and Gerry—for always, *eventually*, responding to my emails and asking the difficult questions that haunt my dreams. I will always admire your ability to digest intricate and eclectic science as easily

as I digest my news feed. One day, I will be in your shoes, and I hope to have half as much patience, grace, and wisdom.

I would like to thank the countless staff at Salk who ensured operations ran smoothly day in and day out. Science would be impossible without your deliveries, cleaning and upkeep, animal support, mechanical and technical support, and safety protocols. The IT team at Salk is truly unmatched. Also, Salk events with free food and beverages were a welcome form of emotional and mental sustenance on my longest days.

Everyone's path has defining characters and experiences that shape and propel the journey forward. The first character to support my career in research was Dr. Harber at Oxnard College, who I am still in touch with today and expect I always will be. I can never thank you enough for your support and guidance throughout this journey. My second research experience was as part of the Amgen Scholars Summer Research Program at Stanford in 2014, and this was a phenomenal program and learning experience. I thank the coordinators, Samar and Terrance, and members of the Relman Lab (Eitan, David, Elise, Rob) for welcoming me into your lab for 10 weeks and introducing me to academia. As part of this program, I made lifelong connections with the brilliant young scientists of the Kairos house. I would like to thank the Cal Poly San Luis Obispo chapter of Alpha Chi Sigma for enabling authentic lifelong friendships with centered around enthusiasm for science, service, and chemistry. I was also graciously admitted into the PREP program at UC Santa Cruz where I was introduced into a brand new field of structural/RNA biology with the Jurica Lab: Melissa, Beth, Andrew, Mayra, Veronica. Finally, I would like to thank my coaches in swim

and water polo for the invaluable time spent dedicated to excellence in the pool and for never settling for less than my best: Kyle Kopp, Coach Baratte, and Travis Dasnoit.

I would like to thank my support network throughout grad school and beyond: My family, friends and my partner, Ben. My “2016 cohort crew”: Kaito, Jenny, Bianca—the last surviving group chat of our graduate school career. That is a considerable milestone alone *and* I was also invited to all 3 of your weddings—I consider this to be a monumental feat and I am proud of us for making it this far. Bianca, you’ve been my resident next-door lab neighbor, parttime therapist, and fulltime friend. You always brighten my day and laugh at my jokes, I can never thank you enough for making me feel like I should have a Netflix special. Jenny, for being the world’s chilliest roommate and the most balanced grad student I’ve met yet. To Kaito, it’s difficult to condense all the ways you’ve enriched my life and my research, and for this, I can never thank you enough. To my lifeguard friend Jake, for brightening the last chapter of graduate school with a fresh perspective outside of science. To my dearest lifelong friend Abbie—a kindred spirit who’s always a call away to discuss any trivial or monumental issue. To my family: Mom, dad, Marissa and Kamille. You’ve kept me grounded as a reminder of “how far I’ve come” and also laugh at my jokes when I come home. Kamille, my personality twin who is trailing a decade behind me yet living with 10 years greater wisdom than me. Marissa, for showing us that you can get 100k subscribers on YouTube faster than I can get a PhD—but in all seriousness, you are a heavy hitter and barriers don’t stand a chance against you. To my dad, for teaching me how to “play the game” and making sure my Mazda was always okay. And to my mother, who bought me the cool science toys, made sure I did my homework, and made sure I went after my dreams—among a million other things.

To Ben, my everything else. We met at Stanford “science camp” in 2014, have earned two degrees, raised Miko, maintained 3 years’ worth of long-distance love, and lived through the formidable year of 2020 together. I am eternally grateful for you, and your endless love and encouragement. You’ve been my #1 fan all these years and are the most brilliant and dedicated scientist I’ve ever known. You told me not to “waste any time” writing about you so I’ll end it here with this: you enrich my life and therefore enrich my science. And to Miko—my pandemic kitty who has completely changed my opinion of “dogs are a man’s best friend”…

As I write this, I am struck by two conflicting urges: finishing this document and continuing to embellish it. The endlessness of science is what makes it simultaneously bearable and unbearable. There is always more to do, ways to improve, questions to ask, and lenses to examine data with. Every essential experiment completed spurs ten more crucial ones. We are relieved to move on from a problem but only as a means to continue on to a new one. However, scientists seem to be alleviated only by the endless nature of the unknown. For this insight, I would like to thank Mrs. Cottingame, my middle-school science teacher who arguably spoke the most influential words to me in my life: “Never stop asking questions”. For each of us has unique questions and perspectives to contribute to a world that would be bland without them.

Chapter 2 is largely adapted from the material as it appears in Romero, A.R., Mu, A., Ayres, J.S., Adipose triglyceride lipase mediates lipolysis and lipid mobilization in response to iron-mediated negative energy balance, *iScience* (2022), doi: https://doi.org/10.1016/j.isci.2022.103941. The dissertation author was the primary investigator and first author of this manuscript. The authors would like to thank Dr. Sihao Liu, Dr. Gencer Sancar, and Dr. Emmanuel Gasser (Evans Lab at Salk) for excellent methodical assistance, stimulating and insightful discussion, and generosity; Kaito Kikuchi (Suel Lab at UCSD) for providing guidance and assistance for analyses of metabolic data; Daniela Michel-Romo for providing technical support in a pair fed animal study, and Caroline Gordon for reliable assistance with animal husbandry. Finally, the authors offer thanks to members of the Ayres Laboratory for helpful discussion and technical assistance as needed. This work was supported by an NIH awards DP1 AI144249 and R01AI114929 (JSA), and the NOMIS Foundation (JSA).

Chapter 3 is currently being prepared for submission for publication of the material in the working citation: Romero, A.R., Gerner, R.G., Ayres, J.S., Iron-induced metabolic rearrangements uncouple hallmarks of infectious colitis. The dissertation author was a primary investigator and the first author of this material. The authors would like to thank Dr. Justin McCarville and Dr. Grischa Chen (Ayres Lab) for thoughtful discussions and Zbignew and Kasia at La Jolla Institute of Immunology for technical guidance with histology.

VITA

2012 - 2015 B.S. in Microbiology, California Polytechnic State University San Luis Obispo

2016 - 2022 Ph.D. in Biology, University of California San Diego

Thesis advisor: Janelle Ayres (Salk Institute for Biological Studies)

PUBLICATION

Romero, A.R., Mu, A., Ayres, J.S., Adipose triglyceride lipase mediates lipolysis and lipid mobilization in response to iron-mediated negative energy balance, *iScience* (2022), doi: https://doi.org/10.1016/j.isci.2022.103941.

MANUSCRIPT IN PREPARATION

Romero, A.R., Gerner, R.R., Ayres, J.S.. Iron-induced metabolic rearrangements uncouple hallmarks of infectious colitis. *Manuscript in preparation*

ABSTRACT OF THE DISSERTATION

Novel role for iron in modulating organismal metabolism
and host defense during enteric infection

by

Alicia Raquel Romero

Doctor of Philosophy in Biology

University of California San Diego, 2022

Professor Janelle Ayres, Chair

Mammalian metabolism and physiology are central to all aspects of health and disease. However, disruptions to homeostasis are more often the hallmarks of disease. Thus, aberrant metabolic states and physiological conditions are considered to be maladaptive and are overlooked for their role in host defense and the coevolution with microbes and pathogenic threats. Having co-evolved alongside microbes, it should be no surprise that hosts have evolved defense mechanisms founded in metabolic and physiological systems alongside our immune system. Here, we explore a novel role of the

essential micronutrient iron which plays a dual role at the interface of infection and physiology.

This thesis dissertation describes original work that examines how excess dietary iron modulates organismal energy balance through interfering with nutrient absorption. We found that negative energy balance in our model drives profound wasting of fat and lean energy depots and that iron-induced fat wasting protects lean energy stores from severe wasting in response to negative energy balance. Quite serendipitously, we found that iron supplementation alone, and iron-induced metabolic alterations mediate beneficial effects through two independent mechanisms in the context of infection. First, we found that dietary iron supplementation promotes resistance defenses during *Citrobacter rodentium* infection—which conflicts with the traditional role for iron defined by nutritional immunity. Iron-induced resistance prevented canonical colonic pathogenesis marked by region-specific expansion, induction of the innate inflammatory cascade and colitis. However, we found that the traditional hallmarks of *C. rodentium*-induced colitis that were previously assumed to correspond with inflammation emerge via two distinct stages of infection. Iron diet prevented expansion of *C. rodentium* and ensuing inflammatory cascades that are required to cause colon pathology. However, we found that iron-induced fat wasting and lipolysis is necessary to prevent non-inflammatory colon remodeling that occurs upon colonization with *C. rodentium.* Thus, we have identified a novel role for iron in promoting resistance defenses and modulating pathology. This work expands on the collective understanding of iron's role in physiology and host defenses—providing mechanistic evidence to implicate iron in modulating a novel adipose-gut axis.

Chapter 1: Introduction

1.1 Organismal physiology and metabolism in host defense

Infectious disease represents one of the greatest selective pressures that has influenced the evolution of eukaryotic organisms. The most palpable outcome being the evolution of the immune system, which functions to recognize and respond to pathogenic threats in order to promote organismal fitness. As such, the immune system has been the central focus of a century of work dedicated to understanding the mechanisms and functions of host defense against pathogens [1]. Though the classical image of host defense is coupled with immune machinery and associated products of the immune system, the landscape in which immunity surveys, signals and operates is often overlooked in the importance of host defense. This perspective of host defense is pervasive in our understanding of health and disease mechanisms, and has supported the idea that in order to avoid disease and stay healthy, we need only to eliminate pathogenic threats [2,3]. This perspective is easily challenged when considering symbiotic relationships that have evolved between hosts and microbes, the deleterious effects of mounting an inflammatory response, or the phenomena of lethal dose 50 (LD_{50})—which describes the dose of an agent that is lethal to 50% of a population [3,4] . Thus, it is crucial to consider the multifaceted nature of host defense strategies that extend beyond the immune system and the one dimensional relationship between host and invading pathogen.

In adopting a multifaceted view of host defense strategies, evolutionary relationships help inform the nature of a defense strategy. For example, the Red Queen Effect describes oscillating defensive traits in host and pathogen populations over time [2,5]. This “evolutionary arms race” is observed for traits that promote fitness of one party that negatively impact the fitness of the other party— essentially driving continuous selection of “counterstrategies” [6].

Defensive strategies of a host are collectively referred to as antagonistic defenses. While the immune system and its innate and adaptive effectors orchestrate a large portion of antagonistic defenses, there are substantial behavioral and physiological mechanisms of antagonistic defense. For example, avoidance behaviors or physiological resistance that limit pathogen fitness (like altering the pH of a pathogen's niche) drive selection of pathogen traits that can overcome these fitness barriers.

On the other hand, a fixation of traits can arise in host and pathogen populations as well. Cooperative defenses encompass traits that promote fitness of one party while having a neutral to positive impact on the fitness of the other party [2]. Thus, cooperative defenses promote host fitness by limiting the damage incurred through an infection without negatively affecting the pathogen's fitness. Because the virulence of an infectious disease is dependent on host and pathogen-derived factors, hosts employ anti-virulence defenses on these two fronts. For instance, host proinflammatory responses and pathogen-encoded virulence factors can inflict severe tissue damage while having no effect on pathogen fitness. Thus, hosts can mitigate disease severity by dampening the virulence of infection through detoxification, neutralization or reducing sensitivity to these factors. These strategies are collectively referred to as anti-virulence defenses. Alternatively, hosts can employ physiological tolerance mechanisms that function to promote maintenance and growth of tissues during disease. For example, maintenance of barrier integrity during gastrointestinal infections prevents extraintestinal dissemination of gut microbiota and supports nutrient uptake—presumably without compromising pathogen fitness. Thus, traits that do not impact the fitness of pathogens (or the host) are predicted to go into fixation in the host population if there is a continued relationship with the pathogen over time [2,3,7] . The emergence of

symbiotic relationships with microbiota is a prime example of cooperative defenses, because the host is not ignorant of their existence nor does it actively eliminate them. Hosts have evolved mechanisms to maintain a niche for commensals an in turn, microbes have evolved to promote our fitness and continue occupying this niche [4].

Significance of metabolic responses during infection

During infection, host and pathogen are subject to increased metabolic demands. More recently, the intersection between the immune system and metabolism has gained traction as a substantial component of immunity and host defense strategies as a whole. The emergence of immunometabolism in the past decade has aimed to describe how the function and metabolism of immune cells is interconnected and define mechanisms of cellular immune metabolism and associated outcomes in health and disease. One well-known principle that has emerged from immunometabolism is the *Warburg effect*—in which glycolytic metabolism is associated with inflammatory effectors functions like cytokine production in inflammatory macrophages and T cells, whereas immune-suppressive macrophages and regulatory T cells exhibit increased oxidative metabolism of lipids [8,9]. However, this principle has since been challenged [10] and corresponding predictions for disease outcomes are context dependent [9,11]. For instance, glycolytic metabolism that enhances inflammation can also incur deleterious costs to the host, like cardiomyopathy during polymicrobial sepsis [12]. Microbial glycolysis itself can promote virulence and many severe systemic infections are associated with a pro-lipolytic state [3,11,13]. In fact, the most deterministic metabolic pathways associated with mortality outcomes in septic intensive care unit patients are glucose, fatty acid and beta-oxidation pathways—highlighting the overwhelming importance of metabolic adaptations in host defense [14]. Nonetheless, cellular

immunometabolic-based approaches have inherent therapeutic value and have been adopted clinically to treat infectious and autoimmune diseases[15].

Though much focus has been paid to metabolism of immune cells, more recent investigations have described a role for behavioral and physiological responses in host defense. For example, sickness-induced behaviors, like anorexia and lethargy, are conserved responses to infection that alter systemic metabolism and can promote fitness of host under certain contexts. Anorexia promotes gluconeogenesis which is beneficial during systemic bacterial infections [16,17]. On the other hand, anorexia is a maladaptive response in murine *Salmonella* infection and promotes systemic extraintestinal infection and mortality[18]. However, increased host mortality also reduces the fitness of *Salmonella* by reducing transmissibility to new hosts—a phenomena referred to as the *virulence-transmission tradeoff*. This has presumably driven the evolution of *Salmonella*-encoded effector SlrP, which inhibits caspase-1 dependent activation of IL-1β and subsequent induction of the anorexic response[18]. In this context, anorexia is as a mutually antagonistic force that has aided in the selection of a cooperative pathogen trait. Importantly, while SlrP reduces mortality in infected individuals by inhibiting anorexia, anorexia itself is a way to promote fitness of the host population as a whole by limiting the transmission of *Salmonella* to naïve hosts.

Thermoregulation is of course, another highly conserved physiological strategy hosts employ to promote resistance or dampen virulence during infection [19]. Infected mammals for instance, produce heat shock factor 1 (HSF-1) during fever responses in order to reduce

tissue damage and organ dysfunction incurred by proinflammatory cytokines, representing an inducible host anti-virulence mechanism [20].

In the context of organismal energy balance, proper maintenance and mobilization of energy stores in the body are crucial to host defense [21]. Body mass index shows that low and high body mass index (BMI) are associated with increased susceptibility to infectious and non-infectious disease [22]. Along these same lines, malnutrition and metabolic diseases also promote susceptibility to certain infectious diseases. Of course, this is due in part to dysfunction of the immune system, but also extends to dysfunctional metabolic adaptations on the organismal scale [23]. For instance, organismal catabolism is a conserved response to infection that leads to wasting of lean and fat energy stores [24]. And while wasting is a highly conserved response, current evidence and clinical data suggest that wasting decreases host survival and impairs recovery from severe infections—raising the question of how wasting can confer a benefit and promote host health [25,26]. At rest, skeletal muscle accounts for 40% of total body mass and 30% of total energy expenditure [27]. Therefore, it is conceivable that in the case of muscle wasting, reducing “auxiliary” energy expenditure or providing amino acids to critical organs and systems could accommodate increased energetic demands during infection. Alas, there is little evidence to support this hypothesis (as it is understandably difficult to test experimentally), and there is substantial evidence highlighting the importance of maintaining muscle mass during infection.

It was recently demonstrated that in *Drosophila* and Zebrafish, muscles promote resistance defenses during bacterial infection by promoting innate immune responses [28]. And while muscle may support resistance defenses, the importance of muscle mass maintenance

for host health provides an opportunity to spur cooperative relationships with microbes. A recent study of infection-induced muscle wasting found that mice that harbor the gut symbiont, *Escherichia coli* serotype O21:H+, were protected from muscle wasting and mortality during infection despite carrying comparable pathogen loads. It was demonstrated that infection with *Salmonella* Typhimurium or *Burkholderia thailandensis* caused translocation of *E. coli* O21:H+ to white adipose tissue (WAT) and induced expression of insulin-like growth factor (IGF-1); thereby suppressing the muscle wasting and improving survival outcomes [26]. This study demonstrates yet again, that vulnerabilities in host physiology are a selective force for the evolution of cooperative microbial traits.

Though adipose tissue was long considered to be an inert energy depot, it is now recognized as a central immune and endocrine organ that has profound influence over systemic metabolism and homeostasis [21,29–31]. As the largest energy reserve in the body, white adipose tissue (WAT) undergoes wasting and mobilization of lipids in response to inflammation, infection, stress and nutrient deprivation [32,33]. Brown adipose tissue (BAT) supports thermogenesis and WAT undergoes beiging to support thermogenesis during cold challenge or during infection [19]. Both heart and BAT rely on lipids as an energy substrate and lack of lipids causes cardiomyopathy and thermogenic failure [34]. Elegant work performed in *Drosophila* demonstrated that muscle coordinates lipid mobilization from the fat body in order to fuel an energetically costly resistance defense against *Pseudomonas entomophila* [35] . Specifically, enhanced mitochondrial function in thoracic muscle increased production of glutamate. Muscle-derived glutamate facilitated lipid mobilization from the fat body and increased defecation and clearance of *P. entomophila* . This muscle-adipose signaling axis is central to driving phenotypic variation of an immunometabolic mechanism of host resistance

in *Drosophila* [35].This work highlights the intricate mechanisms that exist to coordinate inter-organismal metabolism in host defense. Maintenance of triglyceride homeostasis is also crucial as both hypo- and hyperlipidemia are harmful [34]. Luan and colleagues showed that in a murine model of polymicrobial sepsis, interorgan crosstalk coordinates a physiological mechanism of tolerance. They found that growth and differentiation factor 15 (GDF-15), an anorectic hormone produced in response to inflammation, protects mice from cardiomyopathy during polymicrobial sepsis by maintaining liver export of triglyceride via sympathetic circuits with hypothalamus [34].

While it is evident that macronutrient metabolism and homeostasis is crucial to health and host defense responses, macronutrient metabolism and organismal energy balance are largely influenced by micronutrients. Micronutrients are essential elements and molecules that are necessary for growth and development, facilitate signaling and hormone production, and serve as cofactors for proteins and enzymes. Micronutrient deficiencies and overload are consequential, causing growth stunting or increasing susceptibility to disease, infections or toxicity [36]. Thus, the role of micronutrients in physiological host defense are substantial and somewhat underappreciated.

Iron is one essential micronutrient with a considerable historical background that lies at the intersection of metabolism, physiology, host defense, and host-microbe interactions. Thus, the systems that regulate iron homeostasis and metabolism have been shaped through selective pressures from multiple fronts. These multidimensional selective pressures become evident in examining how iron functions in host defense mechanisms—often in

conflicting and highly contextual roles. This dissertation expands on the physiological role of iron in modulating disease pathology through novel mechanisms.

1.2 Role of the micronutrient iron in metabolic homeostasis and physiology

Role of iron in basal metabolism and energy balance

It's estimated that 2% of all human genes encode iron-proteins and that iron is a cofactor for approximately 6.5% of all enzymes in humans [37]. These iron-proteins and enzymes transport and store oxygen, and mediate essential redox biochemistry. Instances of iron depletion or excess are associated with organismal metabolic dysfunction [36,38] . In the case of anemia where iron is depleted, individuals experience decreased appetite and adaptability to endurance training, and increased fatiguability [39–41]. Iron levels are thought to influence appetite through modulation of the hormone leptin, the adipose-derived satiety hormone [42]. Mice lacking ferritin, a model for defective intracellular iron storage, are unable to withstand cold challenge and have reduced thermogenic capacity and beiging of white adipose tissue [43]. On the other hand, iron overload can lead to accumulation of iron in vital organs, like liver and pancreas [44]. Oxidative damage from iron overload in parenchymal tissues is associated with cardiomyopathy, liver damage, and metabolic diseases [45]. Likewise, both iron overload and deficiency disrupt immune function and alter innate inflammatory responses [46–49]. In the case of iron overload, where macrophages exhibit iron deficiency, this can increase the innate inflammatory responses to lipopolysaccharide (LPS) whereas macrophage iron overload has the opposite effect of dampening TLR4-dependent signaling [47–49]. Macrophage polarization is also bidirectionally influenced by iron status, which is hypothesized to contribute to metabolic dysfunction on the tissue and organismal level [50]. Iron supplementation, phlebotomy and iron chelation can alleviate some of the harmful effects associated with dysregulated iron homeostasis, suggesting that there is a bidirectional influence of iron status and metabolic homeostasis [50,51]. Thus, disruptions to iron homeostasis both on the tissue level and organismal level affect metabolic functions and energy balance.

Regulation of iron metabolism and physiology

Iron is one of approximately 30 essential micronutrients and it's regulation is tightly controlled and tuned with organismal metabolism and physiology. In humans, the typical diet contains between 10-15 mg of iron yet only 7-20% is absorbed. Approximately 1-2 mg of iron is lost daily through sloughing of intestinal cells, sweat and urine formation, and desquamation of skin [52]. Reticuloendothelial macrophages in the spleen perform phagocytosis of exhausted reticulocytes, recycling nearly 30 mg of the body's total iron stores per day to support erythropoiesis [52,53]. Importantly, there is no physiological method of iron excretion and iron levels are thus regulated at the level of absorption through the intestine. Laboratory mice used in studies of iron metabolism exhibit considerable differences in iron dynamics due to their small body mass and increased relative food consumption. It's estimated that mice turnover half of their body's iron stores daily and because meat is not a staple of mouse diets, exhibit poor heme absorption [54]. Moreover, common inbred strains exhibit substantial variability in iron homeostasis and responsivity to fluctuations in iron status [55–57].

A considerable amount of dietary iron in humans is in the form of heme and it's uptake was thought to be mediated by heme carrier protein 1 (HCP-1) until it was more convincingly implicated in folate transport [58,59]. Thus, it is proposed than heme uptake is mediated through receptor-mediated endocytosis [54]. Elemental iron on the other hand, is consumed in divalent form: the reduced ferrous state (Fe^{2+}), and the oxidized ferric (Fe^{3+}) state. Ferric iron (Fe^{3+}) is reduced to ferrous iron (Fe^{2+}) by duodenal cytochrome b (Dcytb) and solubilized under acidic conditions in the stomach and duodenum [44,52,60]. Divalent metal ion transporter (DMT1) mediates transport of ferrous iron across apical membranes of

enterocytes [44,52,60]. Intracellular iron is stored as redox-inactive ferric iron (Fe^{3+}) bound to ferritin—which has intrinsic ferroxidase activity [43]. Ferrous iron (Fe^{2+}) is exported into circulation through ferroportin, the only mammalian iron exporter, on the basolateral membrane on enterocytes [44,52,60]. The circulating ferroxidase, ceruloplasmin, oxidizes ferrous iron (Fe^{2+}) to ferric iron (Fe^{3+}), permitting conjugation with apo-transferrin where iron can then be delivered to peripheral tissues via the transferrin receptor 1 (Tfr1). Under homeostatic conditions, approximately 30% of transferrin is saturated with iron (holo-transferrin) and accounts for a small (0.01%) but dynamic fraction of total body iron stores [44]. Tfr1 is present in almost all tissues to mediate import of iron from holo-transferrin. Liver however, also expresses Tfr2, which binds holo-transferrin to sense and regulate iron status through association with other adaptor proteins (discussed further below) [60]. In addition to supplying iron systemically, transferrin prevents damage and iron toxicity by keeping iron in an inert state [60].

Iron must circulate in the bloodstream to maintain homeostasis and this is negatively regulated by hepcidin under instances of iron overload. As iron status is almost entirely dependent on iron uptake through the gut, the response to maintain homeostasis is aimed at intestinal turnover. Hepcidin causes reduced intestinal iron turnover and orchestrates a global iron sequestration response that leads to hypoferremia. Thus, hepcidin is considered to be the master regulator of iron metabolism and was coined hepcidin for being a prominent liver-derived peptide (hep-), and for having bactericidal properties (-cidin) as an acute-phase response protein (discussed further below) [61]. Hepcidin is produced by hepatocytes in response to iron overload (via Tfr2), IL-6-STAT3 and the bone morphogenic protein 6 (BMP6)-SMAD4 pathway [62]. However, inflammation-induced hypoferremia response requires

a threshold of BMP6-SMAD4 signaling and thus, inflammatory signaling alone is not sufficient to activate hepcidin production [63]. Intriguingly, hepatic viral infections and HIV do not induce hepcidin, suggesting a potential hijacking of this niche [64]. Hepcidin functions by inducing the internalization and lysosomal degradation of ferroportin, which prevents iron from entering circulation from enterocytes [62,65]. Though ferroportin is expressed in numerous tissues, macrophages and enterocytes of the duodenum account for the majority of intracellular iron sequestration [65]. Altogether, iron sequestration has the dual function of protecting the host from iron toxicity during iron overload, and limiting iron availability to extracellular pathogens (discussed further below) [66].

Though iron egress from enterocytes is the primary control mechanism for prevention of iron overload, DMT1, Dcytb, and ferroportin are also regulated by hypoxia-inducible transcription factor 2a (HIF2a), a positive regulator of iron absorption [67–71]. Hypoxia and iron deficiency stabilize HIF2a and promote expression of iron uptake genes [68,69,71]. Importantly, hereditary iron overload disorders are exacerbated in part by HIF2a which maintains intestinal iron uptake pathways [68]. More recently, hepcidin has been shown to destabilize HIF2a in the small intestine, demonstrating that hepcidin regulates intestinal iron absorption through two routes [70].

Interestingly, hepcidin can modulate iron metabolism locally at the tissue level. Dendritic cell-specific production of hepcidin in the intestine initiates a local iron sequestration response in macrophages which modulates microbiome composition and facilitates epithelial repair [72]. This finding suggests that tissue level regulation of iron can promote tolerance defenses.

Etiology and effects of iron overload

Iron overload disorders can arise from dietary or genetic causes and can increase circulating levels of iron when transferrin saturation exceeds 60% [44,51,73]. Non-transferrin bound iron (NTBI) is particularly harmful as it can increase production of reactive oxygen species (ROS), like hydroxyl radicals and hydroxide ions via Fenton chemistry . ROS oxidize lipids, proteins and nucleic acids which contribute to oxidative stress and cellular damage [44,51,73]. Eventually this causes lipid peroxidation, protein fragmentation, DNA damage, and DNA strand breaks [44,51,73]. Lipid peroxidation leads to a non-apoptotic, regulated form of cell death referred to as ferroptosis. This pathway is engaged when lipid repair mechanisms are exhausted and there is an accumulation of lipid-based reactive oxygen species [74].

HFE hemochromatosis, or type 1 hemochromatosis, is the most common human iron overload disorder that interferes with the hepcidin signaling axis. HFE is an atypical MHC class 1 protein that mediates the hepcidin signaling axis in the liver by interacting with TFR2 bound to holo-transferrin [75,76]. The most common mutation associated with HFE hemochromatosis is C282Y, identified in 1996 [77]. HFE interacts with β_2-microimunoglobulin to translocate to the cell surface, and the C282Y mutation prevents its ability to bind β_2-microimunoglobulin, reach hepatocyte cell membranes, and interact with Tfr2. There is a high prevalence of HFE hemochromatosis in individuals of Western and Northern European descent, occurring in approximately 5 individuals per 1000, suggesting that this mutation may have been advantageous in maintaining iron homeostasis in iron-poor diets. Juvenile hemochromatosis, or type 2 hemochromatosis, is far less common and is caused by inactivation of hemojuvelin (HJV) which encodes a regulator of the hepcidin signaling pathway [44]. Both *Hjv-/-* and *Hamp-/-* (hepcidin deficient) mice display iron overload disorder

that is similar to that observed in humans. Type 3 hemochromatosis is linked to loss of Tfr2 and the most rare gene mutations associated with hereditary hemochromatosis involved with hepcidin (*Hamp*) and ferroportin [44]. Hemochromatosis is more severe in men but symptoms are not typically detrimental until about 40 years of age. In women, hemochromatosis does not typically present symptoms until after menopause [44].

Hemochromatosis greatly reduces hepcidin production and is marked by uncontrolled iron absorption (up to 8-10 mg per day in humans), hyperferremia, and paradoxically, iron depletion in macrophages and enterocytes of the duodenum [44]. Complications vary widely and include diabetes, liver cirrhosis, colon cancer, cardiomyopathy, arthritis and hypogonadism. If untreated, iron overload can result in fatal multiorgan damage and failure [44]. Therapeutic phlebotomy and iron chelation therapy can alleviate the mild symptoms of joint paint and fatigue, but there is conflicting evidence in the ability for these therapies to reverse the more severe complications [44,51]. Iron overload also increases susceptibility of infection to *Klebsiella pneumoniae*, *Vibrio vulnificus*, HIV, *Yersinia enterocolitica*, and *Listeria monocytogenes* (discussed further below) [48,78–81].

There is a strong association between dysregulated iron homeostasis and adipose tissue function and inflammation. First, iron deficiency and iron overload are associated with obesity and insulin resistance [82]. And as obesity itself is associated with low-grade adipose tissue inflammation, there has been increased interest in understanding the mechanisms by which iron contributes to adipose tissue inflammation and the subsequent impacts on organismal metabolism [21,83]. In obesity, iron accumulates in adipose tissue rather than macrophages, causing inflammation [50]. In vitro analyses with isolated adipocytes have

demonstrated that treatment with iron, transferrin or serum disrupt glucose transport and increase lipolysis through inducing insulin resistance [84,85].

Heme oxygenase 1 (HO-1) is a recently identified biomarker of adipose tissue inflammation and it's overexpression induces insulin resistance both clinically and experimentally [86,87]. Accordingly, insulin resistance is commonly observed in iron overload disorders presumably through increased inflammation [38,88]. Iron chelation therapy has been shown to dampen adipose tissue inflammation and improve insulin sensitivity in obese mouse models in in obese patients [50]. Ferritin, a clinical marker of iron overload, is correlated with insulin resistance and mobilization of fatty acids from adipose tissue in obese women—features indicative of adipose tissue inflammation [89]. The most widely accepted mechanism relating the causality of iron overload in development in insulin resistance has been demonstrated in several mouse models. In models of dietary iron overload in mice, iron accumulates in visceral WAT, causes inflammation, lipolysis and insulin resistance which contribute to systemic insulin resistance [90,91]. Dietary iron supplementation has been shown to exacerbate obesity and insulin resistance in mice fed a high fat diet, and contributes to dysregulated fat and glucose metabolism [92,93]. High iron diets also influence adipokine production in adipose tissue—leading to adipose tissue wasting and decreased production of adiponectin. As adiponectin promotes insulin sensitivity, this is another potential mechanism contributing to iron-overload induced insulin resistance [94,95]. However, there are conflicting reports that have found that insulin resistance precedes disruptions in iron homeostasis observed in mice fed high fat diet [96]. Thus, the mechanisms underlying iron-mediated disruptions in metabolic homeostasis are still undetermined.

More recently, iron content in adipose tissue was found to regulate intestinal lipid absorption [97]. Low adipose tissue iron content reduced lipid absorption in mice fed a high fat diet, preventing obesity. Though there no known mechanisms of direct crosstalk between adipose tissue and the gut, it was shown using adipose tissue transplants that a circulating factor regulates this interorgan axis—further demonstrating the complex role of iron in adipose tissue that extends to physiological function.

1.3 The role of iron in host defense

Iron is an essential nutrient for nearly all living organisms and plays a critical role in both inter-organismal interactions, and intra-organismal functions in health and disease. In both contexts, the role of iron is traditionally defined by its necessity and bioavailability in the environment—which has led to an antagonistic view of the role of iron in host-pathogen interactions.

Microbial iron metabolism at the host interface

Iron is required for almost all bacteria and iron uptake in pathogenic bacteria has been extensively characterized. The ferric uptake regulator (Fur) transcriptionally regulates iron uptake which is mediated by FeoABC protein transport for ferrous iron (Fe2+) and through siderophores and their respective transport systems for ferric iron (Fe3+). Microbes can also uptake iron in the form of heme from hemoglobin or hemopexin through hemophores or direct transport through heme import systems [36].

Siderophores are essential virulence factors for some pathogenic microbes and are induced in response to environments with low iron availability, like host tissues [98]. Enterobactin (Ent), is siderophore produced by *Enterobacteriaceae*, a family of numerous facultative anaerobic enteric pathogens that chelates iron from transferrin and ferritin [98,99]. While the primary function of Ent is to acquire iron in microbial communities of the gut, it performs a secondary action of chelating neutrophil iron and dampening their responses, which could conceivably harm or benefit the host [100]. Importantly, siderophores, a supposed agent of virulence and antagonism, can also spur the opportunity for mutualism. For

example, microbes that consume siderophores but do not produce them, can dampen virulence and benefit the host [101]. Siderophores can also contribute to host health by promoting physiological development [102]. Ent was shown to increase mitochondrial iron levels in *Caenorhabditis elegans* and promote growth. This study demonstrates that microbial iron acquisition systems can be mutually beneficial by providing microbes with a nutrient-rich niche and facilitating transmission into new hosts [102].

Dietary iron supplementation is a common strategy to treat anemias or support nutrition but it can also exacerbate disease especially in gastrointestinal diseases [41,103]. Iron supplementation is associated with dysbiosis which can occur independent of the route of administration (intravenous and dietary)[104]. Iron supplementation has been shown to promote growth of pathogenic bacteria like those from the family of *Enterobacteriaceae* or alter the microbiome composition such that the host is more susceptible to pathogen colonization [105,106]. In humans, heme supplementation reduces the abundance of Firmicutes, which includes beneficial members from the class Clostridia who produce short chain fatty acids [107]. Heme supplementation also increases the abundance of *Enterobacteriaceae* [107].

Though a majority of reports are in agreement with regard to taking caution when administering iron, there are also reports where iron supplementation can dampen gastrointestinal inflammation [108,109]. A murine model of iron supplementation demonstrated that when iron is supplied early in life, mice are protected from chemically-induced colitis in adulthood [110]. More recently, it was shown that commensals have evolved to sense and regulate host iron homeostasis. *Lactobacillus spp*., a genus with low iron requirements, has

been shown to limit iron absorption in murine models of hemochromatosis through modulation of HIF2a [111].

Evolutionary basis of iron in host-microbe interactions and host defense

Iron is an essential nutrient for both host and pathogens. Thus, pathogens occupying the host are limited to the host iron pool and have evolved mechanisms to access iron in order to promote their fitness [66,78,81,112]. The conflict over iron availability has contributed to an antagonistic historical model of host-pathogen coevolution that has led to the identification of host-encoded acute phase responses that sequester iron that limit a pathogen's access to iron— a process referred to as *nutritional immunity* [66,78,81,112]. In response, pathogens have evolved a plethora of counter strategies to overcome nutritional immunity and acquire iron within their hosts. As discussed above, iron acquisition systems and siderophores are often crucial virulence factors needed to proliferate and overcome colonization resistance [99]. The principle of nutritional immunity has shaped the clinical approach to infectious disease and reinforces the traditional view that iron is a finite resource in an endless tug-of-war between host and pathogens. However, host iron acquisition systems are not infallible, which is likely a reflection of the complex evolutionary pressures that have shaped them.

As discussed above, hepcidin is an acute phase protein that is induced by IL-6 and is responsible for orchestrating the iron withholding response [62]. Inflammation also initiates production of calprotectin, lactoferrin and lipocalin-2 in circulation and the intestinal lumen [36,113,114]. This leads to sequestration of iron in intestinal epithelial cells and macrophages, and limits luminal iron availability to pathogenic microbes. Lipocalin-2 is another host encoded

factor that binds Ent [113]– and *Salmonella* has evolved a counter strategy of encoding salmochelin, which is not recognized by lipocalin-2, to evade host resistance defenses. Lipocalin-2 has also been implicated in promoting the colonization resistance capacity for commensal microbes. Deriu and colleagues found that the probiotic *E. coli* Nissle 1917 strain utilizes multiple iron acquisition systems (including salmochelin) and reduces *Salmonella* Typhimurium colonization in inflamed intestines that are producing lipocalin-2 [115]. Nramp1 is another important host factor involved with resistance to intracellular pathogens and mediates export of iron from the phagosome of macrophages. Nramp1 is necessary to protect from fatal *Salmonella* and *Legionella* infections (who replicate in phagosomes) and also promotes iron homeostasis through facilitating macrophage iron recycling during erythrophagocytosis [116].

Abolishment of the hepcidin signaling axis causes iron overload and increases susceptibility to numerous pathogens, ablating protection through inflammation-induced iron-sequestration systems [61]. Humans with hereditary hemochromatosis and mouse models of hemochromatosis (models for hepcidin deficiency and iron overload) display increased susceptibility and mortality to HIV, *Vibrio vulnificus* and *Escherichia coli* [79–81]. Hereditary hemochromatosis afflicts 1 in 200 individuals of Northern European ancestry and C282Y, the most frequent allele mutation observed in HFE hemochromatosis, is present in one quarter to one third of this population. C282Y appeared in Northern European populations around 4000 BC, presumably in the transition from iron-rich meat diets to more grain-based diets with low iron content from the increased reliance on agriculture [44]. Given the considerable health burden and resistance defects associated with HFE hemochromatosis, it is remarkable that C282Y is so prevalent. Thus, it has been hypothesized that C282Y and ensuing iron

overload confers a fitness advantage against certain pathogens [117]. Indeed, hepcidin-deficiency has been observed to promote resistance against intracellular pathogens, like *Salmonella* Typhimurium and *Mycobacterium tuberculosis* [48,118,119]. Similarly, hepcidin-mediated iron sequestration in macrophages can promote virulence of intracellular pathogen like *Burkholderia*, *Legionella*, and *Chlamydia* [78,120,121]—demonstrating that the efficacy of host nutrient withholding is context dependent. In terms of human infections, Moalem and colleagues proposed the intriguing hypothesis that C282Y hereditary hemochromatosis conferred a survival advantage against *Yersinia pestis* in the 14th century [122]. *Y. pestits*, the causative agent of bubonic and pneumonic plague, relies on replication within macrophage phagosomes in order to become systemic and causes mortality [123]. Macrophages are depleted of iron in hemochromatosis, decreasing the ability of intracellular pathogens to proliferate and spread to lymphoid tissues [78,81,122,124]. In support of this, wildtype *Y. pestis* causes a moderate increase in mortality in wildtype mice compared to *Hjv-/-* mice [124]. In a tragic but illuminating incident, a researcher with hereditary hemochromatosis became fatally ill with bubonic septicemic plague acquired in the laboratory [125]. It was later discovered that the researcher had acquired the attenuated *Y. pestis pgm* strain, which does not synthesize the siderophore, yersiniabactin. Thus, hereditary hemochromatosis in the patient complemented the inability of *Y. pestis pgm* to acquire iron, leading to fatal infection [125]. Thus, iron acquisition is a prominent virulence factor of *Y. pestis* and defective host iron handling was exploited in this case.

Despite the historical view of iron in antagonistic defenses, there is growing body of evidence to suggest the role of iron in the cooperative defense system [11,114,126]. First, hemolysis releases heme into circulation, causing toxicity. Several studies have investigated

the importance of mitigating damage incurred by heme during infection to promote anti-virulence defenses. Heme is detoxified by heme oxygenase 1 (HO-1) which degrades heme into iron, biliverdin and carbon monoxide (CO) [126]. HO-1 is mainly produced in phagocytes and mice lacking HO-1 are highly susceptible to sepsis and peripheral forms of malaria while displaying comparable bacterial burdens as the surviving wildtype counterparts [127,128]. Thus, heme and iron recycling is a major pathway driving anti-virulence defenses but HO-1/CO axis has also been shown to promote mitochondrial biogenesis during sepsis with *Staphylococcus aureus*—perhaps serving a role in maintenance of tissue homeostasis [129].

Several studies have demonstrated the link between iron and glucose homeostasis and the importance of this axis in promoting cooperative defenses [3,11,126]. First, polymicrobial sepsis induces anorexia to promote gluconeogenesis and maintain glucose homeostasis during infection. However, infection concurrently causes increases circulating levels of heme which disrupts gluconeogenesis. Weis and colleagues found that hepatic expression of ferritin, the intracellular iron storage protein, is necessary to restore glucose-6-phosphatase activity that is disrupted by iron-induced oxidation [17]. Ferritin expression had no effect on pathogen burdens, and thus, ferritin promotes anti-virulence defenses by maintaining glucose homeostasis to promote survival during sepsis [17].

Our lab recently found that iron supplementation promotes survival against attaching and effacing enteric infection in C3H mice without influencing bacterial burdens [91]. Dietary iron supplementation caused increased accumulation of iron in visceral white adipose tissue and induced insulin resistance—contributing to organismal insulin resistance and hyperglycemia. This transient state of insulin resistance increased availability of glucose in

the intestinal lumen which dampened virulence expression of *Citrobacter rodentium*—driving phenotypic attenuation and eventual selection of genetically attenuated *C. rodentium*. Thus, the physiological effects of iron in WAT induced an anti-virulence program through organismal metabolism [91].

This dissertation expands on the role of iron in host defense by describing novel mechanisms of iron in host metabolism and subsequent implications of iron-induced metabolic rearrangements in host defense—which serendipitously lead us to describe an unexpected etiology for infection-induced colon pathology.

1.4 References

1. Kaufmann, S. H. E. Immunology's Coming of Age. *Front. Immunol.* 10, 684 (2019).

2. Ayres, J. S. Cooperative Microbial Tolerance Behaviors in Host-Microbiota Mutualism. *Cell* 165, 1323–1331 (2016).

3. Ayres, J. S. The Biology of Physiological Health. *Cell* 181, 250–269 (2020).

4. Dethlefsen, L., McFall-Ngai, M. & Relman, D. A. An ecological and evolutionary perspective on human–microbe mutualism and disease. *Nature* 449, 811–818 (2007).

5. Svensson, E. I. & Råberg, L. Resistance and tolerance in animal enemy–victim coevolution. *Trends Ecol. Evol.* 25, 267–274 (2010).

6. Daugherty, M. D. & Malik, H. S. Rules of Engagement: Molecular Insights from Host-Virus Arms Races. *Annu. Rev. Genet.* 46, 677–700 (2012).

7. Schneider, D. S. & Ayres, J. S. Two ways to survive infection: what resistance and tolerance can teach us about treating infectious diseases. *Nat. Rev. Immunol.* 8, 889–895 (2008).

8. Gaber, T., Strehl, C. & Buttgereit, F. Metabolic regulation of inflammation. *Nat. Rev. Rheumatol.* 13, 267–279 (2017).

9. O'Neill, L. A. J., Kishton, R. J. & Rathmell, J. A guide to immunometabolism for immunologists. *Nat. Rev. Immunol.* 16, 553–565 (2016).

10. Nomura, M., Liu, J., Rovira, I. I., Gonzalez-Hurtado, E., Lee, J., Wolfgang, M. J. & Finkel, T. Fatty acid oxidation in macrophage polarization. *Nat. Immunol.* 17, 216–217 (2016).

11. Troha, K. & Ayres, J. S. Metabolic Adaptations to Infections at the Organismal Level. *Trends Immunol.* 41, 113–125 (2020).

12. Zheng, Z., Ma, H., Zhang, X., Tu, F., Wang, X., Ha, T., Fan, M., Liu, L., Xu, J., Yu, K., Wang, R., Kalbfleisch, J., Kao, R., Williams, D. & Li, C. Enhanced Glycolytic Metabolism Contributes to Cardiac Dysfunction in Polymicrobial Sepsis. *J. Infect. Dis.* 215, 1396–1406 (2017).

13. Agwunobi, A. O., Reid, C., Maycock, P., Little, R. A. & Carlson, G. L. Insulin resistance and substrate utilization in human endotoxemia. *J. Clin. Endocrinol. Metab.* 85, 3770–3778 (2000).

14. Langley, R. J., Tsalik, E. L., van Velkinburgh, J. C., Glickman, S. W., Rice, B. J., Wang, C., Chen, B., Carin, L., Suarez, A., Mohney, R. P., Freeman, D. H., Wang, M., You, J., Wulff, J., Thompson, J. W., Moseley, M. A., Reisinger, S., Edmonds, B. T., Grinnell, B., Nelson, D. R., Dinwiddie, D. L., Miller, N. A., Saunders, C. J., Soden, S. S., Rogers, A. J., Gazourian, L., Fredenburgh, L. E., Massaro, A. F., Baron, R. M., Choi, A. M. K., Corey, G. R., Ginsburg, G. S., Cairns, C. B., Otero, R. M., Fowler, V. G., Rivers, E. P., Woods, C. W. & Kingsmore, S. F. An integrated clinico-metabolomic model improves prediction of death in sepsis. *Sci. Transl. Med.* 5, 195ra95 (2013).

15. Bettencourt, I. A. & Powell, J. D. Targeting Metabolism as a Novel Therapeutic Approach to Autoimmunity, Inflammation, and Transplantation. *J. Immunol. Baltim. Md 1950* 198, 999–1005 (2017).

16. Wang, A., Huen, S. C., Luan, H. H., Yu, S., Zhang, C., Gallezot, J.-D., Booth, C. J. & Medzhitov, R. Opposing Effects of Fasting Metabolism on Tissue Tolerance in Bacterial and Viral Inflammation. *Cell* 166, 1512-1525.e12 (2016).

17. Weis, S., Carlos, A. R., Moita, M. R., Singh, S., Blankenhaus, B., Cardoso, S., Larsen, R., Rebelo, S., Schäuble, S., Barrio, L. D., Mithieux, G., Rajas, F., Lindig, S., Bauer, M. & Soares, M. P. Metabolic Adaptation Establishes Disease Tolerance to Sepsis. *Cell* 169, 1263-1275.e14 (2017).

18. Rao, S., Schieber, A. M. P., O'Connor, C. P., Leblanc, M., Michel, D. & Ayres, J. S. Pathogen-Mediated Inhibition of Anorexia Promotes Host Survival and Transmission. *Cell* 168, 503-516.e12 (2017).

19. Schieber, A. M. P. & Ayres, J. S. Thermoregulation as a disease tolerance defense strategy. *Pathog. Dis.* 74, ftw106 (2016).

20. Barber, R. C., Maass, D. L., White, D. J., Horton, J. W., Wolf, S. E., Minei, J. P. & Zang, Q. S. Deficiency in Heat Shock Factor 1 (HSF-1) Expression Exacerbates Sepsis-induced Inflammation and Cardiac Dysfunction. *SOJ Surg.* 1, (2014).

21. Hotamisligil, G. S. Inflammation, metaflammation and immunometabolic disorders. *Nature* 542, 177–185 (2017).

22. Dobner, J. & Kaser, S. Body mass index and the risk of infection - from underweight to obesity. *Clin. Microbiol. Infect.* 24, 24–28 (2018).

23. Lercher, A., Baazim, H. & Bergthaler, A. Systemic Immunometabolism: Challenges and Opportunities. *Immunity* 53, 496–509 (2020).

24. Beisel, W. R. Metabolic response to infection. *Annu. Rev. Med.* 26, 9–20 (1975).

25. Dionne, M. S., Pham, L. N., Shirasu-Hiza, M. & Schneider, D. S. Akt and FOXO dysregulation contribute to infection-induced wasting in Drosophila. *Curr. Biol. CB* 16, 1977–1985 (2006).

26. Palaferri Schieber, A. M., Lee, Y. M., Chang, M. W., Leblanc, M., Collins, B., Downes, M., Evans, R. M. & Ayres, J. S. Disease tolerance mediated by commensal E. coli via inflammasome and IGF-1 signaling. *Science* 350, 558–563 (2015).

27. Baskin, K. K., Winders, B. R. & Olson, E. N. Muscle as a “Mediator“ of Systemic Metabolism. *Cell Metab.* 21, 237–248 (2015).

28. Chatterjee, A., Roy, D., Patnaik, E. & Nongthomba, U. Muscles provide protection during microbial infection by activating innate immune response pathways in Drosophila and zebrafish. *Dis. Model. Mech.* 9, 697–705 (2016).

29. Chait, A. & den Hartigh, L. J. Adipose Tissue Distribution, Inflammation and Its Metabolic Consequences, Including Diabetes and Cardiovascular Disease. *Front. Cardiovasc. Med.* 0, (2020).

30. Kwon, J., Lee, C., Heo, S., Kim, B. & Hyun, C.-K. DSS-induced colitis is associated with adipose tissue dysfunction and disrupted hepatic lipid metabolism leading to hepatosteatosis and dyslipidemia in mice. *Sci. Rep.* 11, 5283 (2021).

31. Romacho, T., Elsen, M., Röhrborn, D. & Eckel, J. Adipose tissue and its role in organ crosstalk. *Acta Physiol.* 210, 733–753 (2014).

32. Tanowitz, H. B., Scherer, P. E., Mota, M. M. & Figueiredo, L. M. Adipose Tissue: A Safe Haven for Parasites? *Trends Parasitol.* 33, 276–284 (2017).

33. Ayres, J. S. Immunometabolism of infections. *Nat. Rev. Immunol.* 20, 79–80 (2020).

34. Luan, H. H., Wang, A., Hilliard, B. K., Carvalho, F., Rosen, C. E., Ahasic, A. M., Herzog, E. L., Kang, I., Pisani, M. A., Yu, S., Zhang, C., Ring, A. M., Young, L. H. & Medzhitov, R. GDF15 Is an Inflammation-Induced Central Mediator of Tissue Tolerance. *Cell* 178, 1231-1244.e11 (2019).

35. Zhao, X. & Karpac, J. Glutamate metabolism directs energetic trade-offs to shape host-pathogen susceptibility in Drosophila. *Cell Metab.* 33, 2428-2444.e8 (2021).

36. Celis, A. I. & Relman, D. A. Competitors versus Collaborators: Micronutrient Processing by Pathogenic and Commensal Human-Associated Gut Bacteria. *Mol. Cell* 78, 570–576 (2020).

37. Andreini, C., Putignano, V., Rosato, A. & Banci, L. The human iron-proteome. *Met. Integr. Biometal Sci.* 10, 1223–1231 (2018).

38. Simcox, J. A. & McClain, D. A. Iron and Diabetes Risk. *Cell Metab.* 17, 329–341 (2013).

39. Stoltzfus, R. J., Chway, H. M., Montresor, A., Tielsch, J. M., Jape, J. K., Albonico, M. & Savioli, L. Low Dose Daily Iron Supplementation Improves Iron Status and Appetite but Not Anemia, whereas Quarterly Anthelminthic Treatment Improves Growth, Appetite and Anemia in Zanzibari Preschool Children. *J. Nutr.* 134, 348–356 (2004).

40. Brownlie, T., Utermohlen, V., Hinton, P. S. & Haas, J. D. Tissue iron deficiency without anemia impairs adaptation in endurance capacity after aerobic training in previously untrained women. *Am. J. Clin. Nutr.* 79, 437–443 (2004).

41. Lawless, J. W., Latham, M. C., Stephenson, L. S., Kinoti, S. N. & Pertet, A. M. Iron Supplementation Improves Appetite and Growth in Anemic Kenyan Primary School Children. *J. Nutr.* 124, 645–654 (1994).

42. Gao, Y., Li, Z., Gabrielsen, J. S., Simcox, J. A., Lee, S., Jones, D., Cooksey, B., Stoddard, G., Cefalu, W. T. & McClain, D. A. Adipocyte iron regulates leptin and food intake. *J. Clin. Invest.* 125, 3681–3691 (2015).

43. Blankenhaus, B., Braza, F., Martins, R., Bastos-Amador, P., González-García, I., Carlos, A. R., Mahu, I., Faisca, P., Nunes, J. M., Ventura, P., Hoerr, V., Weis, S., Guerra, J., Cardoso, S., Domingos, A., López, M. & Soares, M. P. Ferritin regulates organismal energy balance and thermogenesis. *Mol. Metab.* 24, 64–79 (2019).

44. Pantopoulos, K. Inherited Disorders of Iron Overload. *Front. Nutr.* 5, 103 (2018).

45. Datz, C., Felder, T. K., Niederseer, D. & Aigner, E. Iron homeostasis in the Metabolic Syndrome. *Eur. J. Clin. Invest.* 43, 215–224 (2013).

46. Shenkin, A. Micronutrients in health and disease. *Postgrad. Med. J.* 82, 559–567 (2006).

47. Wang, L., Harrington, L., Trebicka, E., Shi, H. N., Kagan, J. C., Hong, C. C., Lin, H. Y., Babitt, J. L. & Cherayil, B. J. Selective modulation of TLR4-activated inflammatory responses by altered iron homeostasis in mice. *J. Clin. Invest.* 119, 3322–3328 (2009).

48. Wang, L., Johnson, E. E., Shi, H. N., Walker, W. A., Wessling-Resnick, M. & Cherayil, B. J. Attenuated inflammatory responses in hemochromatosis reveal a role for iron in the regulation of macrophage cytokine translation. *J. Immunol. Baltim. Md 1950* 181, 2723–2731 (2008).

49. Pagani, A., Nai, A., Corna, G., Bosurgi, L., Rovere-Querini, P., Camaschella, C. & Silvestri, L. Low hepcidin accounts for the proinflammatory status associated with iron deficiency. *Blood* 118, 736–746 (2011).

50. Ameka, M. K. & Hasty, A. H. Fat and Iron Don't Mix. *Immunometabolism* (2020) doi:10.20900/immunometab20200034.

51. Hentze, M. W., Muckenthaler, M. U., Galy, B. & Camaschella, C. Two to Tango: Regulation of Mammalian Iron Metabolism. *Cell* 142, 24–38 (2010).

52. Conway, D. & Henderson, M. A. Iron metabolism. *Anaesth. Intensive Care Med.* 20, 175–177 (2019).

53. White, C., Yuan, X., Schmidt, P. J., Bresciani, E., Samuel, T. K., Campagna, D., Hall, C., Bishop, K., Calicchio, M. L., Lapierre, A., Ward, D. M., Liu, P., Fleming, M. D. & Hamza, I. HRG1 Is Essential for Heme Transport from the Phagolysosome of Macrophages during Erythrophagocytosis. *Cell Metab.* 17, 261–270 (2013).

54. Coffey, R. & Ganz, T. Iron homeostasis: An anthropocentric perspective. *J. Biol. Chem.* 292, 12727–12734 (2017).

55. Clothier, B., Robinson, S., Akhtar, R. A., Francis, J. E., Peters, T. J., Raja, K. & Smith, A. G. Genetic variation of basal iron status, ferritin and iron regulatory protein in mice: potential for modulation of oxidative stress. *Biochem. Pharmacol.* 59, 115–122 (2000).

56. Fleming, R. E., Holden, C. C., Tomatsu, S., Waheed, A., Brunt, E. M., Britton, R. S., Bacon, B. R., Roopenian, D. C. & Sly, W. S. Mouse strain differences determine

severity of iron accumulation in Hfe knockout model of hereditary hemochromatosis. *Proc. Natl. Acad. Sci.* 98, 2707–2711 (2001).

57. Dupic, F. Duodenal mRNA expression of iron related genes in response to iron loading and iron deficiency in four strains of mice. *Gut* 51, 648–653 (2002).

58. Shayeghi, M., Latunde-Dada, G. O., Oakhill, J. S., Laftah, A. H., Takeuchi, K., Halliday, N., Khan, Y., Warley, A., McCann, F. E., Hider, R. C., Frazer, D. M., Anderson, G. J., Vulpe, C. D., Simpson, R. J. & McKie, A. T. Identification of an Intestinal Heme Transporter. *Cell* 122, 789–801 (2005).

59. Andrews, N. C. When Is a Heme Transporter Not a Heme Transporter? When It's a Folate Transporter. *Cell Metab.* 5, 5–6 (2007).

60. Gkouvatsos, K., Papanikolaou, G. & Pantopoulos, K. Regulation of iron transport and the role of transferrin. *Biochim. Biophys. Acta BBA - Gen. Subj.* 1820, 188–202 (2012).

61. Drakesmith, H. & Prentice, A. M. Hepcidin and the Iron-Infection Axis. *Science* 338, 768–772 (2012).

62. Nemeth, E., Rivera, S., Gabayan, V., Keller, C., Taudorf, S., Pedersen, B. K. & Ganz, T. IL-6 mediates hypoferremia of inflammation by inducing the synthesis of the iron regulatory hormone hepcidin. *J. Clin. Invest.* 113, 1271–1276 (2004).

63. Fillebeen, C., Wilkinson, N., Charlebois, E., Katsarou, A., Wagner, J. & Pantopoulos, K. Hepcidin-mediated hypoferremic response to acute inflammation requires a threshold of Bmp6/Hjv/Smad signaling. *Blood* 132, 1829–1841 (2018).

64. Armitage, A. E., Stacey, A. R., Giannoulatou, E., Marshall, E., Sturges, P., Chatha, K., Smith, N. M. G., Huang, X., Xu, X., Pasricha, S.-R., Li, N., Wu, H., Webster, C., Prentice, A. M., Pellegrino, P., Williams, I., Norris, P. J., Drakesmith, H. & Borrow, P. Distinct patterns of hepcidin and iron regulation during HIV-1, HBV, and HCV infections. *Proc. Natl. Acad. Sci.* 111, 12187–12192 (2014).

65. Drakesmith, H., Nemeth, E. & Ganz, T. Ironing out Ferroportin. *Cell Metab.* 22, 777–787 (2015).

66. Núñez, G., Sakamoto, K. & Soares, M. P. Innate Nutritional Immunity. *J. Immunol.* 201, 11–18 (2018).

67. Mastrogiannaki, M., Matak, P., Keith, B., Simon, M. C., Vaulont, S. & Peyssonnaux, C. HIF-2alpha, but not HIF-1alpha, promotes iron absorption in mice. *J. Clin. Invest.* 119, 1159–1166 (2009).

68. Mastrogiannaki, M., Matak, P., Delga, S., Deschemin, J.-C., Vaulont, S. & Peyssonnaux, C. Deletion of HIF-2α in the enterocytes decreases the severity of tissue iron loading in hepcidin knockout mice. *Blood* 119, 587–590 (2012).

69. Shah, Y. M., Matsubara, T., Ito, S., Yim, S.-H. & Gonzalez, F. J. Intestinal Hypoxia-Inducible Transcription Factors Are Essential for Iron Absorption following Iron Deficiency. *Cell Metab.* 9, 152–164 (2009).

70. Schwartz, A. J., Das, N. K., Ramakrishnan, S. K., Jain, C., Jurkovic, M. T., Wu, J., Nemeth, E., Lakhal-Littleton, S., Colacino, J. A. & Shah, Y. M. Hepatic hepcidin/intestinal HIF-2α axis maintains iron absorption during iron deficiency and overload. *J. Clin. Invest.* 129, 336–348 (2018).

71. Taylor, M., Qu, A., Anderson, E. R., Matsubara, T., Martin, A., Gonzalez, F. J. & Shah, Y. M. Hypoxia-Inducible Factor-2α Mediates the Adaptive Increase of Intestinal Ferroportin During Iron Deficiency in Mice. *Gastroenterology* 140, 2044–2055 (2011).

72. Bessman, N. J., Mathieu, J. R. R., Renassia, C., Zhou, L., Fung, T. C., Fernandez, K. C., Austin, C., Moeller, J. B., Zumerle, S., Louis, S., Vaulont, S., Ajami, N. J., Sokol, H., Putzel, G. G., Arvedson, T., Sockolow, R. E., Lakhal-Littleton, S., Cloonan, S. M., Arora, M., Peyssonnaux, C. & Sonnenberg, G. F. Dendritic cell–derived hepcidin sequesters iron from the microbiota to promote mucosal healing. *Science* 368, 186–189 (2020).

73. Hershko, C. Mechanism of Iron Toxicity. *Food Nutr. Bull.* 28, 10 (2007).

74. Yang, W. S. & Stockwell, B. R. Ferroptosis: Death by Lipid Peroxidation. *Trends Cell Biol.* 26, 165–176 (2016).

75. D'Alessio, F., Hentze, M. W. & Muckenthaler, M. U. The hemochromatosis proteins HFE, TfR2, and HJV form a membrane-associated protein complex for hepcidin regulation. *J. Hepatol.* 57, 1052–1060 (2012).

76. Spasić, M. V., Kiss, J., Herrmann, T., Galy, B., Martinache, S., Stolte, J., Gröne, H.-J., Stremmel, W., Hentze, M. W. & Muckenthaler, M. U. Hfe Acts in Hepatocytes to Prevent Hemochromatosis. *Cell Metab.* 7, 173–178 (2008).

77. Feder, J. N., Gnirke, A., Thomas, W., Tsuchihashi, Z., Ruddy, D. A., Basava, A., Dormishian, F., Domingo, R., Ellis, M. C., Fullan, A., Hinton, L. M., Jones, N. L., Kimmel, B. E., Kronmal, G. S., Lauer, P., Lee, V. K., Loeb, D. B., Mapa, F. A., McClelland, E., Meyer, N. C., Mintier, G. A., Moeller, N., Moore, T., Morikang, E., Prass, C. E., Quintana, L., Starnes, S. M., Schatzman, R. C., Brunke, K. J., Drayna, D. T., Risch, N. J., Bacon, B. R. & Wolff, R. K. A novel MHC class I-like gene is mutated in patients with hereditary haemochromatosis. *Nat. Genet.* 13, 399–408 (1996).

78. Ganz, T. & Nemeth, E. Iron homeostasis in host defence and inflammation. *Nat. Rev. Immunol.* 15, 500–510 (2015).

79. Arezes, J., Jung, G., Gabayan, V., Valore, E., Ruchala, P., Gulig, P. A., Ganz, T., Nemeth, E. & Bulut, Y. Hepcidin-Induced Hypoferremia Is a Critical Host Defense Mechanism against the Siderophilic Bacterium Vibrio vulnificus. *Cell Host Microbe* 17, 47–57 (2015).

80. McDermid, J. M., Jaye, A., Schim van der Loeff, M. F., Todd, J., Bates, C., Austin, S., Jeffries, D., Awasana, A. A., Whittlex, A. A. & Prentice, A. Elevated iron status strongly predicts mortality in West African adults with HIV infection. *J. Acquir. Immune Defic. Syndr. 1999* 46, 498–507 (2007).

81. Lopez, C. A. & Skaar, E. P. The Impact of Dietary Transition Metals on Host-Bacterial Interactions. *Cell Host Microbe* 23, 737–748 (2018).

82. Yook, J.-S., Zhou, M., Jaekwon, L. & Chung, S. Iron Deficiency Anemia (IDA) Promotes Visceral Obesity Due to Defective Adipose Tissue Browning (OR09-07-19). *Curr. Dev. Nutr.* 3, (2019).

83. Makki, K., Froguel, P. & Wolowczuk, I. Adipose Tissue in Obesity-Related Inflammation and Insulin Resistance: Cells, Cytokines, and Chemokines. *ISRN Inflamm.* 2013, 1–12 (2013).

84. Rumberger, J. M., Peters, T., Burrington, C. & Green, A. Transferrin and Iron Contribute to the Lipolytic Effect of Serum in Isolated Adipocytes. *Diabetes* 53, 2535–2541 (2004).

85. Green, A., Basile, R. & Rumberger, J. M. Transferrin and iron induce insulin resistance of glucose transport in adipocytes. *Metabolism* 55, 1042–1045 (2006).

86. Moreno-Navarrete, J. M., Ortega, F., Rodríguez, A., Latorre, J., Becerril, S., Sabater-Masdeu, M., Ricart, W., Frühbeck, G. & Fernández-Real, J. M. HMOX1 as a marker

of iron excess-induced adipose tissue dysfunction, affecting glucose uptake and respiratory capacity in human adipocytes. *Diabetologia* 60, 915–926 (2017).

87. Jais, A., Einwallner, E., Sharif, O., Gossens, K., Lu, T. T.-H., Soyal, S. M., Medgyesi, D., Neureiter, D., Paier-Pourani, J., Dalgaard, K., Duvigneau, J. C., Lindroos-Christensen, J., Zapf, T.-C., Amann, S., Saluzzo, S., Jantscher, F., Stiedl, P., Todoric, J., Martins, R., Oberkofler, H., Müller, S., Hauser-Kronberger, C., Kenner, L., Casanova, E., Sutterlüty-Fall, H., Bilban, M., Miller, K., Kozlov, A. V., Krempler, F., Knapp, S., Lumeng, C. N., Patsch, W., Wagner, O., Pospisilik, J. A. & Esterbauer, H. Heme Oxygenase-1 Drives Metaflammation and Insulin Resistance in Mouse and Man. *Cell* 158, 25–40 (2014).

88. Huang, J., Jones, D., Luo, B., Sanderson, M., Soto, J., Abel, E. D., Cooksey, R. C. & McClain, D. A. Iron Overload and Diabetes Risk: A Shift From Glucose to Fatty Acid Oxidation and Increased Hepatic Glucose Production in a Mouse Model of Hereditary Hemochromatosis. *Diabetes* 60, 80–87 (2011).

89. Ryan, B. J., Pelt, D. W. V., Guth, L. M., Ludzki, A. C., Gioscia-Ryan, R. A., Ahn, C., Foug, K. L. & Horowitz, J. F. Plasma ferritin concentration is positively associated with in vivo fatty acid mobilization and insulin resistance in obese women. *Exp. Physiol.* 103, 1443–1447 (2018).

90. Dongiovanni, P., Ruscica, M., Rametta, R., Recalcati, S., Steffani, L., Gatti, S., Girelli, D., Cairo, G., Magni, P., Fargion, S. & Valenti, L. Dietary Iron Overload Induces Visceral Adipose Tissue Insulin Resistance. *Am. J. Pathol.* 182, 2254–2263 (2013).

91. Sanchez, K. K., Chen, G. Y., Schieber, A. M. P., Redford, S. E., Shokhirev, M. N., Leblanc, M., Lee, Y. M. & Ayres, J. S. Cooperative Metabolic Adaptations in the Host Can Favor Asymptomatic Infection and Select for Attenuated Virulence in an Enteric Pathogen. *Cell* 175, 146-158.e15 (2018).

92. Choi, J. S., Koh, I.-U., Lee, H. J., Kim, W. H. & Song, J. Effects of excess dietary iron and fat on glucose and lipid metabolism. *J. Nutr. Biochem.* 24, 1634–1644 (2013).

93. Volani, C., Paglia, G., Smarason, S. V., Pramstaller, P. P., Demetz, E., Pfeifhofer-Obermair, C. & Weiss, G. Metabolic Signature of Dietary Iron Overload in a Mouse Model. *Cells* 7, 264 (2018).

94. Gabrielsen, J. S., Gao, Y., Simcox, J. A., Huang, J., Thorup, D., Jones, D., Cooksey, R. C., Gabrielsen, D., Adams, T. D., Hunt, S. C., Hopkins, P. N., Cefalu, W. T. & McClain, D. A. Adipocyte iron regulates adiponectin and insulin sensitivity. *J. Clin. Invest.* 122, 3529–3540 (2012).

95. Wlazlo, N., van Greevenbroek, M. M. J., Ferreira, I., Jansen, E. H. J. M., Feskens, E. J. M., van der Kallen, C. J. H., Schalkwijk, C. G., Bravenboer, B. & Stehouwer, C. D. A. Iron Metabolism Is Associated With Adipocyte Insulin Resistance and Plasma Adiponectin. *Diabetes Care* 36, 309–315 (2013).

96. Varghese, J., James, J. V., Anand, R., Narayanasamy, M., Rebekah, G., Ramakrishna, B., Nellickal, A. J. & Jacob, M. Development of insulin resistance preceded major changes in iron homeostasis in mice fed a high-fat diet. *J. Nutr. Biochem.* 84, 108441 (2020).

97. Zhang, Z., Funcke, J.-B., Zi, Z., Zhao, S., Straub, L. G., Zhu, Y., Zhu, Q., Crewe, C., An, Y. A., Chen, S., Li, N., Wang, M., Ghaben, A. L., Lee, C., Gautron, L., Engelking, L. J., Raj, P., Deng, Y., Gordillo, R., Kusminski, C. M. & Scherer, P. E. Adipocyte iron levels impinge on a fat-gut crosstalk to regulate intestinal lipid absorption and mediate protection from obesity. *Cell Metab.* 33, 1624-1639.e9 (2021).

98. Singh, V., Yeoh, B. S., Xiao, X., Kumar, M., Bachman, M., Borregaard, N., Joe, B. & Vijay-Kumar, M. Interplay between enterobactin, myeloperoxidase and lipocalin 2 regulates E. coli survival in the inflamed gut. *Nat. Commun.* 6, 7113 (2015).

99. Crosa, J. H. Signal transduction and transcriptional and posttranscriptional control of iron-regulated genes in bacteria. *Microbiol. Mol. Biol. Rev. MMBR* 61, 319–336 (1997).

100. Saha, P., Yeoh, B. S., Olvera, R. A., Xiao, X., Singh, V., Awasthi, D., Subramanian, B. C., Chen, Q., Dikshit, M., Wang, Y., Parent, C. A. & Vijay-Kumar, M. Bacterial Siderophores Hijack Neutrophil Functions. *J. Immunol.* 198, 4293–4303 (2017).

101. West, S. A. & Buckling, A. Cooperation, virulence and siderophore production in bacterial parasites. *Proc. Biol. Sci.* 270, 37–44 (2003).

102. Qi, B. & Han, M. Microbial Siderophore Enterobactin Promotes Mitochondrial Iron Uptake and Development of the Host via Interaction with ATP Synthase. *Cell* 175, 571-582.e11 (2018).

103. Lee, T., Clavel, T., Smirnov, K., Schmidt, A., Lagkouvardos, I., Walker, A., Lucio, M., Michalke, B., Schmitt-Kopplin, P., Fedorak, R. & Haller, D. Oral versus intravenous iron replacement therapy distinctly alters the gut microbiota and metabolome in patients with IBD. *Gut* 66, 863–871 (2017).

104. La Carpia, F., Wojczyk, B. S., Annavajhala, M. K., Rebbaa, A., Culp-Hill, R., D'Alessandro, A., Freedberg, D. E., Uhlemann, A.-C. & Hod, E. A. Transfusional iron

overload and intravenous iron infusions modify the mouse gut microbiota similarly to dietary iron. *Npj Biofilms Microbiomes* 5, 1–11 (2019).

105. Mahalhal, A., Williams, J. M., Johnson, S., Ellaby, N., Duckworth, C. A., Burkitt, M. D., Liu, X., Hold, G. L., Campbell, B. J., Pritchard, D. M. & Probert, C. S. Oral iron exacerbates colitis and influences the intestinal microbiome. *PLoS ONE* 13, e0202460 (2018).

106. Jaeggi, T., Kortman, G. A. M., Moretti, D., Chassard, C., Holding, P., Dostal, A., Boekhorst, J., Timmerman, H. M., Swinkels, D. W., Tjalsma, H., Njenga, J., Mwangi, A., Kvalsvig, J., Lacroix, C. & Zimmermann, M. B. Iron fortification adversely affects the gut microbiome, increases pathogen abundance and induces intestinal inflammation in Kenyan infants. *Gut* 64, 731–742 (2015).

107. Constante, M., Fragoso, G., Lupien-Meilleur, J., Calvé, A. & Santos, M. M. Iron Supplements Modulate Colon Microbiota Composition and Potentiate the Protective Effects of Probiotics in Dextran Sodium Sulfate-induced Colitis. *Inflamm. Bowel Dis.* 23, 753–766 (2017).

108. Dostal, A., Lacroix, C., Pham, V. T., Zimmermann, M. B., Del'homme, C., Bernalier-Donadille, A. & Chassard, C. Iron supplementation promotes gut microbiota metabolic activity but not colitis markers in human gut microbiota-associated rats. *Br. J. Nutr.* 111, 2135–2145 (2014).

109. Kortman, G. A. M., Mulder, M. L. M., Richters, T. J. W., Shanmugam, N. K. N., Trebicka, E., Boekhorst, J., Timmerman, H. M., Roelofs, R., Wiegerinck, E. T., Laarakkers, C. M., Swinkels, D. W., Bolhuis, A., Cherayil, B. J. & Tjalsma, H. Low dietary iron intake restrains the intestinal inflammatory response and pathology of enteric infection by food-borne bacterial pathogens: Immunity to infection. *Eur. J. Immunol.* 45, 2553–2567 (2015).

110. Ettreiki, C., Gadonna-Widehem, P., Mangin, I., Coëffier, M., Delayre-Orthez, C. & Anton, P. M. Juvenile ferric iron prevents microbiota dysbiosis and colitis in adult rodents. *World J. Gastroenterol. WJG* 18, 2619–2629 (2012).

111. Das, N. K., Schwartz, A. J., Barthel, G., Inohara, N., Liu, Q., Sankar, A., Hill, D. R., Ma, X., Lamberg, O., Schnizlein, M. K., Arqués, J. L., Spence, J. R., Nunez, G., Patterson, A. D., Sun, D., Young, V. B. & Shah, Y. M. Microbial Metabolite Signaling Is Required for Systemic Iron Homeostasis. *Cell Metab.* 31, 115-130.e6 (2020).

112. Cassat, J. E. & Skaar, E. P. Iron in Infection and Immunity. *Cell Host Microbe* 13, 509–519 (2013).

113. Flo, T. H., Smith, K. D., Sato, S., Rodriguez, D. J., Holmes, M. A., Strong, R. K., Akira, S. & Aderem, A. Lipocalin 2 mediates an innate immune response to bacterial infection by sequestrating iron. *Nature* 432, 917–921 (2004).

114. Gerner, R. R., Nuccio, S.-P. & Raffatellu, M. Iron at the host-microbe interface. *Mol. Aspects Med.* 75, 100895 (2020).

115. Deriu, E., Liu, J. Z., Pezeshki, M., Edwards, R. A., Ochoa, R. J., Contreras, H., Libby, S. J., Fang, F. C. & Raffatellu, M. Probiotic Bacteria Reduce Salmonella Typhimurium Intestinal Colonization by Competing for Iron. *Cell Host Microbe* 14, 26–37 (2013).

116. Soe-Lin, S., Apte, S. S., Andriopoulos, B., Andrews, M. C., Schranzhofer, M., Kahawita, T., Garcia-Santos, D. & Ponka, P. Nramp1 promotes efficient macrophage recycling of iron following erythrophagocytosis in vivo. *Proc. Natl. Acad. Sci.* 106, 5960–5965 (2009).

117. Weinberg, E. D. Survival Advantage of the Hemochromatosis C282Y Mutation. *Perspect. Biol. Med.* 51, 98–102 (2007).

118. Olakanmi, O., Schlesinger, L. S. & Britigan, B. E. Hereditary hemochromatosis results in decreased iron acquisition and growth by Mycobacterium tuberculosis within human macrophages. *J. Leukoc. Biol.* 81, 195–204 (2007).

119. Nairz, M., Theurl, I., Schroll, A., Theurl, M., Fritsche, G., Lindner, E., Seifert, M., Crouch, M.-L. V., Hantke, K., Akira, S., Fang, F. C. & Weiss, G. Absence of functional Hfe protects mice from invasive Salmonella enterica serovar Typhimurium infection via induction of lipocalin-2. *Blood* 114, 3642–3651 (2009).

120. Paradkar, P. N., De Domenico, I., Durchfort, N., Zohn, I., Kaplan, J. & Ward, D. M. Iron depletion limits intracellular bacterial growth in macrophages. *Blood* 112, 866–874 (2008).

121. Schmidt, I. H. E., Gildhorn, C., Böning, M. A. L., Kulow, V. A., Steinmetz, I. & Bast, A. Burkholderia pseudomallei modulates host iron homeostasis to facilitate iron availability and intracellular survival. *PLoS Negl. Trop. Dis.* 12, e0006096 (2018).

122. Moalem, S., Percy, M. E., Kruck, T. P. A. & Gelbart, R. R. Epidemic pathogenic selection: an explanation for hereditary hemochromatosis? *Med. Hypotheses* 59, 325–329 (2002).

123. St. John, A. L., Ang, W. X. G., Huang, M.-N., Kunder, C. A., Chan, E. W., Gunn, M. D. & Abraham, S. N. S1P-Dependent Trafficking of Intracellular Yersinia pestis through

Lymph Nodes Establishes Buboes and Systemic Infection. *Immunity* 41, 440–450 (2014).

124. Quenee, L. E., Hermanas, T. M., Ciletti, N., Louvel, H., Miller, N. C., Elli, D., Blaylock, B., Mitchell, A., Schroeder, J., Krausz, T., Kanabrocki, J. & Schneewind, O. Hereditary Hemochromatosis Restores the Virulence of Plague Vaccine Strains. *J. Infect. Dis.* 206, 1050–1058 (2012).

125. Frank, K. M., Schneewind, O. & Shieh, W.-J. Investigation of a Researcher's Death Due to Septicemic Plague. *http://dx.doi.org/10.1056/NEJMc1010939* (2011) doi:10.1056/NEJMc1010939.

126. Chen, G. Y. & Ayres, J. S. Beyond tug-of-war: Iron metabolism in cooperative host–microbe interactions. *PLOS Pathog.* 16, e1008698 (2020).

127. Larsen, R., Gozzelino, R., Jeney, V., Tokaji, L., Bozza, F. A., Japiassú, A. M., Bonaparte, D., Cavalcante, M. M., Chora, Â., Ferreira, A., Marguti, I., Cardoso, S., Sepúlveda, N., Smith, A. & Soares, M. P. A Central Role for Free Heme in the Pathogenesis of Severe Sepsis. *Sci. Transl. Med.* 2, (2010).

128. Seixas, E., Gozzelino, R., Chora, Â., Ferreira, A., Silva, G., Larsen, R., Rebelo, S., Penido, C., Smith, N. R., Coutinho, A. & Soares, M. P. Heme oxygenase-1 affords protection against noncerebral forms of severe malaria. *Proc. Natl. Acad. Sci.* 106, 15837–15842 (2009).

129. MacGarvey, N. C., Suliman, H. B., Bartz, R. R., Fu, P., Withers, C. M., Welty-Wolf, K. E. & Piantadosi, C. A. Activation of Mitochondrial Biogenesis by Heme Oxygenase-1–mediated NF-E2–related Factor-2 Induction Rescues Mice from Lethal Staphylococcus aureus Sepsis. *Am. J. Respir. Crit. Care Med.* 185, 851–861 (2012).

Chapter 2: Adipose triglyceride lipase (ATGL) mediates lipolysis and lipid mobilization in response to iron-mediated negative energy balance

2.1 Introduction

Mammals have evolved complex homeostatic control mechanisms to maintain their energy balance within a defined set point. These include mechanisms that regulate nutrient acquisition, nutrient utilization and energy storage, to achieve a balance between energy intake and energy expenditure. Energy expenditure is a function of multiple factors including basal metabolism, adaptive thermogenesis and physical activity [1,2]. Basal metabolism of an organism involves processes within the organism that are necessary to sustain life. Adaptive thermogenesis describes energy that is dissipated in the form of heat when animals consume a meal or adapts to a cold environment. Physical activity involves voluntary movements by the organism. Homeostatic control of energy balance is maintained through the interactions between genetic and environmental factors. Disruptions in these interactions that ultimately lead to energy imbalances will manifest as changes in energy storage [2]. Animals that have an energy intake that exceeds energy expenditure will have a net gain, resulting in increased energy storage. If animals have an energy intake that is less than energy expenditure, there will be a net loss, resulting in a loss of fat and other energy stores. The ability to maintain energy balance within the homeostatic set point is critical as disruptions to the balance and resulting changes in energy storage may render the organism more susceptible to diseases. For example, the increased adiposity in obesity predisposes individuals to cardiovascular disease and type 2 diabetes [3,4]. Extreme causes of net energy loss can result in dangerously low body fat content that predisposes animals to infections, cardiovascular damage and musculoskeletal issues [5–7]. Thus understanding the genetic and environmental factors that regulate energy balance is necessary for our understanding of the metabolic basis of disease.

The essential micronutrient iron has emerged as a critical regulator of body weight and energy balance. In children and adults, there is a greater prevalence of iron deficiency in both overweight and obese individuals [8]. The causality of iron in the regulation of adipose tissue stores has been demonstrated in animal studies. Iron deficient diet causes increased adiposity in rats and excess dietary iron causes a reduction in body fat mass in rodents [9]. The possible underlying mechanisms for iron mediated control of energy balance and the resulting changes to fat storage are likely complex and multifactorial. For example, iron status affects energy intake by regulating food consumption. Iron deficiency is associated with appetite loss that can be reversed with iron supplementation possibly through its effects on the satiety hormone leptin [10–12]. Iron has dramatic effects on multiple aspects of the gastrointestinal tract that will influence nutrient absorption and affect the overall energy balance of the individual. For example, changes in luminal iron concentration will lead to changes in the composition of the intestinal microbiome, that can lead to functional changes that control nutrient harvesting and uptake [13]. Iron can also change the inflammatory state of digestive organs that will affect the ability of an individual to absorb nutrients [14]. Iron has also been shown to regulate systemic responses that control the ability of the small intestine to regulate nutrient absorption [15]. The critical role of iron for providing adequate levels of oxygen will control an individual's capacity to endure the amount and rigor of physical activity. Individuals that are anemic experience fatigue, reducing the amount of physical activity they undertake. Furthermore, individuals who experience low iron without anemia have impaired adaptation to aerobic activity [16]. Lastly, as iron regulates various aspects of energy metabolism including cellular respiration, the ability of an organism to carry out their basic basal metabolic functions will also be dependent on the iron status of the individual.

The changes in energy balance and storage controlled by the iron status of an individual will result in physiological responses involved in energy substrate mobilization, storage and breakdown. White adipose tissue (WAT) serves as the major storage depot for lipids, where excess lipid species are stored as triacylglycerol in lipid droplets. Under conditions of increased energetic demand or in response to stress stimuli, triacylglycerol is mobilized from WAT to meet organismal energy demands that are not met by diet [17]. Triacylglycerides (TG) in lipid droplets are hydrolyzed into diacylglycerol (DG) by adipose triglyceride lipase (ATGL) and monoacylglycerol (MG)/ free fatty acids and glycerol by hormone-sensitive lipase (HSL). FFA and glycerol are then released into circulation where they can be utilized by peripheral tissues. ATGL and HSL are considered essential lipolytic enzymes and are negatively regulated by insulin and IGF-1 signaling through the PKA/PKC signaling cascade [18,19]. In vitro, it was shown that iron and transferrin from serum can induce lipolysis in an acute time frame and is independent of PKA and PKC signaling [20]. More recently, it was shown that the elevated levels of fatty acid mobilization, adipose tissue HSL and ATGL in obese women correlated with elevated levels of ferritin, suggesting that *in vivo*, elevated iron stores correlates with increased fatty acid mobilization [21]. While iron has an established correlative relationship with adipose tissue physiology, a causative role for iron in regulating lipid mobilization *in vivo* and how this relates to iron mediated changes in energy balance, as well as the underlying mechanisms for these processes remain unknown.

In the present study, we examined the role of the essential micronutrient iron in regulating energy balance. Using a dietary model of iron overload, we found that an acute course of excess dietary iron leads to a negative energy balance and profound whole body wasting in mice. The negative energy balance was due to iron dependent intestinal nutrient

malabsorption. To meet energetic demands, we found that iron caused increased lipid utilization associated with increased lipolysis, lipid mobilization, and fat wasting. Using a transgenic mouse model, we found that lipolysis was dependent on ATGL activity specifically in adipose tissue. Animals lacking ATGL in adipose tissue, shifted to carbohydrate utilization when fed dietary iron and exhibited a severe cachectic response due to the intestinal nutrient malabsorption. Our work highlights the multi-faceted role of iron regulation of organismal metabolism and provides a novel *in vivo* mechanism for micronutrient control of lipolysis that is necessary for regulating mammalian energy balance.

2.2 Material and Methods

Mice. Six week-old male C57BL/6 mice were purchased from Jackson Laboratories and housed in our facility to acclimate for 2 days prior to experimentation. To study ATGL-dependent lipolysis, we performed crosses with B6N.129S-Pnpla2tm1Eek/J mice to B6.Cg-Tg(Fabp4-cre)1Rev/J both from Jackson labs to generate Pnpla2;Fabp4 cre+ and Pnpla2;Fabp4 cre- mice. For experiments, 6-8 week old male littermates were used. All animal experiments were done in accordance with The Salk Institute Animal Care and Use Committee and performed in our AALAC-certified vivarium.

Mouse diets and Pairwise feeding. Mice were fed a 2% carbonyl iron supplemented diet or a control diet from Envigo. Daily food intake was determined by measuring mass of food pellets daily from single-housed mice. For pair feeding experiments, iron and control diets were supplied ad libitum while the third pair fed group of mice were given control diets that were weight-matched to the historical daily food intake of a mouse given iron diet ad libitum.

Body composition measurements. Total body fat and lean mass were measured using an EchoMRI machine. Total fat or total lean mass(g) was normalized to total body mass(g) to determine the percent body composition of fat and lean tissues. Fat pad masses were measured by dissecting and weighing subcutaneous fat pads (inguinal WAT), visceral fat pads (gonadal WAT), and mesenteric WAT post mortem. Muscles from hindlimb were dissected and weighed postmortem. The following muscles were harvested to represent muscles of varied myofiber composition: Quadricep (primarily fast twitch), Tibialis anterior

(fast/slow twitch), extensor digitorum longus (fast/slow twitch), Soleus (slow twitch), gastrocnemius (fast/slow twitch).

Metabolic phenotyping by indirect calorimetry. Mice were singly housed in metabolic cages from the Columbus Instruments Comprehensive Lab Animal Monitoring System (CLAMS) where O2 consumption, CO2 production, and activity data were collected. Food consumption was measured by weighing food pellets daily in order to determine calorie intake. Mice were removed from metabolic cages daily to measure body mass with a scale and body composition using EchoMRI. Energy Expenditure was calculated using the modified Weir equation (modified for systems lacking urine collection): EEJ(Joules/hour) = 15.818 J/ml * VO2 + 5.176 J/ml *VCO2 . Where VO2 and VCO2 are in units of ml/hour. Respiratory Exchange Ratio (RER) was determined by dividing VCO2/VO2.

Insulin Tolerance Tests. Animals were fasted for 6 hours in fresh cages with ad libitum access to water. Blood glucose measurements were taken using a Nova Max plus by making small cuts to the tips of tails using a sterile razor blade and gently squeezing the tail from base to tip. Insulin was administered according to body mass (1U/kg) in a single intraperitoneal injection at time=0 minutes. Blood glucose measurements were taken every 15 minutes for the first hour post insulin injection and then again at 90 and 120 minutes post injection. Blood glucose measurements were normalized to their time=0 fasted blood glucose levels to generate a curve representing the percent drop in glucose levels from basal.

Lipid Tolerance Test. Animals were fasted for 9 hours in fresh cages with *ad libitum* access to water on day 9 of dietary regimens. Mice were injected intraperitoneally with 10μL/g of Intralipid. Blood was collected at 0, 1, 2, 3, 4, and 5 hours post injection in Microvettes by tail bleed. The microvettes were centrifuged at 6000 RPM for 20 minutes and serum was harvested for quantifying non esterified free fatty acids (Wako) and total triglycerides (Fujifilm L-Type Triglyceride M kit) and following the manufacturers protocol.

Oral lipid tolerance test. Animals were fasted for 14-16 hours overnight in fresh cages with *ad libitum* access to water on day 8 of dietary regimens. Mice were orally administered 250 ul of olive oil by gavage. Blood was collected at 0, 1, 2, 3, 4, and 5 hours following administration of oil in Microvettes by tail bleed. The microvettes were centrifuged at 6000 RPM for 20 minutes and serum was harvested for quantifying non esterified free fatty acids (Wako) total triglycerides using the (Fujifilm L-Type Triglyceride M kit) and following the manufacturers protocol.

Bomb calorimetry. Mice were co-housed (5 mice per cage) in Pure-o'Cel bedding and provided *ad libitum* access to water and control iron diet (CID) or 2% carbonyl iron diet (IRD). Body mass and food mass was measured daily to determine daily food intake (calorie intake). All bedding was collected daily and stored in sealed bags at -20˚C until further processing. Fecal pellets were collected from bedding and desiccated in an airtight chamber with drierite for ≥20 hours. Fecal pellets were combined from two cages per day per respective diets. Combined desiccated fecal pellets were weighed and ground using mortar and pestle. ddH_2O was mixed into ground feces 50 ul at a time to reach a mealy-pasty consistency. Parr 6100 Calorimeter instruments and accessories were used to determine

caloric content of fecal matter thereafter. Fecal mixture was used to form a compacted cylindrical pellet and placed in a brass dish inside bomb containing 1 ml ddH_2O and twisted ignition string touching fecal pellet. Bomb was filled with O_2, sealed and carefully inserted into 2000 g of room temperature deionized H_2O. Ignition leads were connected to bomb and calorimetry chamber was closed for testing. Calculations were performed according to the Parr instrument manual to determine calories/gram of fecal matter. Net caloric absorption was determined by subtracting total fecal caloric content from pooled daily caloric intake from respective diets.

Insulin Signaling Experiments and Western blot. To examine insulin signaling in tissues, mice were fasted for 6 hours in fresh cages with *ad libitum* access to water and injected with insulin as described above (insulin tolerance test). Injections were performed in 15-minute staggered intervals. Exactly 15 minutes following insulin injection, mice were sacrificed and liver, muscle and fat pads were harvested, immediately flash frozen in liquid nitrogen, and stored at -80˚C. Tissues were subsequently processed for western blot analyses as described below.

Western blot. Snap frozen tissues were ground into fine powder using ceramic mortar and pestles equilibrated in liquid nitrogen. Powder was homogenized in BeadMill24 with a ceramic bead in Tissue extraction reagent or adipose tissue protein extraction buffer with phosphatase and protease inhibitors added (Adipose tissue protein lysis buffer: 50mM Tris pH 7.5, 150mM NaCl, 1% NP-40, 0.5% Sodium Deoxycholate, 5% Glycerol). Lysates were purified by three consecutive centrifugations at 4˚C to remove debris and fat and quantified using Pierce BCA protein assay kit. Samples were loaded into a 7% Tris-acetate gel

following a 10-minute sonication, and a 10-minute boil at 70˚C. Gels were ran for 150V for 60 minutes in Invitrogen Mini Gel Tank and transferred to nitrocellulose blot using the BioRad Turbo Transblot system for 10 minutes at 25V (1.3 A). Blots were stained with OneBlock Wes protein stain and cut into strips according to size of target protein. Strips were then washed in TBST (20mM Tris, 150mM NaCl, 0.1% Tween20 w/v) and blocked with 5% BSA in TBST for 1 hour at room temperature. Blots were incubated with primary antibodies overnight at 4˚C on an orbital shaker (p-AKT, AKT, ATGL, p-HSL, HSL, p-PKAc, PKAc, GAPDH; see Catalog details in materials table). Blots were washed 3x 10 minutes with TBST and incubated with anti-rabbit for 1 hour at room temperature with Anti-Rabbit IgG HRP-linked antibodies with gentle shaking and subsequently washed 3x 10 minutes with TBST. Blots were developed and imaged using ProSignal Dura chemiluminescence in the BioRad Gel Doc XR system. Densitometry analyses were performed suing the ImageLab Software and phosphorylated proteins were normalized to total protein level and subsequently to housekeeping protein, GAPDH. Phosphorylated target proteins were probed/measured first, and the same membrane was used to measure total levels of that respective protein using the following stripping protocol: Blot was covered with stripping buffer for 5 mins and discarded. Blot was covered with fresh stripping buffer again for 5 minutes and discarded. Blot was washed two times with PBS for 10 minutes by gentle shaking. Blot was washed two times with TBST for 5 minutes by gentle shaking. After final wash, blot was blocked with 5% BSA for 1 hour at room temperature and used for subsequent antibody incubations as described above. (Mild stripping buffer (500ml): 7.5 glycine, 5 ml Tween20, 0.5g sodium dodecyl sulfate, pH 2.2)

Gene expression analyses. Tissues were flash frozen in liquid nitrogen immediately following harvest from sacrificed animals. Tissues were ground into a powder using ceramic mortar and pestles equilibrated in liquid nitrogen. Powder was added to Trizol reagent and

homogenized with a ceramic bead in a bead beater. Chloroform was added to homogenate and centrifuged to separate the organic and aqueous layers. Aqueous layer was carefully transferred to fresh nuclease-free tubes where isopropanol was added and mixture was left to precipitate at -20˚C for at least 1 hour. Isopropanol/aqueous layer solution was added to a Qiagen RNeasy column and RNeasy protocol was followed from this step, including the removal of genomic DNA using Qiagen's on-column DNase kit. RNA was eluted in nuclease-free H_2O and quantified using a Nanodrop Spectrophotometer. cDNA was synthesized using SuperScript IV using ~200 ng RNA and oligo dT for mammalian cDNA. Real time quantitative PCR was performed using SYBR green Mix on QuantStudio 5 from Applied Biosystems. Relative standard curves method was used to analyze gene expression relative to a pooled sample dilution series. *Rps17* was used as an endogenous housekeeping control for relative normalization. Annealing temp of 60˚C was used for all RT-qPCR reactions.

Primer Table

Gene target	**Forward 5'->3'**	**Reverse 5'->3'**
Atrogin-1	CAGCTTCGTGAGCGACCTC	GGCAGTCGAGAAGTCCAGTC
MuRF-1	AGTGTCCATGTCTGGAGG TCGTTT	ACTGGAGCACTCCTGCTTGTAGA T
MyoD	CAGTGGCGACTCAGATGC	CGCCTCACTGTAGTAGGCG
Myogenin	GCAATGCACTGGAGTTCG	GTCCACGATGGACGTAAGG
Rps17	CGCCATTATCCCCAGCAAG	TGTCGGGATCCACCTCAATG
Fpn	CCCTGCTCTGGCTGTAAAAG	TAGGAGACCCATCCATCTCG
Dmt1	CAATGGAATAGGCTGGAGGA	CCCAATGCAATCAAACACTG
Tfr1	TCGCTTATATTGGGCAGACC	ATAAGGGGCTGGCAGAAACT
Transferrin	GCGCATTCAAGTGTCTGAAA	GAGCCACAACAGCATGAGAA
Ftl	GGGCCTCCTACACCTACCTC	CTCCTGGGTTTTACCCCATT
Fth	CTGAATGCAATGGAGTGTGC	TCTTGCGTAAGTTGGTCACG
Hmox1	ACGCATATACCCGCTACCTG	CCAGAGTGTTCATTCGAGCA
Steap2	ATGCCAGAAACCAGCAGAGT	TGCAAAGAAGAAGCTCAGCA
Hepcidin	TTGCGATACCAATGCAGAAG	GGATGTGGCTCTAGGCTATG
Genotyping primers		
cre recombinase	CGCGCTCTGGCAGTAAAAACTATC	CCCACCGTCAGTACGTGAGATATC

***Ex vivo* lipolysis assay.** Mice were fed control or 2 % carbonyl iron diets for a period of 3, 6, and 9 days and fasted for 6 hours in fresh cages with *ad libitum* access to water. Inguinal and gonadal white adipose tissue pads were harvested, cut into 2 ~30-50 mg pieces and placed into separate wells in a 24 well plate with 300 µl of ice-cold PBS. Following the completion of tissue harvest, all fat pads were gently dabbed on a paper towel, cut with scissors in a central latitudinal location to introduce freshly cut exposed tissue, and carefully transferred to 24 well plates containing 300 µl of room-temperature Krebs-Ringer bicarbonate Hepes buffer ph 7.4 (120mM $NaCl_2$, 4mM KH_2PO_4, 1mM $MgSO_4$, 0.75 mM $CaCl_2$, 30 mM Hepes pH 7.4, 10mM $NaHCO_3$; solution was sterilized and stored at 4˚C until day of *ex vivo* lipolysis assay when fatty acid free bovine serum albumin (to 2% wbv) and D-glucose (5mM) was added. Plates were incubated for 4 hours in a 37˚C tissue culture incubator and supernatants were transferred to fresh tubes and frozen at -20˚C until they were used to quantify free fatty acids and glycerol content as described below.

Free fatty acid, glycerol and triglyceride assays. Serum from fasted mice and supernatant from *ex vivo* lipolysis assay were added to a 96 well plate according to the Wako Fuji Film protocol and reagents were added and incubated according to the respective FFA or glycerol Wako protocols. Standards were generated using a dilution series of glycerol or non-esterified fatty acids (WAKO). A 1:2 dilution series from 1mM to 0.03125mM was used to generate the FFA standard curve. The standard curve for glycerol used the following series in mM: 8, 7, 6, 5, 4, 3, 2, 1, 0.5, 0.25. Triglyceride standards were generated from multi-calibrator lipids in the following series (mg/dL): 48, 96, 144, 192, 240, 288, 384, 480. To determine FFA and glycerol content, 5 µl of samples and standards were used. To determine

triglyceride content, 4 µl of samples were used. Following methods outlined in manufacturer's protocols, samples were quantified from standard curve analyses using a 96-well VERSAmax microplate reader and SoftMax Pro software. FFA and glycerol levels from *ex vivo* lipolysis assays were normalized to recorded tissue masses.

Iron assay for determining tissue iron content. Total iron content was determined using colorimetric Iron Assay from Abcam according to manufacturer's protocol. For serum, blood was collected via cardiac puncture in microtainers and centrifuged at 6000 rpm for 20 minutes and serum was stored at -80˚C. Tissues were flash frozen in liquid nitrogen immediately following harvest from sacrificed animals. Tissues were ground into a powder using ceramic mortar and pestles equilibrated in liquid nitrogen. 10-30 mg of tissue powder and 10 ul serum was suspended in Iron assay buffer and gently homogenized by pipetting. Tissue samples were centrifuged at 13000 rpm for 10 minutes to remove insoluble materials and supernatant was used for iron content quantification according to manufacturer's protocol in 96-well plates. A standard curve was generated using the following dilution series (nmol/well): 0.5, 1.0, 1.5, 2.0, 2.5, 4, 6, 8, 10, 20, 40. Samples were quantified using a 96-well VERSAmax microplate reader and SoftMax Pro software. Iron content was normalized to respective tissue masses.

Principal component analyses. To determine the light/dark cycle and diet relationships between samples, EEJ, RER and total activity spreadsheets were transformed to represent hourly blocks of the light/dark cycle during periods of matched food consumption; this was the primary derived data used for PCA (Jolliffe, 2005). Principal component analysis was computed using the *mixOmics* R package (v6.14.1) with 10 components considered in the

calculations (Rohart et al., 2017). Eigenvalues of the variance-covariance matrix were calculated, and the data centered and scaled (standardized) to account for heterogeneity in variances across the variables. Multivariate analysis plots were generated using the R function plotIndiv (Plot of Individuals). The first two principal components were projected onto the sample space with the ellipses representing 95% confidence intervals.

Linear Regression and ANCOVA. For linear regression analyses of energy expenditure based on total or lean mass, the daily energy expenditure for each mouse was determined by summing J/hr per 24 hour periods preceding total and lean mass measurements. Daily energy expenditure (J/day) was plotted as a function of total body mass or lean mass for each mouse over the course of the experimental window for respective dietary groups. GraphPad Prism 9.0e was used to perform regression analyses. Simple linear regression was performed for each dietary group and linear regression lines were compared to determine if the slopes and y intercepts were significantly different between dietary groups. ANCOVA analyses were performed when slopes between dietary group linear regression lines were not significantly different and the pooled slope was used to calculate an adjusted daily energy expenditure at the group mean mass. Group mean mass was determined by calculating the mean total or lean body mass for the groups presented in linear regression plots. ANCOVA adjusted daily energy expenditure was determined by using the following equation: (actual J/day)-[(average group LBM or TBM (g))-(actual TBM or LBM (g))]*pooled slope (J day^{-1} per g change in mass). The NIDDK Mouse Metabolic Phenotyping Centers (MMPC, www.mmpc.org) and Energy Expenditure Analysis page (http://www.mmpc.org/shared/regression.aspx) was used as a reference to guide the EE

ANCOVA analysis done for this work. NIDDK MMPC is supported by grants DK076169 and DK115255.

Clinical pathology analysis. Six week old C57BL/6 male mice were provided *ad libitum* access to water and control iron diet (CID) or 2% iron rich diet (IRD) for 8 days. On day 9 of dietary regimens, animals were fasted for 6 hours in fresh cages with *ad libitum* access to water prior to sacrifice. Blood was collected via cardiac puncture in BD microtainers and centrifuged at 6000 rpm for 20 minutes to collect serum. Serum was stored at -80˚C. Serums were sent to IDEXX Laboratories for quantification of ALP, AST, ALT, lipase and cholesterol levels.

Statistics. All variables were analyzed using GraphPad Prism 9.0e. Categorical variables are expressed as numbers and percentages, and quantitative variables as means ± standard error of the mean (SEM). Where data is shown as dot plots, each dot represents a single mouse or biological replicate. One-way analysis of variance (ANOVA) with a post Tukey's test or Two-way ANOVA were used as appropriate. Student's two tailed t-test was performed to evaluate the differences between two independent groups or paired samples as appropriate. A P value <0.05 was used to reject the null hypothesis. All experiments used an n of 3 or more and represent 1-3 independent experiments. Further information regarding specific P values, n used in each experiment, and how data are presented can be found in the figure legends.

2.3 Results

2.3.1 Dietary iron supplementation causes negative energy balance and nutrient malabsorption

While it is well established that iron regulates organismal metabolism and energy balance, the underlying mechanisms regulating these processes are not completely known. We established a dietary model to determine the mechanistic basis for the effects of an acute course of surplus dietary iron on organismal metabolism and energy balance. Carbonyl iron is a dietary iron supplement that has reduced inflammatory effects on the gastrointestinal tract relative to iron sulfate-based alternatives (Devasthali et al., 1991). We fed 6-week-old C57BL/6 mice an iron rich diet (IRD) containing 2% carbonyl iron or a nutrient matched control iron diet (CID) and found that while CID-fed mice exhibited an expected slight increase in whole body weight over the course of the experiment, IRD-fed mice exhibited a drastic whole-body wasting phenotype, with mice losing approximately 20% of total body weight by day 8 post diet initiation (**Figure 1A** and **Supplemental Figure 1A**). Net negative energy balance caused by the IRD can be due to an increase in energy expenditure and/or a decrease in energy intake. To determine the effects of dietary iron on energy expenditure, we fed 6-week-old C57BL/6 mice CID or IRD for nine days and housed them in the Comprehensive Lab Animal Monitoring System (CLAMS) to measure gas exchange volumes and rates continuously over the experimental course (mice were allowed to acclimate for a day before introduction of the diets). We observed a drastic continuous decrease in energy expenditure of mice following introduction of the IRD (**Figure 1B, Supplemental Figure 1B**). Principal component analysis (PCA) of light/dark cycle EEJ in CID and IRD-fed mice revealed a distinct clustering of samples according to light cycle and diet, suggesting that patterns of energy expenditure are impacted by diet and light cycle (**Figure 1C**). The clustering is supported by non-overlapping 95% confidence intervals (ellipses) (**Figure 1C**).

As energy expenditure is positively correlated with body mass, we performed a regression-based analysis of daily energy expenditure as a function of daily total body mass (TMB) or daily lean body mass (LBM) over the eight day dietary regimen (**Figure 1D and Supplemental Figure 1C**). We found that the relationship between TBM and energy expenditure significantly depended on diet and that energy expenditure increased significantly with TBM on both CID and IRD (**Supplemental Figure 1C**). Energy expenditure increased significantly with increased LBM and the influence of LBM on energy expenditure was equivalent for mice fed CID or IRD (**Figure 1D**). Interestingly, ANCOVA analysis revealed that IRD resulted in decreased energy expenditure as a function of mouse LBM relative to mice fed CID, suggesting that IRD does not cause negative energy balance by increasing energy expenditure (**Figure 1E**). Changes in activity level and thermogenesis can contribute to differences in energy expenditure. We observed no significant difference in total activity levels, but PCA of light/dark cycle activity levels revealed distinct clustering of dark cycle activity, suggesting that activity patterns are impacted by diet during the dark cycle (**Supplemental Figure 1D-E**). Additionally, mice fed IRD exhibited a decrease in core body temperature over the course of the dietary regimen, suggesting that reduced energy expenditure caused by excess dietary iron may in part be due to a decrease in thermogenesis (**Supplemental Figure 1F**).

Notably, mice fed IRD eat significantly less food during the first 48 hours post diet initiation, with no significant difference in food consumption between the dietary groups by day 3 post diet initiation (**Figure 1F**). To determine if this initial food aversion response in IRD-fed mice was responsible for the whole-body wasting, we performed a pairwise feeding analysis. Pair fed mice on CID had a steep decrease in body mass within the first 48 hours of

the diet regimen and increased body mass thereafter; whereas mice fed IRD *ad libitum* exhibited continual weight loss over the 8 day diet regimen (**Figure 1G and Supplemental Figure 1G**). Thus, the initial reduced feeding alone does not account for the continual whole body wasting caused by the acute course of excess dietary iron. Mice fed IRD also exhibited comparable body temperature and activity levels as pair fed mice on CID (**Supplemental Figure 1H, I, J**). We next analyzed energy expenditure of mice of the three dietary regimens in the CLAMS and found that mice fed IRD had a significant decrease in energy expenditure relative to both groups of mice fed CID *ad lib* and pair fed (**Figure 1H, I, Supplemental Figure 1K**). Consistently, PCA revealed distinct clusters of energy expenditure between the three dietary regimens during the light cycles (**Figure 1I**). We performed regression-based analyses of daily energy expenditure as a function of daily TBM and daily LBM for our pairwise feeding conditions to determine if dietary regimens caused a mass-independent effect on energy expenditure (**Figure 1J-K, Supplemental Figure 1L**). Consistent with our previous analyses of CID and IRD, we found that the relationship between TBM and energy expenditure significantly depended on diet (F= 41.21 df= 2, 102, P<0.0001*)* and energy expenditure increased significantly with TBM in all dietary regimens (**Supplemental Figure 1L**). Daily energy expenditure increased significantly as a function of daily LBM and the influence of LBM on energy expenditure was equivalent for mice on the three dietary regimens (**Figure 1J**). We observed that IRD decreased energy expenditure as a function of LBM relative to mice pair fed CID or given CID *ad lib* (**Figure 1K)**demonstrating that IRD does not cause negative energy balance through reduced energy intake or though increasing energy expenditure.

Energy intake is a function of both caloric consumption and nutrient absorption by the gastrointestinal tract. Pancreatic-derived enzymes are essential for digestion and absorption of dietary macronutrients and excess dietary iron can contribute to dysfunction of exocrine pancreas [23]. Consistent with this, we observed a significant reduction in circulating levels of lipase in mice fed IRD, suggesting that IRD disrupts pancreatic production of lipase and subsequent ability to digest triglyceride and fats into free fatty acids and glycerol for uptake in the intestines (**Figure 1L**). As lipase inhibition is also known to reduce cholesterol absorption [24,25], we saw a corresponding decrease in circulating total cholesterol levels in mice fed IRD (**Figure 1M**). To address if IRD reduced the ability of mice to absorb dietary lipids, we performed an oral lipid tolerance test (OLTT) in mice fed CID or IRD for eight days and found that mice fed IRD exhibited a significant reduction in their ability to absorb orally administered lipids(**Figure 1N**). Finally, mice fed IRD excreted more calories in their stool and had decreased net calorie absorption from diets relative to mice fed CID(**Supplemental Figure 1M**). Taken together, our data show that IRD causes negative energy balance by causing intestinal nutrient malabsorption.

2.3.2 Iron rich diet increases lipid utilization, lipid mobilization and wasting of fat energy stores

Negative energy balance will cause mobilization of energy substrates from endogenous stores. Mobilization of the energy stores in white adipose tissue (WAT) involves the liberation of triacylglycerol from lipid droplets stored in adipose tissue that provides free fatty acids (FFA) and glycerol to other tissues and organs. Using an *ex vivo* lipolysis assay, we found that inguinal WAT (IWAT) and gonadal WAT (GWAT) from IRD-fed mice released significantly higher levels of free non-esterified fatty acids (FFA) and free glycerol compared to mice fed CID over the course of the dietary regimen (**Figure 2A-B**). Mobilization of fat stores can result in loss of body fat mass. To determine the extent of fat energy store depletion, we utilized magnetic resonance imaging (MRI) to analyze fat and lean body composition of mice fed CID or IRD for eight days. We found that the whole body wasting and increased lipid mobilization in mice fed IRD was associated with wasting of fat energy stores (**Figure 2C**). We also measured masses of representative WAT pads and found a significant reduction in the mass of IWAT, GWAT and mesenteric WAT (MWAT) in mice fed IRD (**Figure 2D-F**). MRI and direct measurement of hindlimb muscles that represent varied myofiber composition and the heart revealed that mice fed IRD also exhibit wasting of skeletal muscle but not cardiac muscle (**Figure 2C, G** and **Supplemental Figure A-B**). Further, we observed significant upregulation of two muscle-specific atrogenes, *Atrogin-1* and *Murf-1,* in gastrocnemius muscles of mice fed IRD— a hallmark of skeletal muscle wasting (**Figure 2H**) [26–28]. We also found upregulation of *Myogenin* in gastrocnemius muscles from IRD fed mice, which is associated with Type I myofiber development (**Figure 2H**) [29]. Consistent with our findings, body composition analysis of mice from our pairwise feeding experiments confirmed that fat and lean body composition were significantly reduced in the IRD *ad libitum* group relative to pair fed mice on CID (**Supplemental Figure 2C**). Similarly,

we found that mice fed IRD *ad libitum* had the greatest decrease in IWAT mass and hindlimb muscle masses after eight days on the diet regimen (**Supplemental Figure 2D-E**). In support of IRD-induced skeletal muscle wasting, we also observed the greatest upregulation of atrogene expression in gastrocnemius muscles from mice fed IRD *ad libitum* (**Supplemental Figure 2F**). Taken together, our data demonstrate that dietary iron causes lipid mobilization that results in adipose tissue wasting, as well as muscle wasting, that is independent of the initial food aversion response.

We hypothesized that the increased lipid mobilization was indicative of IRD causing a shift towards lipid utilization. To determine how IRD influences energy substrate preference, we measured respiratory exchange ratio (RER) by housing mice fed CID or IRD in the CLAMS. An RER close to 1 is indicative of carbohydrate utilization, while an RER closer to 0.7 is indicative of lipid substrate utilization [30]. Using PCA, we found that mice from the different dietary conditions exhibited distinct clustering during their day and night cycles, indicating that there were distinct RERs for each dietary condition and their respective light/dark cycles (**Figure 2I**). We found that IRD-fed mice exhibited a dramatic shift towards lipid utilization (**Figure 2J**). Increased lipid utilization is characteristic during periods of fasting when mice will draw from white adipose tissue (WAT) stores [31,32]. We therefore performed an RER area under the curve analysis for days 3-8, when food consumption was comparable between CID and IRD-fed mice to analyze energy substrate utilization independent of differences in food consumption (**Figure 2K**). We found that the IRD induced an increase in lipid utilization independent of the fasted state. We performed RER analyses for the pair fed experimental cohort and found that IRD induced a significant shift towards lipid utilization relative to pair fed mice fed CID—further demonstrating that IRD increases reliance on lipids

as an energy substrate (**Supplementary Figure 2G-I**). Interestingly, the increased reliance on lipids as an energy source did not result in a decrease in circulating lipids or glycerol in fasted mice fed CID or IRD over the course of the experiment (**Figure 2L**). Consistently, mice fed IRD had a comparable rise and clearance of FFA and triglycerides in a lipid tolerance test performed on day 9 post diet initiation, suggesting that while IRD induces a shift towards lipid utilization, this does not increase rates of lipid turnover (**Figure 2M**). Taken together, our data demonstrate that dietary iron excess causes negative net energy balance, inducing a global shift towards lipid utilization that is fueled by mobilization of endogenous fat energy stores.

2.3.3 An acute course of excess dietary iron does not induce insulin resistance

Iron metabolism can influence glucose homeostasis by altering insulin sensitivity. We previously demonstrated in C3H/HeJ mice that an acute course of dietary iron caused transient insulin resistance (IR) during infection with an enteric pathogen and that this was associated with iron overload in WAT [15]. In C57BL/6 mice it was previously shown that long-term administration of dietary iron causes IR associated with an increase in hepatic and adipose tissue iron levels as well as an increase in serum iron [33]. We found that in C57BL/6 mice, an acute course of IRD resulted in significantly higher levels of iron in the liver and serum, but not other metabolic tissues including the visceral fat (GWAT), subcutaneous fat (IWAT) and muscle (gastrocnemius) (**Figure 3A-B**). The livers of IRD fed mice were significantly smaller than that of CID ad libitum fed mice. However CID pair fed mice had comparable liver size as IRD mice indicating that the reduced food consumption amount rather than hepatic iron overload caused a reduction in liver size (**Supplemental Figure 3A-B**). IRD fed mice exhibited significantly elevated ALP levels but no difference in AST levels, and only a modest and insignificant increase in ALT levels (**Figure 3C** and **Supplemental Figure 3C-D**), suggesting that IRD may cause liver damage. Consistent with a systemic iron overloading response, IRD induced hepcidin (*Hamp*) expression in liver and significantly reduced expression of genes involved with iron uptake (*Tfr1, Dmt1*) (**Figure 3D** and **Supplemental Figure 3E**). Both GWAT and IWAT showed reduced expression of heme oxygenase-1 (*Hmox1)* which is considered to be a marker of iron overload and inflammation in adipose tissue [34]. IRD caused a reduction in transferrin expression in GWAT and reduced ferroportin (Fpn) expression in IWAT—suggesting that both visceral and subcutaneous adipose tissues depots respond to dietary iron overload (**Figure 3E-F** and **Supplemental Figure 3F-G**). IRD induced a modest reduction in gastrocnemius expression of iron uptake

genes (*Dmt1, Hmox1,* Steap2) and a significant reduction in transferrin receptor 1 (*Tfr1*) (**Figure 3G** and **Supplemental Figure 3H**).

We next asked whether an acute course of IRD could affect insulin sensitivity in C57BL/6 mice. We performed an insulin tolerance test (ITT) on days 3, 6, and 9 post-diet initiation on mice fed CID and IRD. We found no difference in insulin sensitivity between mice fed the different diets at any of the examined time points (**Figure 3H-I, Supplemental Figure 4A-J**). It has been previously demonstrated that iron overload can lead to tissue-specific insulin resistance; notably, Dongiovanni and colleagues observed insulin resistance in visceral WAT but not subcutaneous WAT in mice fed excess dietary iron [15,33]. We therefore examined activation of insulin signaling in the GWAT and IWAT, as well as the liver and gastrocnemius muscle in CID and IRD fed mice. Mice fed CID and IRD for six days were injected with insulin and tissues were harvested 15 minutes post-insulin injection and processed to measure activation of AKT, a central kinase in the intracellular insulin signaling cascade (**Figure 3J**). We found no differences in phosphorylated AKT in the GWAT from mice in either dietary condition (**Figure 3K, Supplemental Figure 5A-B**). Interestingly, we found a trend towards increased phosphorylation of AKT in the IWAT, liver, and gastrocnemius muscles from mice fed IRD (**Figure 3L-N** and **Supplemental Figure 5C-H**). Thus, our model of acute dietary iron enrichment in C57BL/6 mice causes changes in organismal lipid physiology that is not associated with insulin resistance.

2.3.4 Iron-induced lipid mobilization and adipose tissue wasting is dependent on fat-specific ATGL activity

The bulk of lipid mobilization from adipose tissue is mediated through lipolysis. In canonical adipose tissue lipolysis, triglycerides stored in lipid droplets are hydrolyzed by adipose triglyceride lipase (ATGL) and hormone-sensitive lipase (HSL) to produce free glycerol and fatty acids to be supplied into circulation and fuel peripheral tissue metabolism [35,36]. ATGL is the rate limiting lipase present on lipid droplets that is responsible for hydrolyzing triacylglycerol into diacylglycerol. We found that mice fed an IRD exhibited elevated levels of ATGL protein in both subcutaneous (IWAT) and visceral adipose tissue (GWAT) (**Figure 4A, B, Supplemental Figure 6-7)**. ATGL activity is directly regulated by its co-activator CGI-58, which is regulated by protein kinase A (PKA). Activated PKA will phosphorylate Perilipin-1 that is conjugated with CGI-58 on lipid droplet surfaces, thereby liberating CGI-58 to activate ATGL [37,38]. It was previously demonstrated that adipose tissue cultures exposed to iron rich media and human sera (transferrin rich) upregulate lipolysis in a PKA-independent manner, suggesting that iron-induced lipolysis may be regulated in a non-canonical manner, though a mechanism was not determined [20]. Contrary to previous *in vitro* observations, we found a significant increase in the levels of phosphorylated PKAc in IWAT and GWAT of IRD fed mice, indicating that iron diet leads to increased activation of PKA in WAT *in vivo* (**Figure 4A, B, Supplemental Figure 6-7)**. Finally, IRD led to an increase in the activation of the downstream lipase, HSL, in IWAT and GWAT (**Figure 4A, B, Supplemental Figure 6-7)**. Taken together, our data demonstrate that an acute course of excess dietary iron leads to increased activation of the regulators of canonical adipose lipolysis in both subcutaneous and visceral WAT.

To test if ATGL-dependent lipolysis in adipose tissue is necessary for mediating IRD-induced lipid mobilization and adipose tissue wasting, we generated a transgenic mouse model with the gene that encodes ATGL*, Pnpla2,* specifically deleted from adipose tissue (floxed *Pnpla2* x *Fab4 cre*). Using an *ex vivo* lipolysis assay, we found that the IWAT from IRD-fed mice lacking adipose-specific ATGL (floxed *Pnpla2;Fab4 cre+,* designated $Pnpla2^{WAT\ KO}$) secreted significantly less FFA and glycerol than wild type mice fed IRD (floxed *Pnpla2;Fab4 cre-,* designated $Pnpla2^{WT}$) (**Figure 4C**). Notably, we observed comparable levels of secreted FFA and glycerol from GWAT and no difference in circulating levels of FFA or glycerol between $Pnpla2^{WAT\ KO}$ and $Pnpla2^{WT}$ mice fed IRD (**Figure 4D,E**). The apparent difference in rates of lipid mobilization between subcutaneous and visceral adipose tissue may reflect a preferential pattern of organismal lipid storage across fat depots in response to dietary iron excess [39–41]. Consistent with this, $Pnpla2^{WAT\ KO}$ mice were protected from IRD-induced IWAT wasting, but were only moderately protected from wasting of visceral fat pads, GWAT and MWAT (**Figure 4F-H)**. Though we observed differences in the pattern of subcutaneous and visceral fat pad wasting, body composition analyses showed that $Pnpla2^{WAT\ KO}$ mice had significantly more total fat mass relative to $Pnpla2^{WT}$ littermates fed IRD (**Figure 4I**). Together, these data suggest that ATGL activity is necessary for IRD-induced lipolysis, lipid mobilization and fat wasting primarily in subcutaneous adipose tissue.

2.3.5 Dietary iron-induced ATGL activity in adipose tissue protects from wasting of lean energy stores

Having established a role for adipose tissue specific ATGL in IRD-mediated lipid mobilization and fat wasting, we next asked if ATGL activity in fat was required for the changes in energy balance we observed in IRD-fed mice (**Figure 2.3.1**). Despite being protected from wasting of subcutaneous fat and having a higher body fat composition (**Figure 2.3.4 F** and **I**), Pnpla2$^{WAT\ KO}$ displayed comparable total body wasting to that exhibited by their wild type littermates when fed dietary iron (**Figure 2.3.5 A, Supplemental Figure 2.3.8 A**). This suggests that mice lacking ATGL activity in adipose tissue are not protected from the negative energy balance caused by IRD. Consistent with this, we found that food consumption was comparable between Pnpla2$^{WAT\ KO}$ and their wildtype littermates when fed IRD (**Figure 2.3.5 B**). Our analyses with the CLAMS showed that energy expenditure of Pnpla2^{WT} and Pnpla2$^{WAT\ KO}$ mice was comparable under normal chow conditions (**Figure 2.3.5 C, Supplemental Figure 2.3.8 B**). Following introduction of IRD, Pnpla2^{WT} and Pnpla2$^{WAT\ KO}$ mice showed equivalent changes in energy expenditure (**Figure 2.3.5 C-D, Supplemental Figure 2.3.8 B**). When we examined the light/dark cycle EEJ for Pnpla2^{WT} and Pnpla2$^{WAT\ KO}$ mice by PCA, we saw no influence of genotype on EEJ for light or dark cycles when animals were fed IRD (**Figure 2.3.5 E**). Furthermore, we found that Pnpla2^{WT} and Pnpla2$^{WAT\ KO}$ mice fed IRD displayed comparable daily EEJ relative to daily TBM and daily LBM over the course of the experiment (**Figure 2.3.5 F-G** and **Supplemental Figure 2.3.8 C-D**). Analysis of body temperature and activity over the course of the diet regimen revealed no difference in body temperature, total activity levels, or differences in light/dark cycle activity levels between genotypes (**Supplemental Figure 2.3.8 E-H**). Taken together, our results demonstrate that ATGL activity in adipose tissue is not necessary for the effects of dietary iron on net energy balance, and does not change energy expenditure,

activity levels, basal metabolism or food consumption when animals are fed an acute course of IRD.

We hypothesized that Pnpla2$^{WAT\ KO}$ mice undergo a compensatory increase in lean energy store wasting that can account for the whole body weight loss driven by IRD. Consistent with our hypothesis, we found that Pnpla2$^{WAT\ KO}$ mice exhibited increased wasting of lean tissue stores compared to their Pnpla2^{WT} littermates fed IRD (**Figure 2.3.5 H**). These differences in body composition were specific to mice fed IRD because mice lacking ATGL in adipose tissue and their wild type littermates exhibited comparable body composition when fed control chow (**Supplemental Figure 2.3.8 I**). Direct measurement of hindlimb muscle masses similarly showed that Pnpla2$^{WAT\ KO}$ mice fed IRD had decreased mass of individual muscle groups compared to their wild type littermates fed IRD (**Figure 2.3.5 I).** As muscle mass is regulated by protein synthesis and degradation cascades in muscle, we analyzed expression of both atrogenes, *Atrogin-1* and *Murf-1*, and myogenesis factors, *MyoD* and *myogenin* in gastrocnemius of IRD-fed mice. We observed increased expression of both *Atrogin-1* and *Murf-1,* and significant downregulation of *MyoD* expression in Pnpla2$^{WAT\ KO}$ muscles, suggesting that both atrophic factors and lack of myogenesis signaling may contribute to enhanced muscle wasting in Pnpla2$^{WAT\ KO}$ fed IRD (**Figure 2.3.5 J**).

Excess dietary iron in wild type mice causes increased lipid utilization (**Figure 2.3.2**). We hypothesized that the reduced lipid mobilization and increased lean wasting in IRD-fed Pnpla2$^{WAT\ KO}$ mice would result in a decrease in global lipid utilization. Consistent with this, we observed modest separation in RER values between Pnpla2$^{WAT\ KO}$ and Pnpla2^{WT} mice following introduction of IRD (**Figure 2.3.5 K**). Principal component analysis of the light/dark

cycle RER values from Pnpla2$^{WAT\ KO}$ and Pnpla2^{WT} mice showed that the pattern of clustering is based on the light vs. dark cycle and independent of genotype (**Figure 2.3.5 L**). We therefore analyzed AUC of RER by light/dark cycles and observed a significant increase in Pnpla2$^{WAT\ KO}$ RER values during the light cycle following introduction of IRD (**Figure 2.3.5 M**). This suggests that during the diurnal "fasting" state, Pnpla2$^{WAT\ KO}$ mice fed IRD utilized less lipid substrates relative to Pnpla2^{WT} littermates (**Figure 2.3.5 M**). Thus, ATGL activity in adipose tissue protects from lean energy store wasting by promoting lipolysis and lipid mobilization in response to IRD-induced negative energy balance (**Figure 2.3.5 N**).

2.4 Discussion

Organismal macronutrient metabolism is intimately linked to micronutrient metabolism. While a role for iron in regulating lipid metabolism is well appreciated, the mechanistic underpinnings of these regulatory processes are unknown. Here, using an acute course of dietary iron excess, we demonstrate that iron causes profound changes in whole organismal metabolism including nutrient malabsorption and lipid mobilization, resulting in a negative energy balance. We demonstrate that lipid mobilization is dependent on ATGL activity in adipose tissue and that this lipid mobilization protects from cachexia. While our data support a model that the systemic effects of iron and nutrient absorption lead to ATGL activation, lipolysis and lipid mobilization, it is formally possible that in addition to these systemic effects iron also directly acts on adipocytes to induce ATGL activity (**Figure 5N**) [20].

We found that an acute course of excess dietary iron caused reduced energy expenditure in mice, and we propose that this is due to a hypometabolic state triggered by the reduced nutrient absorption caused by IRD. Nutrient absorption is largely dependent on proper digestion of macronutrients in the duodenum via digestive enzymes secreted by the exocrine pancreas [23]. Iron overload disorders that lead to deposition of iron in parenchymal tissues, like liver and pancreas, are associated with metabolic syndrome and reduced levels of circulating pancreatic-derived digestive enzymes [23,42,43]. It has been proposed that pancreatic insufficiency caused by iron loading may contribute to malabsorption issues observed in individuals with iron overload disorders [43].

Our finding that IRD decreases serum levels of lipase is consistent with experimental and clinical models of iron-overload induced pancreatic dysfunction and atrophy of exocrine

pancreatic acinar cells. Further, we observed reduced cholesterol levels in mice fed IRD, which is consistent with pharmacologic inhibition of lipase activity [24,25]. In further support of IRD-induced pancreatic insufficiency, lipid absorption was severely blunted in mice fed IRD and we observed decreased net calorie absorption in mice fed IRD. Though we predict that IRD-induced nutrient malabsorption extends to insufficient digestion of proteins and carbohydrates as well, we did not measure levels of other pancreatic-derived digestive enzymes in the current study. It is important to note that while our study implicates iron-induced pancreatic insufficiency in reduced nutrient uptake, iron metabolism can just as likely affect nutrient absorption and turnover through a systemic mechanism independent of digestive function. For example, our lab previously showed that excess dietary iron can indirectly affect luminal macronutrient content through inducing insulin resistance [15]. Furthermore, iron can also influence the the microbial landscape of the gut and contribute to gastrointestinal inflammation, compromise barrier integrity and regulate iron metabolism at the local level to control infection [44,45] . Excess iron is known to drive expansion of facultative anaerobes like *Enterobacteriaceae*, thus displacing and driving competition against *Lactobacillus* and Firmicutes. [13]. Moreover, it was recently demonstrated that iron supplementation can similarly influence microbiome composition independent of the route of administration [46]. Altogether, these findings highlight the diverse role of micronutrient metabolism on nutritional status beyond nutrient absorption and digestive function.

It has been previously reported that when fed a chronic 16-week course of dietary iron, C57BL/6 mice develop IR specifically in visceral adipose depots as well as impaired organismal insulin tolerance [33]. In our study, we used an acute course of dietary iron and found that C57BL/6 mice did not develop IR in adipose tissue, skeletal muscle or liver, and

also showed no changes in organismal insulin tolerance. The discrepancies between our study and that of Dongiovanni et al. may be due to the length of the feeding regimens and suggests that in C57BL/6 mice that the IR caused by excess dietary iron may be largely influenced by length of the dietary iron regimen. In a mouse model of infectious colitis using C3H/HeJ, an acute course of dietary iron excess resulted in IR in visceral adipose tissue and changes in organismal glucose tolerance [15], suggesting that the ability of a short course of dietary iron to cause IR may be mouse strain specific. It is well established that inbred mouse strains have differences in iron physiology including basal differences in tissue iron content. C75BL/6 mice in particular, have a dampened iron-overloading response following introduction to an iron rich diet (Clothier et al., 1999; Dupic, 2002; Leboeuf et al., 1995; Morse et al., 1999).

When considering the physiological differences in iron handling between C3H and C57BL/6 mice that could contribute to differential manifestations in IR development, it is important to note that C57BL/6 mice lack functional *Nramp1* while C3H have a viable *Nramp1* allele. Though *Nramp1* does not appear to be directly involved in tissue iron loading, it has been shown to be important for heme recycling and influence hepcidin expression. Failure to release heme-derived iron from macrophages dampens hepcidin signaling—leading to increased basal iron uptake. Mice lacking *Nramp1* accumulate iron in liver and spleen following erythrophagocytotic stimuli *in vivo* [51]. The differences in the studies of Sanchez et al and our work also suggest that the effects of excess dietary iron on IR may be dependent on the disease state of the host, and that under conditions in which homeostasis is disrupted, as observed during infection, the short course of excess iron may be sufficient to induce IR. Future studies addressing the role of *Nramp1* in mediating the IR response to

dietary iron in different mouse strains and an understanding of the role of acute dietary iron excess in disease states are needed.

Subcutaneous fat (SAT) is considered to have greater flux in terms of storage and mobilization capacity compared to visceral fat (VAT). Specifically, excess lipids are preferentially stored in SAT, and mobilized from SAT to accommodate negative energy balance [39–41]. We found that an acute course of dietary iron induces wasting and mobilization of SAT and VAT indiscriminately and to a similar degree, suggesting that dietary iron excess leads to lipid mobilization events in a unconventional pattern that operates in response to negative energy balance. Curiously, we found that mice lacking adipose-specific ATGL are protected from iron-induced fat wasting in SAT, but not VAT. We demonstrated that IWAT and GWAT have comparable levels of ATGL protein expression and activation of the PKA signaling cascade upon introduction of IRD. Therefore, the difference in fat wasting between SAT and VAT cannot be attributed to differences in ATGL expression or activation through the PKA cascade. Though PKA activation is considered the canonical signaling cascade for ATGL activation, other pathways can alter ATGL activity including PKC, MAP kinase, PI3K, NF-κB and lipid peroxidation resulting from Fenton and Haber Weiss reactions [20,52–54]. Indeed, in an *in vitro* study utilizing visceral adipocytes from rats, iron induced lipolysis independent of the PKA lipolytic cascade, and was proposed to occur through increased levels of lipid peroxides [20]. In the current study, our data supports a model where iron induces lipolysis in SAT via the canonical PKA-ATGL cascade, however we propose that VAT is more sensitive to iron-derived lipolytic stimuli such as lipid peroxides or ROS.

We found that an acute course of dietary iron excess caused cachexia with IRD-fed animals exhibiting wasting of muscles with varied oxidative capacity and myofiber composition, suggesting that iron induces muscle wasting in an indiscriminate manner. Cachexia is dependent on the transcriptional upregulation of two muscle specific E3 ubiquitin ligases, *Murf-1* and *Atrongin-1* [26–28]. In agreement with this, we found that iron-induced cachexia was associated with the transcriptional upregulation of *Murf-1* and *Atrogin-1* in wasting hindlimb muscles. Iron-induced muscle wasting was more severe in IRD-fed animals lacking ATGL function in adipose tissue. We propose that this increase in the cachectic response in $ATGL^{WATKO}$ mice is necessary to supply muscle-derived substrates to meet the iron-induced heightened energetic demands when lipid mobilization is impaired. In support of this, we observed that $ATGL^{WATKO}$ mice fed IRD displayed a significant shift towards carbohydrate utilization during light cycles in metabolic cages. Our finding is consistent with previous reports highlighting a diurnal pattern of WAT lipolysis driven by circadian clock transcription factors CLOCK and BMAL (both *in vivo* and *ex vivo*). Light cycles represent the diurnal murine “fasting cycle” where they preferentially utilize lipids for energy, which is dependent on circadian regulation of HSL and ATGL in WAT [17,55] . We propose that $ATGL^{WATKO}$ mice fed an IRD undergo increased gluconeogenesis during a prolonged period of inactivity—a process that relies on supply of muscle-derived amino acid substrates [56], to meet the increased energetic demands induced by the diet. Interestingly, we found upregulation of *Myogenin* in gastrocnemius muscles from IRD-fed mice, which is a muscle comprised of both Type I and Type II myofibers. As *Myogenin* expression is associated with Type I myofiber development, this may represent adaptive remodeling of muscles to accommodate increased reliance on lipids/beta-oxidation [29,56], that may be necessary to meet the energetic demands caused by the acute course of dietary iron excess. In summary, this work defines the mechanistic basis for dietary iron-induced lipid mobilization in response

to negative energy balance and highlights the multi-faceted role of iron regulation of organismal metabolism.

2.5 Acknowledgements

This chapter is largely adapted from the material as it appears in: **Romero, A.R**., Mu, A., Ayres, J.S., Adipose triglyceride lipase mediates lipolysis and lipid mobilization in response to iron-mediated negative energy balance, *iScience* (2022), doi: https://doi.org/10.1016/j.isci.2022.103941. The dissertation author was the primary investigator and first author of this manuscript. The authors would like to thank Dr. Sihao Liu, Dr. Gencer Sancar, and Dr. Emmanuel Gasser (Evans Lab at Salk) for excellent methodical assistance, stimulating and insightful discussion, and generosity; Kaito Kikuchi (Suel Lab at UCSD) for providing guidance and assistance for analyses of metabolic data; Daniela Michel-Romo for providing technical support in a pair fed animal study, and Caroline Gordon for reliable assistance with animal husbandry. Finally, the authors offer thanks to members of the Ayres Laboratory for helpful discussion and technical assistance as needed. This work was supported by an NIH awards DP1 AI144249 and R01AI114929 (JSA), and the NOMIS Foundation (JSA).

2.6 References

1. Argilés, J. M., Fontes-Oliveira, C. C., Toledo, M., López-Soriano, F. J. & Busquets, S. Cachexia: a problem of energetic inefficiency. *J. Cachexia Sarcopenia Muscle* **5**, 279–286 (2014).

2. Spiegelman, B. M. & Flier, J. S. Obesity and the Regulation of Energy Balance. *Cell* **104**, 531–543 (2001).

3. O'Neill, S. & O'Driscoll, L. Metabolic syndrome: a closer look at the growing epidemic and its associated pathologies. *Obes. Rev.* **16**, 1–12 (2015).

4. Tune, J. D., Goodwill, A. G., Sassoon, D. J. & Mather, K. J. Cardiovascular consequences of metabolic syndrome. *Transl. Res.* **183**, 57–70 (2017).

5. Carrero, J. J., Stenvinkel, P., Cuppari, L., Ikizler, T. A., Kalantar-Zadeh, K., Kaysen, G., Mitch, W. E., Price, S. R., Wanner, C., Wang, A. Y. M., ter Wee, P. & Franch, H. A. Etiology of the Protein-Energy Wasting Syndrome in Chronic Kidney Disease: Consensus Statement From the International Society of Renal Nutrition and Metabolism (ISRNM). *J. Ren. Nutr.* **23**, 77–90 (2013).

6. Dobner, J. & Kaser, S. Body mass index and the risk of infection - from underweight to obesity. *Clin. Microbiol. Infect.* **24**, 24–28 (2018).

7. Rausch, V., Sala, V., Penna, F., Porporato, P. E. & Ghigo, A. Understanding the common mechanisms of heart and skeletal muscle wasting in cancer cachexia. *Oncogenesis* **10**, 1–13 (2021).

8. Ikeda, Y., Enomoto, H., Tajima, S., Izawa-Ishizawa, Y., Kihira, Y., Ishizawa, K., Tomita, S., Tsuchiya, K. & Tamaki, T. Dietary iron restriction inhibits progression of diabetic nephropathy in *db/db* mice. *Am. J. Physiol.-Ren. Physiol.* **304**, F1028–F1036 (2013).

9. Yook, J.-S., Zhou, M., Jaekwon, L. & Chung, S. Iron Deficiency Anemia (IDA) Promotes Visceral Obesity Due to Defective Adipose Tissue Browning (OR09-07-19). *Curr. Dev. Nutr.* **3**, (2019).

10. Gao, Y., Li, Z., Gabrielsen, J. S., Simcox, J. A., Lee, S., Jones, D., Cooksey, B., Stoddard, G., Cefalu, W. T. & McClain, D. A. Adipocyte iron regulates leptin and food intake. *J. Clin. Invest.* **125**, 3681–3691 (2015).

11. Lawless, J. W., Latham, M. C., Stephenson, L. S., Kinoti, S. N. & Pertet, A. M. Iron Supplementation Improves Appetite and Growth in Anemic Kenyan Primary School Children. *J. Nutr.* **124**, 645–654 (1994).

12. Stoltzfus, R. J., Chway, H. M., Montresor, A., Tielsch, J. M., Jape, J. K., Albonico, M. & Savioli, L. Low Dose Daily Iron Supplementation Improves Iron Status and Appetite but Not Anemia, whereas Quarterly Anthelminthic Treatment Improves Growth, Appetite and Anemia in Zanzibari Preschool Children. *J. Nutr.* **134**, 348–356 (2004).

13. Yilmaz, B. & Li, H. Gut Microbiota and Iron: The Crucial Actors in Health and Disease. *Pharmaceuticals* **11**, 98 (2018).

14. Niepel, D., Klag, T., Malek, N. P. & Wehkamp, J. Practical guidance for the management of iron deficiency in patients with inflammatory bowel disease. *Ther. Adv. Gastroenterol.* **11**, 1756284818769074 (2018).

15. Sanchez, K. K., Chen, G. Y., Schieber, A. M. P., Redford, S. E., Shokhirev, M. N., Leblanc, M., Lee, Y. M. & Ayres, J. S. Cooperative Metabolic Adaptations in the Host Can Favor Asymptomatic Infection and Select for Attenuated Virulence in an Enteric Pathogen. *Cell* **175**, 146-158.e15 (2018).

16. Brownlie, T., Utermohlen, V., Hinton, P. S. & Haas, J. D. Tissue iron deficiency without anemia impairs adaptation in endurance capacity after aerobic training in previously untrained women. *Am. J. Clin. Nutr.* **79**, 437–443 (2004).

17. Duncan, R. E., Ahmadian, M., Jaworski, K., Sarkadi-Nagy, E. & Sul, H. S. Regulation of Lipolysis in Adipocytes. *Annu. Rev. Nutr.* **27**, 79–101 (2007).

18. Degerman, E., Landström, T. R., Wijkander, J., Holst, L. S., Ahmad, F., Belfrage, P. & Manganiello, V. Phosphorylation and Activation of Hormone-Sensitive Adipocyte Phosphodiesterase Type 3B. *Methods* **14**, 43–53 (1998).

19. Wijkander, J., Landström, T. R., Manganiello, V., Belfrage, P. & Degerman, E. Insulin-Induced Phosphorylation and Activation of Phosphodiesterase 3B in Rat Adipocytes: Possible Role for Protein Kinase B But Not Mitogen-Activated Protein Kinase or p70 S6 Kinase*. *Endocrinology* **139**, 219–227 (1998).

20. Rumberger, J. M., Peters, T., Burrington, C. & Green, A. Transferrin and Iron Contribute to the Lipolytic Effect of Serum in Isolated Adipocytes. *Diabetes* **53**, 2535–2541 (2004).

21. Ryan, B. J., Pelt, D. W. V., Guth, L. M., Ludzki, A. C., Gioscia-Ryan, R. A., Ahn, C., Foug, K. L. & Horowitz, J. F. Plasma ferritin concentration is positively associated with in vivo fatty acid mobilization and insulin resistance in obese women. *Exp. Physiol.* **103**, 1443–1447 (2018).

22. Devasthali, S. D., Gor-deuk, V. R., Brittenham, G. M., Bravo, J. R., Hughes, M. A. & Keating, L. J. Bioavailability of carbonyl iron: A randomized, double-blind study. *Eur. J. Haematol.* **46**, 272–278 (1991).

23. Kimita, W. & Petrov, M. S. Iron metabolism and the exocrine pancreas. *Clin. Chim. Acta* **511**, 167–176 (2020).

24. Erdmann, J., Lippl, F., Klose, G. & Schusdziarra, V. Cholesterol lowering effect of dietary weight loss and orlistat treatment – efficacy and limitations. *Aliment. Pharmacol. Ther.* **19**, 1173–1179 (2004).

25. Ke, J., An, Y., Cao, B., Lang, J., Wu, N. & Zhao, D. Orlistat-Induced Gut Microbiota Modification in Obese Mice. *Evid. Based Complement. Alternat. Med.* **2020**, 1–9 (2020).

26. Baehr, L. M., Furlow, J. D. & Bodine, S. C. Muscle sparing in muscle RING finger 1 null mice: response to synthetic glucocorticoids. *J. Physiol.* **589**, 4759–4776 (2011).

27. Bodine, S. C., Latres, E., Baumhueter, S., Lai, V. K., Nunez, L., Clarke, B. A., Poueymirou, W. T., Panaro, F. J., Na, E., Dharmarajan, K., Pan, Z. Q., Valenzuela, D. M., DeChiara, T. M., Stitt, T. N., Yancopoulos, G. D. & Glass, D. J. Identification of ubiquitin ligases required for skeletal muscle atrophy. *Science* **294**, 1704–1708 (2001).

28. Gomes, M. D., Lecker, S. H., Jagoe, R. T., Navon, A. & Goldberg, A. L. Atrogin-1, a muscle-specific F-box protein highly expressed during muscle atrophy. *Proc. Natl. Acad. Sci. U. S. A.* **98**, 14440–14445 (2001).

29. Hughes, S. M., Chi, M. M.-Y., Lowry, O. H. & Gundersen, K. Myogenin Induces a Shift of Enzyme Activity from Glycolytic to Oxidative Metabolism in Muscles of Transgenic Mice. *J. Cell Biol.* **145**, 633–642 (1999).

30. Speakman, J. R. Measuring Energy Metabolism in the Mouse – Theoretical, Practical, and Analytical Considerations. *Front. Physiol.* **4**, (2013).

31. Rosen, E. D. & Spiegelman, B. M. Adipocytes as regulators of energy balance and glucose homeostasis. *Nature* **444**, 847–853 (2006).

32. Schmidt-Nielsen, K. *Animal Physiology: Adaptation and Environment*. (Cambridge University Press, 1997).

33. Dongiovanni, P., Ruscica, M., Rametta, R., Recalcati, S., Steffani, L., Gatti, S., Girelli, D., Cairo, G., Magni, P., Fargion, S. & Valenti, L. Dietary Iron Overload Induces Visceral Adipose Tissue Insulin Resistance. *Am. J. Pathol.* **182**, 2254–2263 (2013).

34. Moreno-Navarrete, J. M., Ortega, F., Rodríguez, A., Latorre, J., Becerril, S., Sabater-Masdeu, M., Ricart, W., Frühbeck, G. & Fernández-Real, J. M. HMOX1 as a marker of iron excess-induced adipose tissue dysfunction, affecting glucose uptake and respiratory capacity in human adipocytes. *Diabetologia* **60**, 915–926 (2017).

35. Haemmerle, G., Lass, A., Zimmermann, R., Gorkiewicz, G., Meyer, C., Rozman, J., Heldmaier, G., Maier, R., Theussl, C., Eder, S., Kratky, D., Wagner, E. F., Klingenspor, M., Hoefler, G. & Zechner, R. Defective lipolysis and altered energy metabolism in mice lacking adipose triglyceride lipase. *Science* **312**, 734–737 (2006).

36. Zimmermann, R., Strauss, J. G., Haemmerle, G., Schoiswohl, G., Birner-Gruenberger, R., Riederer, M., Lass, A., Neuberger, G., Eisenhaber, F., Hermetter, A. & Zechner, R. Fat mobilization in adipose tissue is promoted by adipose triglyceride lipase. *Science* **306**, 1383–1386 (2004).

37. Gruber, A., Cornaciu, I., Lass, A., Schweiger, M., Poeschl, M., Eder, C., Kumari, M., Schoiswohl, G., Wolinski, H., Kohlwein, S. D., Zechner, R., Zimmermann, R. & Oberer, M. The N-terminal region of comparative gene identification-58 (CGI-58) is important for lipid droplet binding and activation of adipose triglyceride lipase. *J. Biol. Chem.* **285**, 12289–12298 (2010).

38. Lass, A., Zimmermann, R., Haemmerle, G., Riederer, M., Schoiswohl, G., Schweiger, M., Kienesberger, P., Strauss, J. G., Gorkiewicz, G. & Zechner, R. Adipose triglyceride lipase-mediated lipolysis of cellular fat stores is activated by CGI-58 and defective in Chanarin-Dorfman Syndrome. *Cell Metab.* **3**, 309–319 (2006).

39. Luong, Q., Huang, J. & Lee, K. Y. Deciphering White Adipose Tissue Heterogeneity. *Biology* **8**, E23 (2019).

40. Schoettl, T., Fischer, I. P. & Ussar, S. Heterogeneity of adipose tissue in development and metabolic function. *J. Exp. Biol.* **221**, jeb162958 (2018).

41. Tchkonia, T., Thomou, T., Zhu, Y., Karagiannides, I., Pothoulakis, C., Jensen, M. D. & Kirkland, J. L. Mechanisms and Metabolic Implications of Regional Differences among Fat Depots. *Cell Metab.* **17**, 644–656 (2013).

42. Gullo, L., Corcioni, E., Brancati, C., Bria, M., Pezzilli, R. & Sprovieri, G. Morphologic and Functional Evaluation of the Exocrine Pancreas in p-Thalassemia Major. 5 (1993).

43. Horne, W. I., Tandler, B., Dubick, M. A., Niemelä, O., Brittenham, G. M. & Tsukamoto, H. Iron Overload in the Rat Pancreas Following Portacaval Shunting and Dietary Iron Supplementation. *Exp. Mol. Pathol.* **64**, 90–102 (1997).

44. Bessman, N. J., Mathieu, J. R. R., Renassia, C., Zhou, L., Fung, T. C., Fernandez, K. C., Austin, C., Moeller, J. B., Zumerle, S., Louis, S., Vaulont, S., Ajami, N. J., Sokol, H., Putzel, G. G., Arvedson, T., Sockolow, R. E., Lakhal-Littleton, S., Cloonan, S. M., Arora, M., Peyssonnaux, C. & Sonnenberg, G. F. Dendritic cell–derived hepcidin sequesters iron from the microbiota to promote mucosal healing. *Science* **368**, 186–189 (2020).

45. Yilmaz, B. & Li, H. Gut Microbiota and Iron: The Crucial Actors in Health and Disease. *Pharm. Basel Switz.* **11**, E98 (2018).

46. La Carpia, F., Wojczyk, B. S., Annavajhala, M. K., Rebbaa, A., Culp-Hill, R., D'Alessandro, A., Freedberg, D. E., Uhlemann, A.-C. & Hod, E. A. Transfusional iron overload and intravenous iron infusions modify the mouse gut microbiota similarly to dietary iron. *Npj Biofilms Microbiomes* **5**, 1–11 (2019).

47. Clothier, B., Robinson, S., Akhtar, R. A., Francis, J. E., Peters, T. J., Raja, K. & Smith, A. G. Genetic variation of basal iron status, ferritin and iron regulatory protein in mice: potential for modulation of oxidative stress. *Biochem. Pharmacol.* **59**, 115–122 (2000).

48. Dupic, F. Duodenal mRNA expression of iron related genes in response to iron loading and iron deficiency in four strains of mice. *Gut* **51**, 648–653 (2002).

49. Leboeuf, R. C., Tolson, D. & Heinecke, J. W. Dissociation between tissue iron concentrations and transferrin saturation among inbred mouse strains. *J. Lab. Clin. Med.* **126**, 128–136 (1995).

50. Morse, A. C., Beard, J. L. & Jones, B. C. A genetic developmental model of iron deficiency: biological aspects. *Proc. Soc. Exp. Biol. Med. Soc. Exp. Biol. Med. N. Y. N* **220**, 147–152 (1999).

51. Soe-Lin, S., Apte, S. S., Andriopoulos, B., Andrews, M. C., Schranzhofer, M., Kahawita, T., Garcia-Santos, D. & Ponka, P. Nramp1 promotes efficient macrophage recycling of iron following erythrophagocytosis in vivo. *Proc. Natl. Acad. Sci.* **106**, 5960–5965 (2009).

52. Rejholcova, M., Wilhelm, J. & Svoboda, P. Lipid peroxidation inhibits norepinephrine-stimulated lipolysis in rat adipocytes. Reduction of beta-adreno-ceptor number. *Biochem. Biophys. Res. Commun.* **150**, 802–810 (1988).

53. Winterbourn, C. C. Toxicity of iron and hydrogen peroxide: the Fenton reaction. *Toxicol. Lett.* **82–83**, 969–974 (1995).

54. Yang, W. S. & Stockwell, B. R. Ferroptosis: Death by Lipid Peroxidation. *Trends Cell Biol.* **26**, 165–176 (2016).

55. Shostak, A., Meyer-Kovac, J. & Oster, H. Circadian Regulation of Lipid Mobilization in White Adipose Tissues. *Diabetes* **62**, 2195–2203 (2013).

56. Wu, J. W., Wang, S. P., Casavant, S., Moreau, A., Yang, G. S. & Mitchell, G. A. Fasting energy homeostasis in mice with adipose deficiency of desnutrin/adipose triglyceride lipase. *Endocrinology* **153**, 2198–2207 (2012).

Figure 2.3.1 Iron rich diet causes negative energy balance and nutrient malabsorption
Six-week old C57BL/6 males were given control diet (CID) or 2% carbonyl iron diet (IRD) and individually housed in static or metabolic cages in the Comprehensive Laboratory Animal Monitoring System (CLAMS). Weight, energy expenditure and food consumption were monitored. (**A**) Percent original weight over eight-day diet regimen on CID or IRD. Data shown represents two pooled independent experiments (n=11 mice per group). (**B**) Hourly energy expenditure and corresponding area under the curve analysis for mice fed CID or IRD for eight days in CLAMS. White and black/grey boxes/shaded region represent light/dark cycles respectively. Data shown represents one independent experiment (n=5-6 mice per group). (**C**) Principal component analysis of energy expenditure in (**B**) for CID and IRD fed mice in light/dark cycles. Ellipses are indicative of 95% confidence intervals. Data shown represents analysis of one independent experiment (n=5-6 mice per group). (**D**) Linear regression analysis of daily energy expenditure as a function of daily lean body mass (LBM) over eight day period and corresponding (**E**) ANCOVA-predicted EEJ at group average LBM of 15.589 g. Dotted vertical line in (**D**) represents group average lean mass (CID linear regression, R^2=.1467, F=7.735, dF=1, 45, *P*=0.0079, Y = 568.2*X + 30500; IRD linear regression, R^2=.1396, F=5.841, dF=1, 36 , *p*=0.0208, Y = 519.6*X + 27524; pooled slope=534.5) Data shown represents analysis of one independent experiment (n=5-6 mice per group). (**F**) Average daily food consumption of mice fed CID or IRD**.** Data shown represents two pooled independent experiments (n= 11 mice per group). (**G-K**) C57BL/6 male mice were fed CID *ad libitum* (*ad lib)*, IRD *ad libitum* (*ad lib)*, or CID pair fed matched to average historical iron food consumption values. (**G**) Percent original body weight for dietary regimens shown. Data shown represents two pooled independent experiments (n= 9 mice per group). Blue asterisks denote comparisons between CID *ad lib* and CID pair fed. Gray asterisks denote comparisons between CID pair fed and IRD *ad lib*. Peach asterisks denote comparisons between CID *ad lib* and IRD *ad lib*. (**H**) Hourly energy expenditure and corresponding area under the curve analysis for mice on three dietary regimens. White and black/grey boxes/shaded region represent light/dark cycles respectively. Data shown represents one independent experiment (n= 4 mice per group) (**I**) Principal component analyses of energy expenditure in (**H**) for light/dark cycles of three dietary regimens. Ellipses are indicative of 95% confidence intervals. Data shown represents analyses of one independent experiment (n= 4 mice per group) (**J**) Regression-based analysis of absolute daily EEJ against daily lean mass over eight day period and corresponding (**K**) ANCOVA-predicted EEJ at group average lean mass of 15.359 g. Dotted vertical line in regression plot represents group average lean mass (CID *ad lib* linear regression, R^2=.2913, F=13.98, dF=1,34, *P*=0.0007, Y = 646.6*X + 38295; CID pair fed linear regression, R^2=.2585, F=11.85, dF=1,34, *p*=0.0015, Y =906.9*X + 29379; IRD *ad lib* linear regression, R^2=.2204, F=9.61, dF=1,34 , *P*=0.0039, Y = 1982*X + 11641; pooled slope=1159). Data shown represents analysis of one independent experiment (n= 4 mice per group). (**L-M**) Circulating levels of (**L**) Lipase and (**M**) total cholesterol in serum on day 9 of diet regimen. Data shown represents one independent experiment (n= 5 mice per group) **(N)** Oral lipid tolerance test of mice fed CID or IRD for eight days. Data shown represents analysis of two pooled independent experiments (n=10 mice per group)All CLAMS data plotted in zeitgeber time. Data represent mean ±SEM; CID **P*<0.05, ***P*<0.01, ****P*<0.001, *****P*<0.0001. Related to **Supplemental Figure 2.3.1**

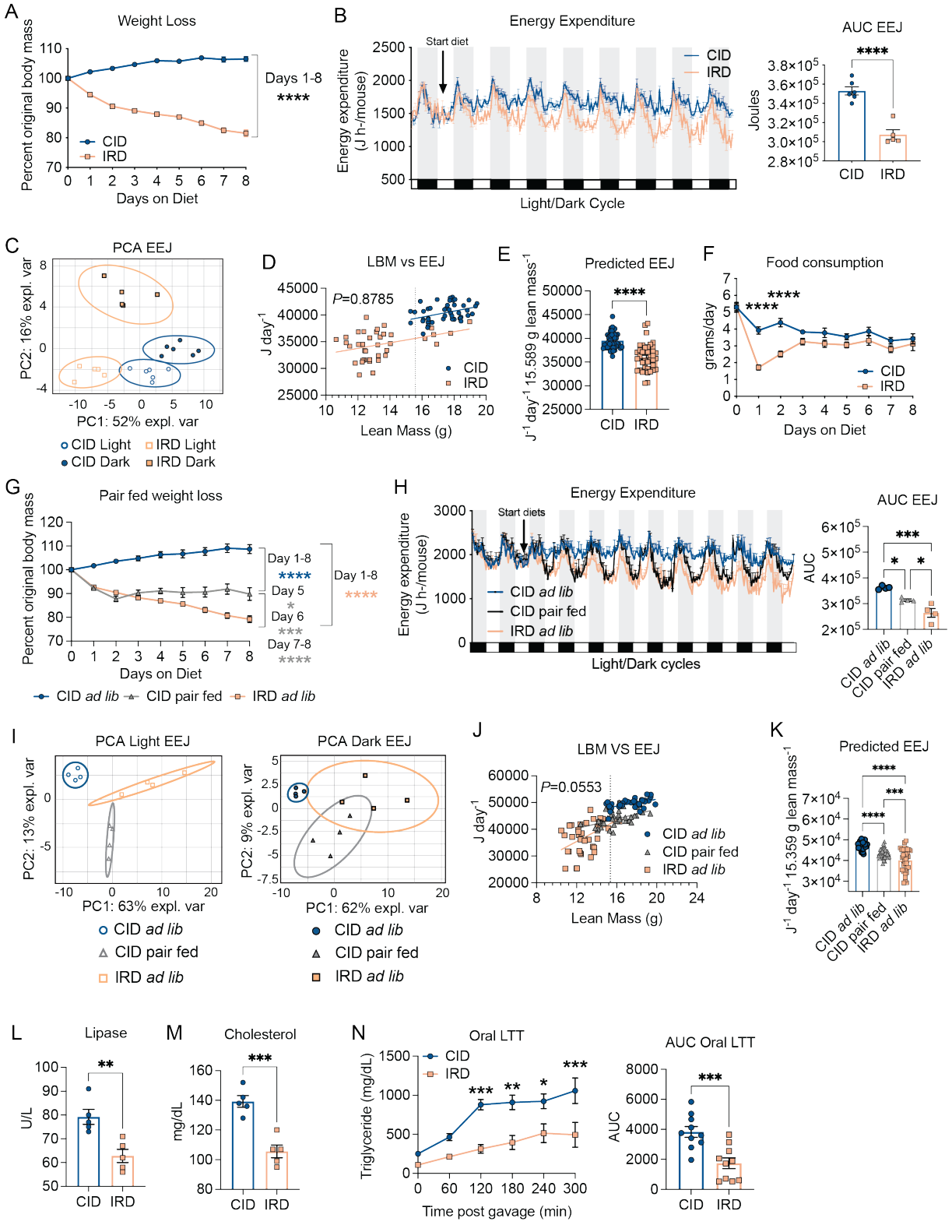
A
Weight Loss
Percent original body mass
Days on Diet
CID
IRD
Days 1-8
****
B
Energy Expenditure
Start diet
Energy expenditure (J h-/mouse)
Light/Dark Cycle
CID
IRD
AUC EEJ
Joules
****
C
PCA EEJ
PC2: 16% expl. var
PC1: 52% expl. var
CID Light
IRD Light
CID Dark
IRD Dark
D
LBM vs EEJ
P=0.8785
J day-1
Lean Mass (g)
E
Predicted EEJ
J-1 day-1 15.589 g lean mass-1
****
F
Food consumption
grams/day
Days on Diet
****
G
Pair fed weight loss
Percent original body mass
Days on Diet
Day 1-8 ****
Day 5 *
Day 6 ***
Day 7-8 ****
Day 1-8 ****
CID ad lib
CID pair fed
IRD ad lib
H
Energy Expenditure
Start diets
Energy expenditure (J h-/mouse)
Light/Dark cycles
CID ad lib
CID pair fed
IRD ad lib
AUC EEJ
AUC
I
PCA Light EEJ
PCA Dark EEJ
PC2: 13% expl. var
PC1: 63% expl. var
PC2: 9% expl. var
PC1: 62% expl. var
CID ad lib
CID pair fed
IRD ad lib
J
LBM VS EEJ
P=0.0553
J day-1
Lean Mass (g)
K
Predicted EEJ
J-1 day-1 15.359 g lean mass-1
L
Lipase
U/L
**
M
Cholesterol
mg/dL
***
N
Oral LTT
Triglyceride (mg/dL)
Time post gavage (min)
AUC Oral LTT
AUC
***

Figure 2.3.2 Excess dietary iron induces lipid mobilization from white adipose tissue (WAT) that is associated with increased lipid utilization and wasting of fat energy stores

Six-week old C57BL/6 males were provided control (CID) or 2% carbonyl iron diet (IRD) for 3, 6, or 9 days. **(A-B)** *Ex vivo* lipolysis assay measuring glycerol and free fatty acids (FFA) released from **(A)** IWAT **(B)** and GWAT**.** Data shown represents one independent experiment (n=5 mice per group). **(C)** Body composition analyses using EchoMRI of mice fed CID or IRD for 6 days. Fat and lean mass were normalized to original body mass. Data shown represents two pooled independent experiments (n=11 mice per group)**. (D-F)** Tissue masses of **(D)** IWAT **(E)** GWAT and **(F)** MWAT from mice fed CID or IRD for 6 days**.** Data shown for **D,E** represents two pooled independent experiments (n=10 mice per group). Data shown for **F** represents one independent experiment (n=5 mice per group)**. (G)** Muscle masses from hindlimb of mice fed CID or IRD for 8 days (Quadricep; Quad , tibialis anterior; TA, extensor digitorum longus; EDL, soleus, and gastrocnemius; Gastro). Data shown represents one independent experiment (n=5 mice per group). **(H)** Gene expression in gastrocnemius of mice fed CID or IRD for 8 days. Gene expression was normalized to housekeeping expression of *Rps17*. Data shown represents one independent experiment (n=4 mice per group). **(I-K)** Mice were housed in the CLAMS and given CID or IRD. The respiratory exchange ratio over the course of the experiment was determined. **(I)** Principal component analysis for the respiratory exchange ratio (RER) of CID and IRD fed mice in light/dark cycles. Ellipses are indicative of 95% confidence intervals. Data shown represents analyses of one independent experiment (n=6 mice per group). **(J)** Average hourly respiratory exchange ratio of mice fed CID or IRD (RER) calculated as ratio of ml CO_2 OUT (respired):ml O_2 IN (inhaled). Data shown represents one independent experiment (n=6 mice per group). **(K)** Area under the curve analysis for RER for period of matched food consumption. **(L)** Circulating levels of glycerol and FFA in serum of fasted CID or IRD mice on days 3, 6, and 9 of diet time course. Data shown represents one independent experiment (n=5 mice per group). **(M)** Intraperitoneal lipid tolerance test (i.p. LTT) performed on fasted mice fed CID or IRD for nine days. Data shown represents one independent experiment (n=5 mice per group). Data represent mean ±SEM; **P*<0.05, ***P*<0.01, ****P*<0.001, *****P*<0.0001. Related to **Supplemental Figure 2.3.2**

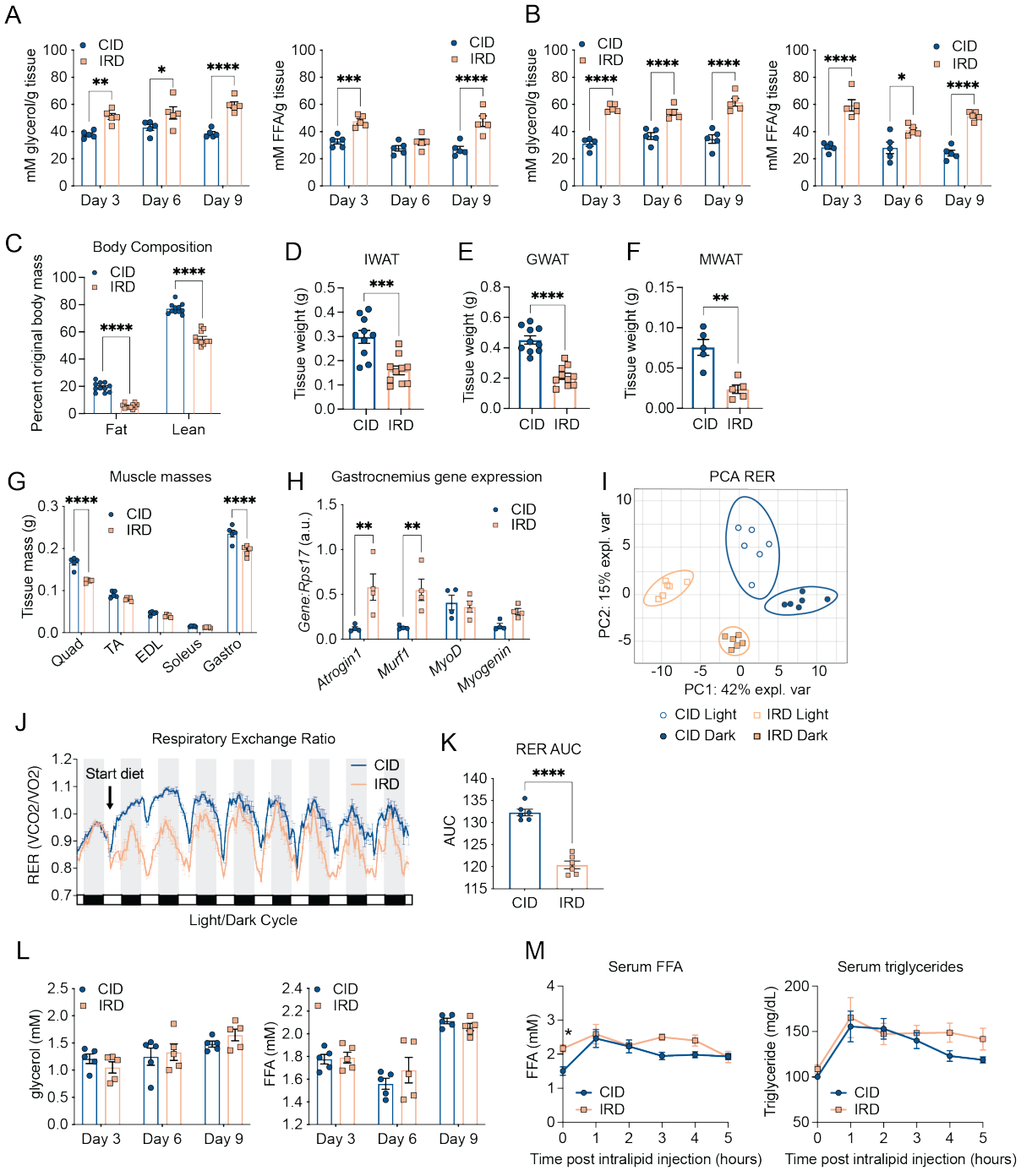
A
mM glycerol/g tissue
mM FFA/g tissue
CID
IRD
Day 3
Day 6
Day 9
B
C
Body Composition
Percent original body mass
Fat
Lean
D
IWAT
Tissue weight (g)
E
GWAT
F
MWAT
G
Muscle masses
Tissue mass (g)
Quad
TA
EDL
Soleus
Gastro
H
Gastrocnemius gene expression
Gene:Rps17 (a.u.)
Atrogin1
Murf1
MyoD
Myogenin
I
PCA RER
PC2: 15% expl. var
PC1: 42% expl. var
CID Light
IRD Light
CID Dark
IRD Dark
J
Respiratory Exchange Ratio
RER (VCO2/VO2)
Start diet
Light/Dark Cycle
K
RER AUC
AUC
L
glycerol (mM)
FFA (mM)
M
Serum FFA
Serum triglycerides
Triglyceride (mg/dL)
Time post intralipid injection (hours)

Figure 2.3.3 Acute dietary iron overload does not induce insulin resistance
Six-week old C57BL/6 males were provided control (CID) or 2% carbonyl iron diet (IRD). **(A-B)** Total iron (ferric and ferrous) content in **(A)** tissues and **(B)** serum from mice fed CID or IRD for 6 day. Data shown represents one independent experiment (n=5 mice per group). **(C)** Circulating levels of alkaline phosphatase (ALP) in mice fed CID or IRD for nine days. Data shown represents one independent experiment (n=5 mice per group). **(D-G)** Gene expression in **(D)** liver, **(E)** GWAT, **(F)** IWAT and **(G)** gastrocnemius muscles of mice 6 days post diet initiation. Genes were normalized to expression of housekeeping gene *Rps17* and subsequently normalized to the lowest normalized Gene:Rps17 value within each tissue for each respective gene. Data shown represents one independent experiment (n=5 mice per group). **(H-I)** Insulin tolerance test (ITT) normalized to basal glucose levels and **(I)** corresponding area under the curve (AUC) analysis performed on day 6 post diet initiation. Data shown represents one independent experiment (n= 5 mice per group). **(J)** Diagram for experimental setup to analyze insulin signaling. Following a 6 hour fast on day 6 of the diet time course, mice were i.p. injected with insulin and liver, fat pads, and muscle was harvested 15 minutes post insulin injection to analyze tissue-specific insulin signaling. **(K-N)** Western blot analyses for AKT protein activation in protein extracts from **(K)** GWAT**, (L)** IWAT, **(M)** liver, and **(N)** gastrocnemius muscle from hindlimb. Data shown represents one independent experiment (n= 5 mice per group). Data represent mean ±SEM. **P*<0.05, ****P*<0.001, *****P*<0.0001. Related to **Supplemental Figure 2.3.3, 2.3.4 and 2.3.5.**

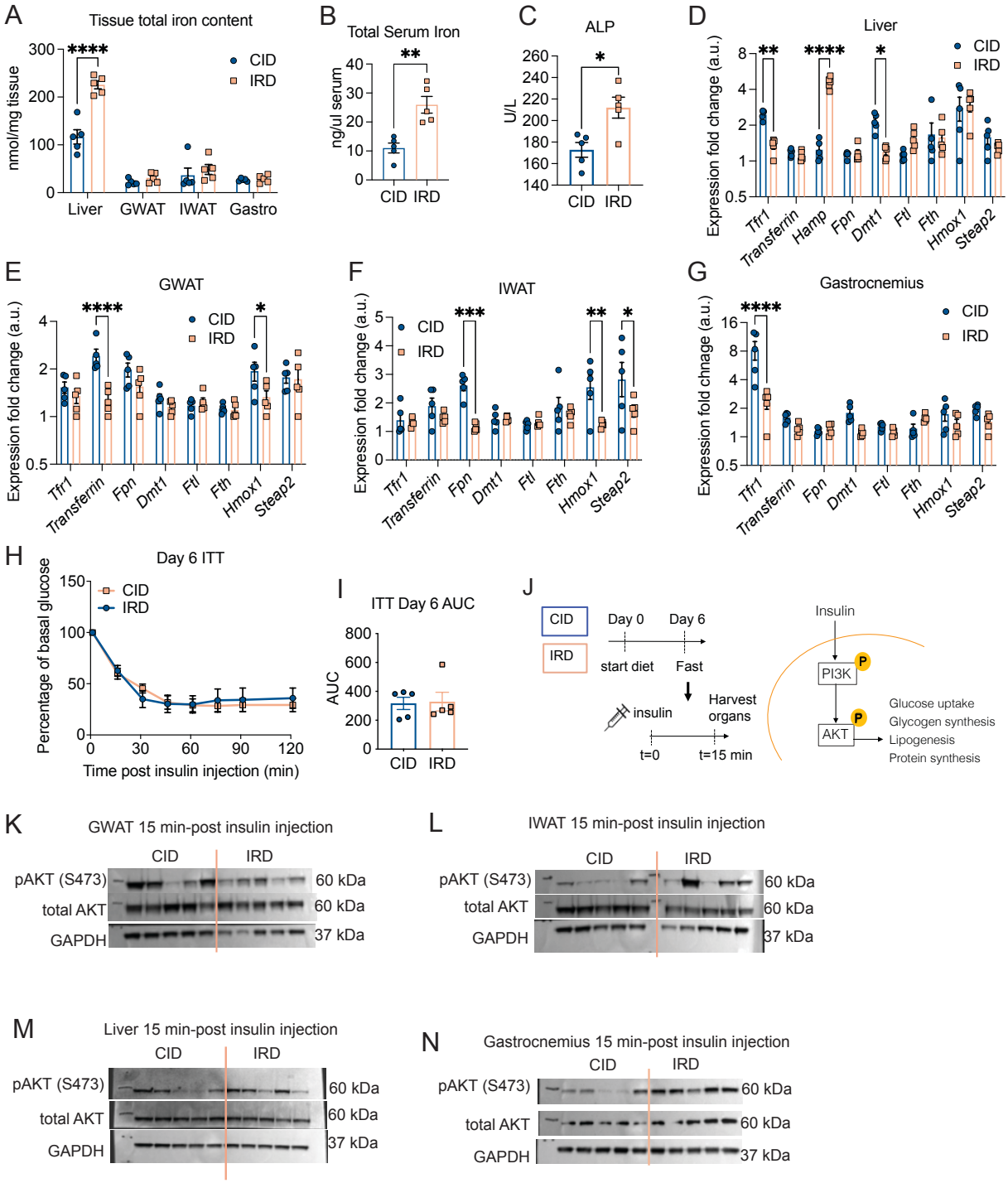
A
Tissue total iron content
nmol/mg tissue
CID
IRD
Liver
GWAT
IWAT
Gastro
B
Total Serum Iron
ng/ul serum
C
ALP
U/L
D
Liver
Expression fold change (a.u.)
Tfr1
Transferrin
Hamp
Fpn
Dmt1
Ftl
Fth
Hmox1
Steap2
E
GWAT
F
IWAT
G
Gastrocnemius
H
Day 6 ITT
Percentage of basal glucose
Time post insulin injection (min)
I
ITT Day 6 AUC
AUC
J
Day 0
Day 6
start diet
Fast
insulin
Harvest organs
t=0
t=15 min
Insulin
PI3K
AKT
Glucose uptake
Glycogen synthesis
Lipogenesis
Protein synthesis
K
GWAT 15 min-post insulin injection
pAKT (S473)
total AKT
GAPDH
60 kDa
37 kDa
L
IWAT 15 min-post insulin injection
M
Liver 15 min-post insulin injection
N
Gastrocnemius 15 min-post insulin injection

Figure 2.3.4 Dietary iron-induced lipid mobilization and adipose tissue wasting is dependent on fat-specific ATGL activity

(A-B) Six-week old C57BL/6 males were given control (CID) or 2% carbonyl iron diet (IRD) for 3 days. Following a six-hour fast, mice were sacrificed and fat pads were harvested for analysis. **(A)** Western blot analysis for activated proteins in canonical lipolysis pathway in **(A)** IWAT and **(B)** GWAT protein extracts**.** (HSL/phospho-HSL Ser563, hormone sensitive lipase; ATGL, Adipose triglyceride lipase; PKA-c, cAMP dependent protein kinase catalytic subunit alpha; GAPDH, Glyceraldehyde3-phosphate dehydrogenase). n=5 mice per condition. **(C-D)** *Pnpla2;Fabp4 cre*+ ($Pnpla2^{WAT\ KO}$) and *Pnpla2;Fabp4 cre*- ($Pnpla2^{WT}$) male littermates between six and eight-weeks old were given 2% carbonyl iron diet (IRD) for 3 days and *ex vivo* lipolysis assays were performed following a 6 hour fast. Glycerol and free fatty acids (FFA) released from **(C)** IWAT **(D)** and GWAT. n=5-7 mice per condition. **(E)** Circulating levels of glycerol and FFA in serum of $Pnpla2^{WAT\ KO}$ and $Pnpla2^{WT}$ littermates fed IRD for 6 days. n=5-7 mice per condition. **(F-H)** Raw mass of fat pads from $Pnpla2^{WAT\ KO}$ and $Pnpla2^{WT}$ littermates fed IRD for five days **(F)** IWAT **(G)** GWAT **(H)** MWAT. For (F) n=8-9 mice per condition and represent two experiments combined. For (G-H) n=4 mice per condition. **(I)** Body fat composition of $Pnpla2^{WAT\ KO}$ and $Pnpla2^{WT}$ littermates fed IRD for 5 days using EchoMRI. Fat mass was normalized to original total body mass. n=4-5 mice per condition. Data represent mean ±SEM; ****P<0.0001. Panels 4A-E, G-I represent one independent experiment and panel 5F represents two pooled experiments. Related to **Supplemental Figure 2.3.6 and 2.3.7**

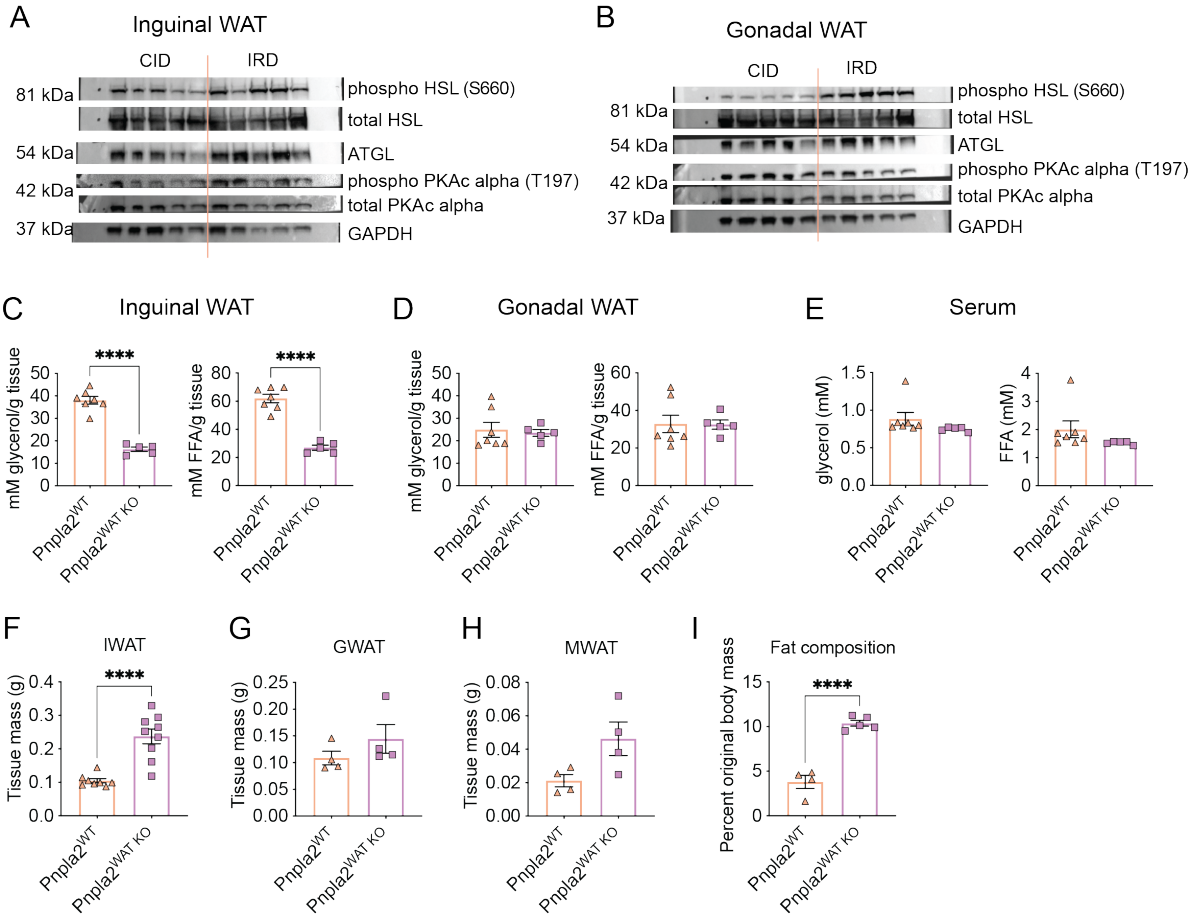
A
Inguinal WAT
CID
IRD
81 kDa
phospho HSL (S660)
total HSL
54 kDa
ATGL
42 kDa
phospho PKAc alpha (T197)
total PKAc alpha
37 kDa
GAPDH
B
Gonadal WAT
CID
IRD
81 kDa
phospho HSL (S660)
total HSL
54 kDa
ATGL
42 kDa
phospho PKAc alpha (T197)
total PKAc alpha
37 kDa
GAPDH
C
Inguinal WAT
mM glycerol/g tissue
mM FFA/g tissue
****
Pnpla2WT
Pnpla2WAT KO
D
Gonadal WAT
mM glycerol/g tissue
mM FFA/g tissue
Pnpla2WT
Pnpla2WAT KO
E
Serum
glycerol (mM)
FFA (mM)
Pnpla2WT
Pnpla2WAT KO
F
IWAT
Tissue mass (g)
****
Pnpla2WT
Pnpla2WAT KO
G
GWAT
Tissue mass (g)
Pnpla2WT
Pnpla2WAT KO
H
MWAT
Tissue mass (g)
Pnpla2WT
Pnpla2WAT KO
I
Fat composition
Percent original body mass
****
Pnpla2WT
Pnpla2WAT KO

Figure 2.3.5 Dietary iron-induced ATGL activity in adipose tissue protects from wasting of lean energy stores

Littermate *Pnpla2;Fabp4 cre*- (Pnpla2^{WT}) and *Pnpla2;Fabp4 cre*+ (Pnpla2$^{WAT\ KO}$) males between six and eight-weeks old were housed in comprehensive laboratory animal monitoring system (CLAMS) metabolic cages for 6 days. Mice were provided 2% carbonyl iron diet (IRD) after brief acclimation period. Daily measurements were taken for body mass and food intake. **(A)** Percent original weight of Pnpla2^{WT} and Pnpla2$^{WAT\ KO}$ mice fed IRD. n=8-9 mice per condition. Data shown represents two pooled independent experiments. **(B)** Daily average food intake of Pnpla2^{WT} and Pnpla2$^{WAT\ KO}$ mice prior to and during IRD feeding period. Data shown represents three pooled independent experiments (n=5-10 mice per group and per timepoint. For some timepoints, food was shredded by some mice and was not weighable for those animals at those timepoints)**. (C)** Average hourly energy expenditure (EEJ) calculated from VO_2 and VCO_2 (ml/hr) using the modified Weir equation and corresponding **(D)** area under the curve analysis for EEJ. Data shown represents one independent experiment (n=4-5 mice per group) **(E)** Principal component analysis of average EEJ from light/dark cycles from Pnpla2^{WT} and Pnpla2$^{WAT\ KO}$ mice fed IRD. Ellipses are indicative of 95% confidence intervals. Data shown represents analysis of one independent experiment (n=4-5 mice per group). **(F)** Daily energy expenditure as a function of daily lean body mass (LBM) over five day period and corresponding **(G)** ANCOVA-predicted EEJ at group average LBM of 14.04 g. Dotted vertical line in regression plot represents group average lean mass (Pnpla2^{WT} linear regression R^2 =.1645, F=3.545, dF= 1, 18, *P*= 0.076, Y=795.3*X+ 30861; Pnpla2$^{WAT\ KO}$ linear regression R^2 =.4920, F=22.28, dF= 1, 23, *P*<0.0001 Y=1041*X+ 28522; pooled slope=949.6) Data shown represents analysis of one independent experiment (n=4-5 mice per group). **(H)** Lean body composition of Pnpla2^{WT} and Pnpla2$^{WAT\ KO}$ mice fed IRD using Echo MRI. Lean mass was normalized to original total body mass. Data shown represents one independent experiment (n=4-5 mice per group). **(I)** Muscle masses from hindlimb of Pnpla2^{WT} and Pnpla2$^{WAT\ KO}$ mice fed IRD for five days (Quadricep; Quad , tibialis anterior; TA, extensor digitorum longus; EDL, soleus, and gastrocnemius; Gastro). Data shown represents one independent experiment (n=4-5 mice per group). **(J)** Gene expression in gastrocnemius of Pnpla2^{WT} and Pnpla2$^{WAT\ KO}$ mice fed IRD for six days. Gene expression is normalized to *Rps17*. Data shown represents one independent experiment (n=4 mice per group). **(K)** Respiratory exchange ratio (RER) and **(L)** Principal component analysis of average RER from light/dark cycles from Pnpla2^{WT} and Pnpla2$^{WAT\ KO}$ mice fed IRD. Ellipses are indicative of 95% confidence intervals. Data shown represents analysis of one independent experiment (n=4-5 mice per group). **(M)** Area under the curve (AUC) analysis of RER for light cycle periods of CLAMS monitoring following introduction of IRD. Data shown represents one independent experiment (n=4-5 mice per group) **(N)** Model of dietary iron regulation of energy balance and ATGL-dependent lipid mobilization. All CLAMS data plotted in zeitgeber time. White/black boxes on X axis represent light/dark cycles of 24-hr day. AUC of CLAMS analyses taken from total average values per mouse. Data represent mean ±SEM; ***P*<0.01, ****P*<0.001**,** *****P*<0.0001. Related to **Supplemental Figure 2.3.8**.

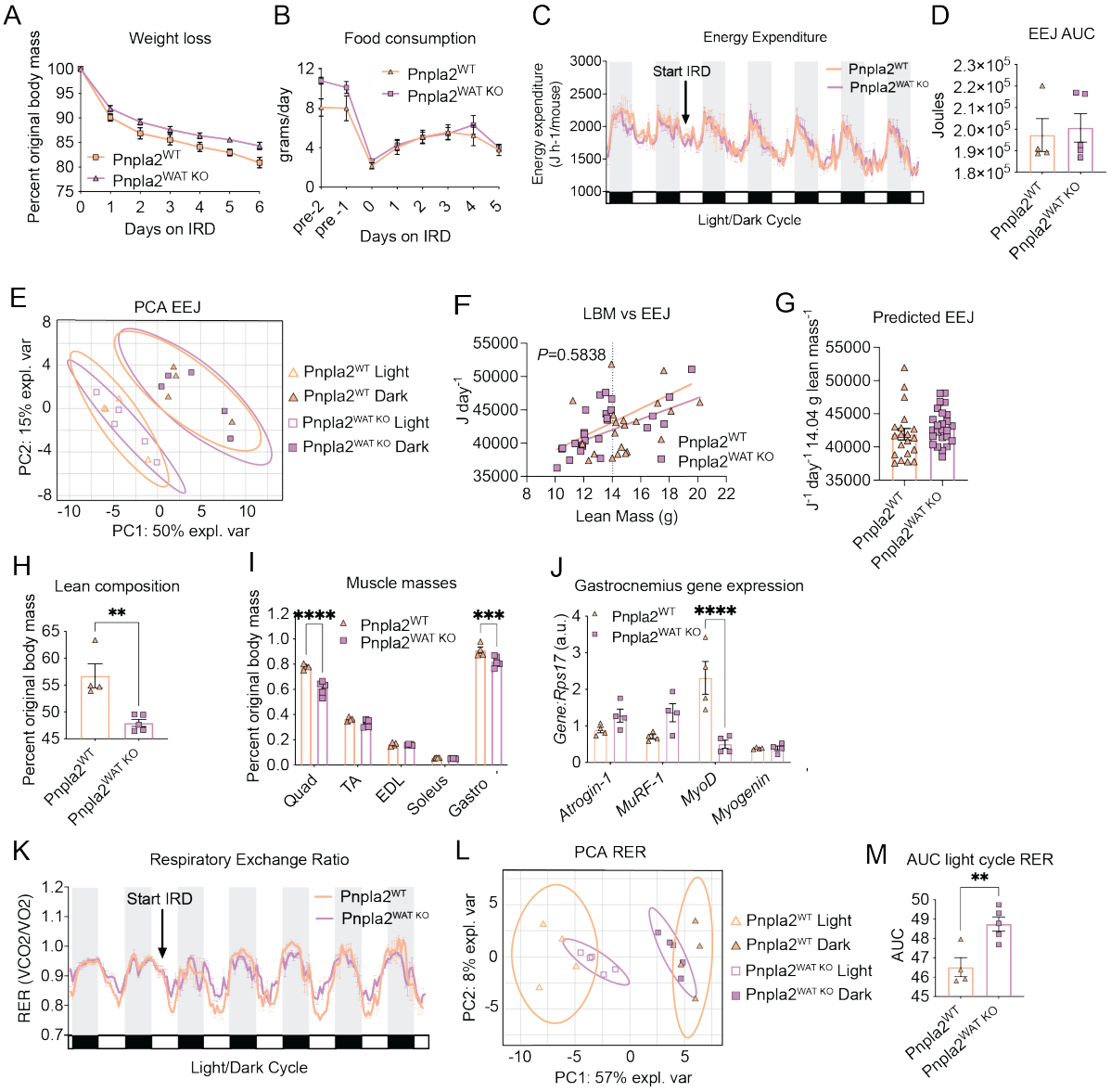
A
Weight loss
Percent original body mass
Pnpla2WT
Pnpla2WAT KO
Days on IRD
B
Food consumption
grams/day
Pnpla2WT
Pnpla2WAT KO
pre-2
pre-1
Days on IRD
C
Energy Expenditure
Energy expenditure (J h-1/mouse)
Start IRD
Pnpla2WT
Pnpla2WAT KO
Light/Dark Cycle
D
EEJ AUC
Joules
Pnpla2WT
Pnpla2WAT KO
E
PCA EEJ
PC2: 15% expl. var
PC1: 50% expl. var
Pnpla2WT Light
Pnpla2WT Dark
Pnpla2WAT KO Light
Pnpla2WAT KO Dark
F
LBM vs EEJ
P=0.5838
J day-1
Lean Mass (g)
Pnpla2WT
Pnpla2WAT KO
G
Predicted EEJ
J-1 day-1 14.04 g lean mass-1
Pnpla2WT
Pnpla2WAT KO
H
Lean composition
Percent original body mass
**
Pnpla2WT
Pnpla2WAT KO
I
Muscle masses
Percent original body mass
****
***
Pnpla2WT
Pnpla2WAT KO
Quad
TA
EDL
Soleus
Gastro
J
Gastrocnemius gene expression
Gene:Rps17 (a.u.)
****
Pnpla2WT
Pnpla2WAT KO
Atrogin-1
MuRF-1
MyoD
Myogenin
K
Respiratory Exchange Ratio
RER (VCO2/VO2)
Start IRD
Pnpla2WT
Pnpla2WAT KO
Light/Dark Cycle
L
PCA RER
PC2: 8% expl. var
PC1: 57% expl. var
Pnpla2WT Light
Pnpla2WT Dark
Pnpla2WAT KO Light
Pnpla2WAT KO Dark
M
AUC light cycle RER
AUC
**
Pnpla2WT
Pnpla2WAT KO
N
Pnpla2WT
Iron
Reduced nutrient absorption
muscle wasting
ATGL dependent lipolysis, lipid mobilization and wasting
Negative energy balance
FFA
Glycerol
Lipid utilization
Pnpla2WAT KO
Iron
Reduced nutrient absorption
muscle wasting
ATGL independent lipolysis
fat wasting
Negative energy balance
muscle derived substrates
Carbohydrate/protein utilization

Supplemental Figure 2.3.1 Iron diet causes negative energy balance
(**A**) Absolute body mass over eight-day diet regimen on CID or IRD. Data shown represents two pooled independent experiments (n=11 mice per group). (**B**) Average hourly absolute gas exchange volumes of O_2 consumed and CO_2 respired for mice fed CID or IRD. Data was used to calculate EEJ in **Figure 2.3.1 B** using modified Weir equation. Data shown represent one independent experiment (n=5-6 mice per group)**.** (**C**) Daily energy expenditure as a function of daily total body mass (TBM) over eight day period (CID linear regression, R^2=.1523, F=8.266, dF=1, 46, *P*=0.0061, Y = 455.0*X + 29062; IRD linear regression, R^2=.6545, F=71.98, dF=1, 38 , *P*<0.0001, Y = 1379*X + 6417). Data shown represent analyses of one independent experiment (n=5-6 mice per group). (**D**) Average hourly activity levels plotted as total X directional beam breaks per hour for mice fed CID or IRD in CLAMS and corresponding area under the curve analysis (AUC) for total activity in CLAMS. Data shown represents one independent experiment (n= 6 mice per group) (**E**) Principle component analysis for activity of CID and IRD fed mice in light/dark cycles. Ellipses are indicative of 95% confidence intervals. Data shown represents analyses of one independent experiment (n= 6 mice per group). (**F**) Daily core temperature of CID or IRD fed mice. Data represent two pooled independent experiments (n=5-11 mice per timepoint per group). (**G-L**) C57BL/6 male mice were fed CID *ad libitum* (*ad lib)*, IRD *ad libitum* (*ad lib)*, or CID pair fed matched to average historical IRD food consumption values. (**G**) Absolute body mass over eight-day diet regimens. Data shown represents two pooled independent experiments (n=9 mice per group). Blue asterisks denote comparisons between CID *ad lib* and CID pair fed. Gray asterisks denote comparisons between CID pair fed and IRD *ad lib*. Peach asterisks denote comparisons between CID *ad lib* and IRD *ad lib*. (**H**) Daily core temperature of mice fed CID *ad lib,* pair fed, or IRD *ad lib*. Data represent two pooled independent experiments (n=4-9 mice per timepoint per group). Gray asterisk denotes comparison between CID *ad lib* and CID pair fed. Peach asterisks denote comparisons between CID *ad lib* and IRD *ad lib*. (**I**) Average hourly activity levels plotted as total X directional beam breaks per hour for mice on dietary regimens in CLAMS and corresponding area under the curve analysis (AUC) for total activity in CLAMS. Data shown represents one independent experiment (n= 4 mice per group). (**J**) Principle component analysis for activity mice from three dietary regimens in light/dark cycles. Ellipses are indicative of 95% confidence intervals. Data shown represents analyses of one independent experiment (n= 4 mice per group). (**K**) Average hourly absolute gas exchange volumes of O_2 consumed and CO_2 respired for mice fed CID *ad lib,* pair fed, or IRD *ad lib*. Data was used to calculate EEJ in **Figure 2.3.1 H** using modified Weir equation. Data shown represent one independent experiment (n=4 mice per group). (**L**) Daily energy expenditure as a function of total body mass (TBM) over eight day period (CID *ad lib* linear regression, R^2=.3360, F=17.2, df= 1, 34, *P*=0.0002, Y = 565.9*X + 35548; CID pair fed linear regression, R^2=.1905, F=8.002, dF=1, 34 , *P*=0.0078, Y = 590.3*X + 32039; IRD *ad lib* linear regression, R^2=.8254, F=160.7, dF=1, 34 , *P*<0.0001, Y = 3300*X - 26401). Data shown represent analyses of one independent experiment (n=4 mice per group). (**M**) Net calorie absorption of mice fed CID and IRD. Data shown represents two time points per diet (Days 4 and 6 post diet initiation). Each data point represents the total caloric intake pooled from two cages of mice minus the total caloric content of solid fecal excrement pooled from the same two cages per respective day of dietary regimen (5 mice per cage, 10 mice pooled). All CLAMS data plotted in zeitgeber time. Data represent mean ±SEM; CID **P*<0.05, ***P*<0.01, ****P*<0.001, *****P*<0.0001. Related to **Figure 2.3.1**

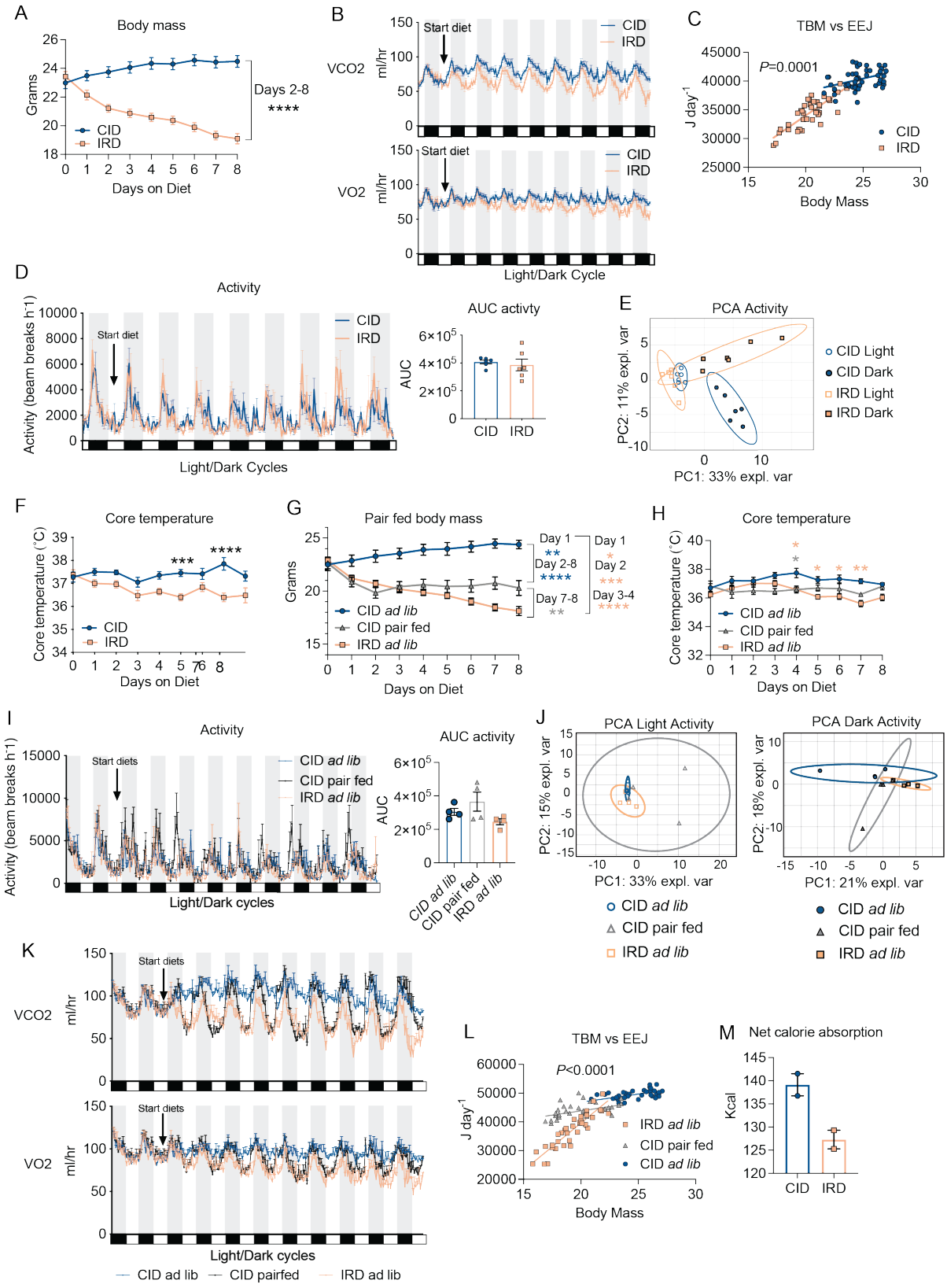
A
Body mass
Grams
Days on Diet
CID
IRD
Days 2-8
****
B
Start diet
VCO2
VO2
ml/hr
CID
IRD
Light/Dark Cycle
C
TBM vs EEJ
P=0.0001
J day-1
Body Mass
D
Activity
Activity (beam breaks h-1)
Light/Dark Cycles
AUC activty
AUC
E
PCA Activity
PC2: 11% expl. var
PC1: 33% expl. var
CID Light
CID Dark
IRD Light
IRD Dark
F
Core temperature
Core temperature (˚C)
Days on Diet
G
Pair fed body mass
Grams
CID ad lib
CID pair fed
IRD ad lib
Day 1
Day 2-8
Day 7-8
Day 2
Day 3-4
H
Core temperature
I
Activity
Start diets
Light/Dark cycles
AUC activity
J
PCA Light Activity
PCA Dark Activity
PC2: 15% expl. var
PC1: 33% expl. var
PC2: 18% expl. var
PC1: 21% expl. var
K
CID ad lib
CID pairfed
IRD ad lib
L
TBM vs EEJ
P<0.0001
M
Net calorie absorption
Kcal

Supplemental Figure 2.3.2 Iron causes negative energy balance independent of reduced food intake

C57BL/6 male mice were fed CID *ad libitum* (*ad lib)*, IRD *ad libitum* (*ad lib)*, or CID pair fed matched to average historical iron food consumption values. **(A)** Absolute heart mass and corresponding **(B)** heart mass normalized to total body mass of mice from day eight of pair feeding dietary regimens. Data shown represents 3 pooled independent experiments (n=10-16 mice per group). **(C)** Body composition analyses on day eight of pair fed dietary regimens using Echo MRI. Fat and lean mass were normalized to original body mass. Data shown represents one independent experiment (n=5 mice per group). **(D)** IWAT fat pad mass on day eight of pair feeding dietary regimens normalized to original body mass. Data shown represents one independent experiment (n=5 mice per group). **(E)** Muscle masses on day eight of pair fed dietary regimens normalized to original body mass. Data shown represents one independent experiment (n=4-5 mice per group). (Quadricep; Quad , tibialis anterior; TA, extensor digitorum longus; EDL, soleus, and gastrocnemius; Gastro)**. (F)** Gene expression in gastrocnemius on day eight of pair fed dietary regimens. Gene expression was normalized to housekeeping expression of *Rps17*. Data shown represents one independent experiment (n=4-5 mice per group). (**G-I**) Mice were housed in the CLAMS to determine the respiratory exchange ratio. (**G**) Average hourly respiratory exchange ratio (RER) calculated as ratio of ml CO_2 OUT (respired):ml O_2 IN (inhaled) and corresponding (**H**) Area under the curve (AUC) analysis for RER for period of matched food consumption. Data shown represents one independent experiment (n=4 mice per group). (**I**) Principal component analysis for the respiratory exchange ratio (RER) of mice in light/dark cycles form the three dietary regimens. Ellipses are indicative of 95% confidence intervals. Data shown represents analyses of one independent experiment (n=4 mice per group). Data represent mean ±SEM; **P*<0.05, ***P*<0.01, ****P*<0.001, *****P*<0.0001. Related to **Figure 2.3.2.**

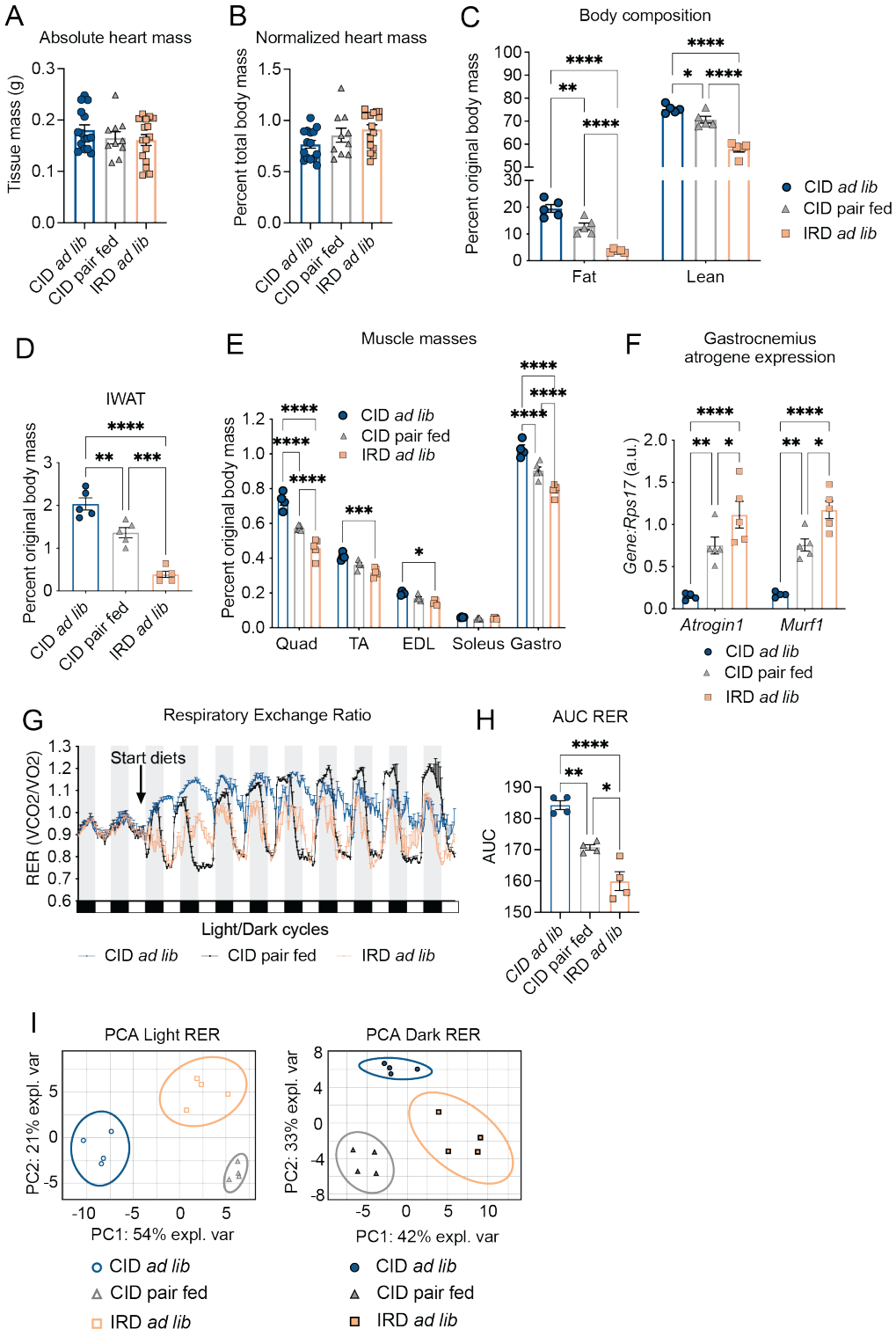
A
Absolute heart mass
Tissue mass (g)
CID ad lib
CID pair fed
IRD ad lib
B
Normalized heart mass
Percent total body mass
C
Body composition
Percent original body mass
Fat
Lean
D
IWAT
E
Muscle masses
Quad
TA
EDL
Soleus
Gastro
F
Gastrocnemius atrogene expression
Gene:Rps17 (a.u.)
Atrogin1
Murf1
G
Respiratory Exchange Ratio
Start diets
RER (VCO2/VO2)
Light/Dark cycles
H
AUC RER
AUC
I
PCA Light RER
PC2: 21% expl. var
PC1: 54% expl. var
PCA Dark RER
PC2: 33% expl. var
PC1: 42% expl. var

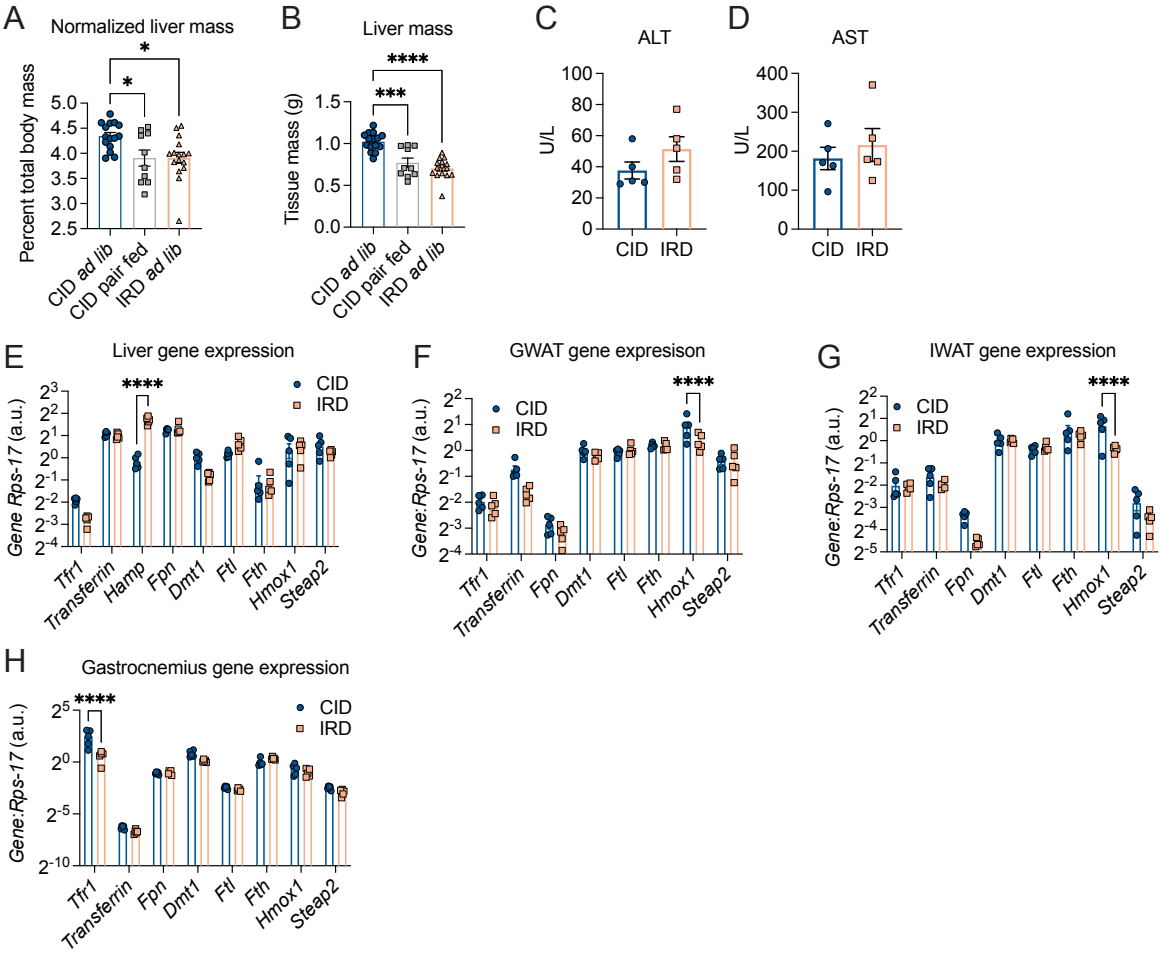

Supplemental Figure 2.3.3 Tissue responses to dietary iron supplementation
Six-week old C57BL/6 males were provided control (CID) or 2% carbonyl iron diet (IRD). **(A)** Liver masses from mice fed CID *ad libitum*, CID pair fed, and IRD *ad libitum* for 8 days normalized to respective body mass on day 8 and **(B)** unnormalized raw liver masses**.** Data shown represents three pooled independent experiments (n=10-16 mice per group). **(C)** Circulating levels of alanine amino transferase (ALT) and **(D)** aspartate aminotransferase (AST) in mice fed CID or IRD for nine days. Data shown represents one independent experiment (n=5 mice per group). (**E-H**) Gene expression in (**E**) liver, (**F**) GWAT, (**G**) IWAT, and (**H**) gastrocnemius muscles of mice fed CID or IRD for 6 days. Expression was normalized to *Rps17* expression. Data shown represents one independent experiment (n=5 mice per group). Data represent mean ±SEM. **P*<0.05, ****P*<0.001, *****P*<0.0001. Related to **Figure 2.3.3**

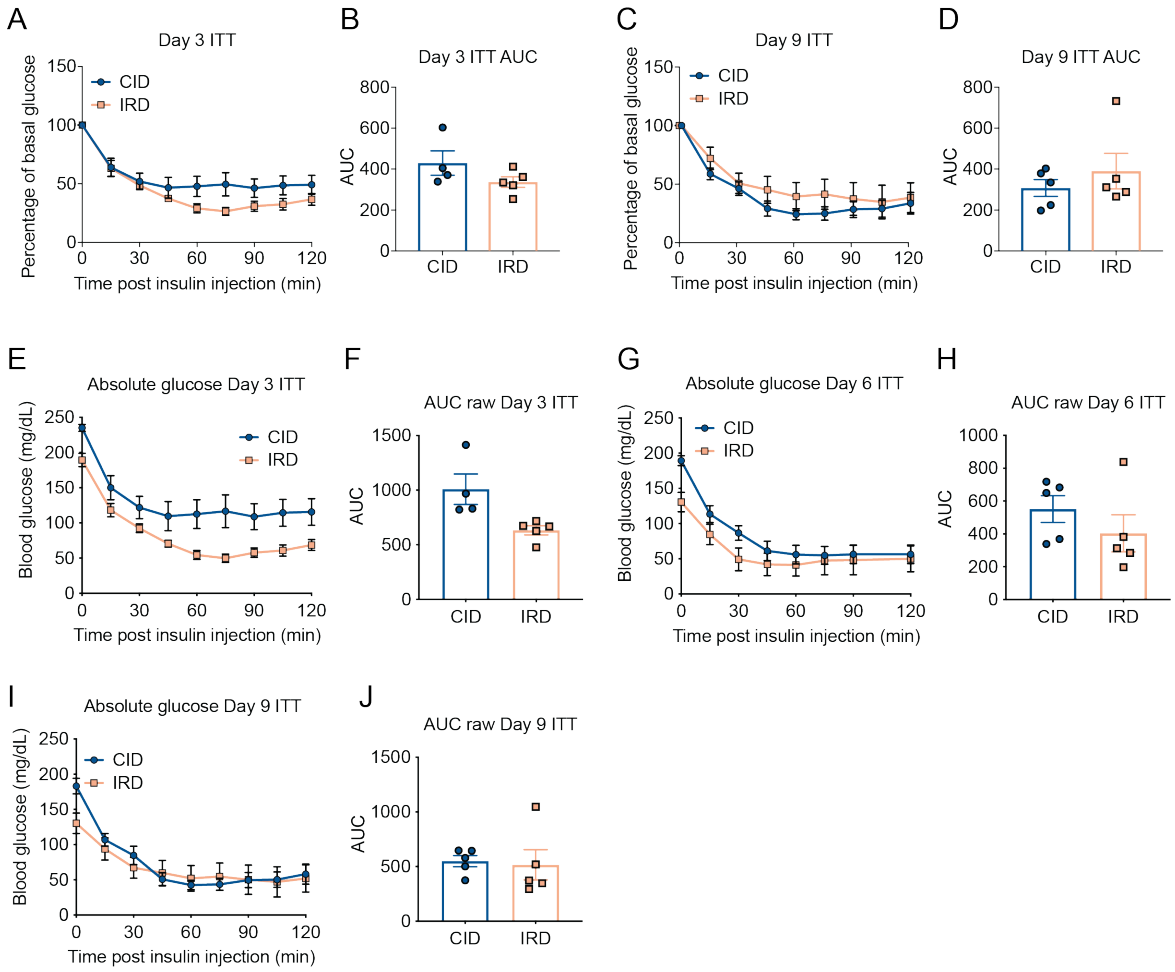

Supplemental Figure 2.3.4 Insulin sensitivity not affected by dietary iron supplementation

Six-week old C57BL/6 males were provided control (CID) or 2% carbonyl iron diet (IRD) for a nine-day time course and insulin tolerance tests (ITT) were performed on day 3, 6, and 9 of time course following a 6-hour fast. **(A-D)** ITT curve normalized to basal glucose levels and corresponding area under the curve (AUC) analysis performed on **(A, B)** day 3 and **(C, D)** day 9 post diet initiation. **(E-J)** Absolute glucose levels and corresponding AUC analyses for ITT performed on **(E, F)** day 3, **(G, H)** day 6 and **(I, J)** day 9 post diet initiation. All data shown represents one independent experiment (n=5 mice per group). Data represent mean ±SEM. Related to **Figure 2.3.3**

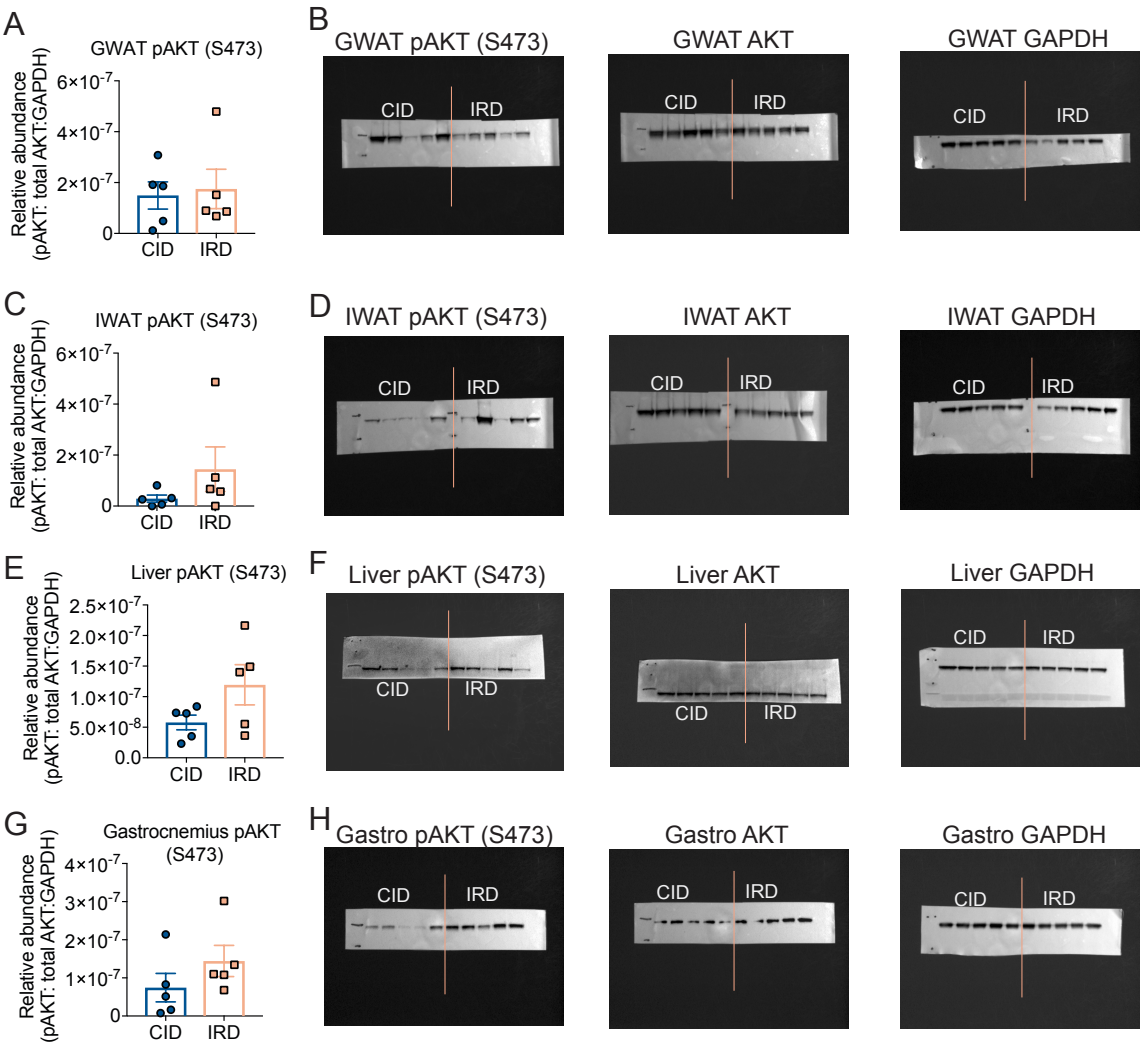

Supplemental Figure 2.3.5 Iron does not influence tissue-level insulin sensitivity
Six-week old C57BL/6 males were provided control (CID) or 2% carbonyl iron diet (IRD) for a nine-day time course and experiments were performed on day 3, 6, and 9 of time course following a 6-hour fast. Mice were injected with insulin and tissues were harvested 15 minutes post injection and snap frozen for analysis. **(A)** Densitometry analyses and **(B)** original blots for AKT activation in GWAT from **Figure 3K**. **(C)** Densitometry analyses and **(D)** original blots for AKT activation in IWAT from **Figure 3L**. **(E)** Densitometry analyses and **(F)** original blots for AKT activation in liver from **Figure 3M**. **(G)** Densitometry analyses and **(H)** original blots for AKT activation in gastrocnemius from **Figure 3N**. All data shown represents one independent experiment. Data represent mean ±SEM; CID n=5, IRD n=5. Related to **Figure 2.3.3**

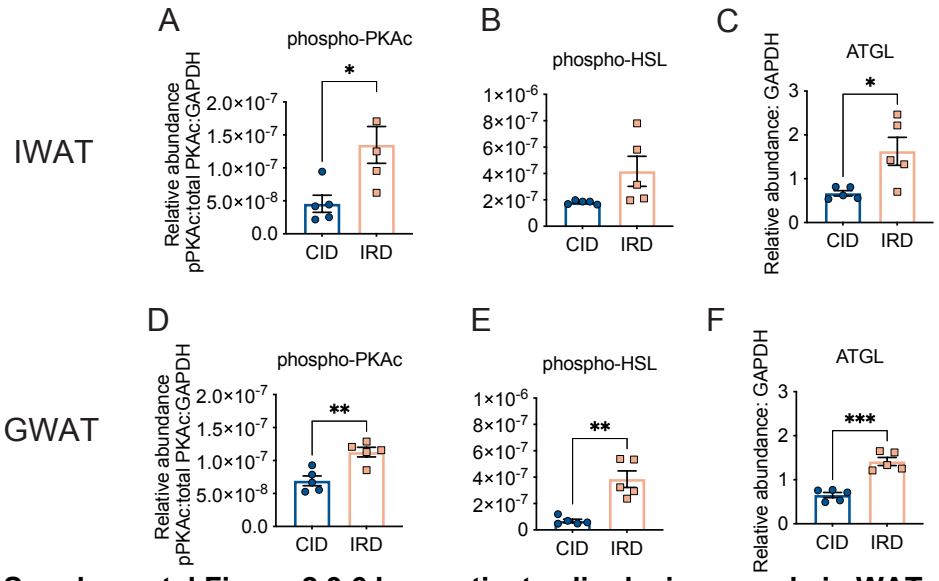

Supplemental Figure 2.3.6 Iron activates lipolysis cascade in WAT

Six-week old C57BL/6 males were provided control (CID) or 2% carbonyl iron diet (IRD) for a nine-day time course and experiments were performed on day 3, 6, and 9 of time course following a 6-hour fast. Mice were injected with insulin and tissues were harvested 15 minutes post injection and snap frozen for analysis. **(A)** Densitometry analyses and **(B)** original blots for AKT activation in GWAT from **Figure 2.3.3 K**. **(C)** Densitometry analyses and **(D)** original blots for AKT activation in IWAT from **Figure 2.3.3 L**. **(E)** Densitometry analyses and **(F)** original blots for AKT activation in liver from **Figure 2.3.3 M**. **(G)** Densitometry analyses and **(H)** original blots for AKT activation in gastrocnemius from **Figure 2.3.3 N**. All data shown represents one independent experiment. Data represent mean ±SEM; CID n=5, IRD n=5. Related to **Figure 2.3.3**

Supplemental Figure 2.3.7 Iron activates lipolysis cascade in WAT (continued)
(A-F) Uncropped Western blot imaging for **Figure 2.3.4 A** protein extracts from IWAT. (HSL/phospho-HSL Ser563, hormone sensitive lipase; ATGL, Adipose triglyceride lipase; PKA-c, cAMP dependent protein kinase catalytic subunit alpha; GAPDH, Glyceraldehyde3-phosphate dehydrogenase). Data shown represents one independent experiment (n= 5 mice per group)**. (G-L)** Uncropped Western blot imaging for **Figure 2.3.4 B** protein extracts from GWAT. (HSL/phospho-HSL Ser563, hormone sensitive lipase; ATGL, Adipose triglyceride lipase; PKA-c, cAMP dependent protein kinase catalytic subunit alpha; GAPDH, Glyceraldehyde3-phosphate dehydrogenase). Data shown represents one independent experiment (n= 5 mice per group). Related to **Figure 2.3.4**

A

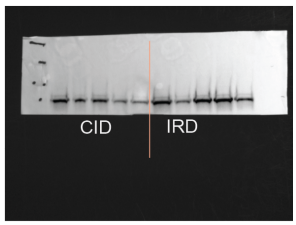

IWAT phospho-HSL (S660)

G

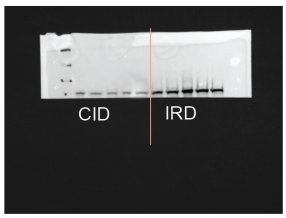

GWAT phospho-HSL (S660)

B

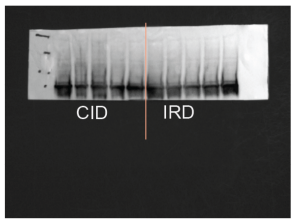

IWAT HSL

H

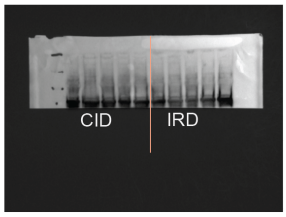

GWAT HSL

C

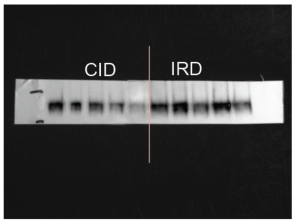

IWAT ATGL

I

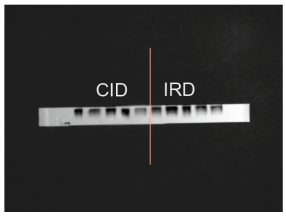

GWAT ATGL

D

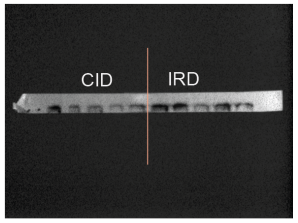

IWAT phospho-PKAc alpha (T197)

J

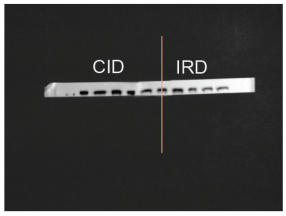

GWAT phospho-PKAc alpha (T197)

E

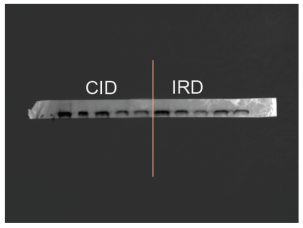

IWAT PKAc alpha

K

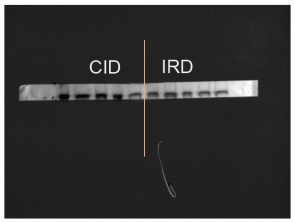

GWAT PKAc alpha

F

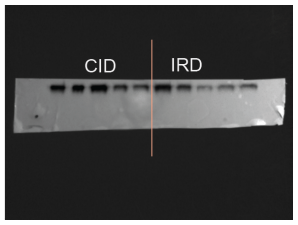

IWAT GAPDH

L

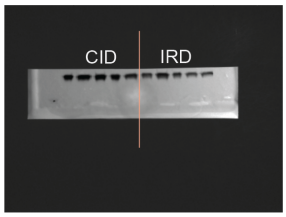

GWAT GAPDH

Supplemental Figure 2.3.8 Adipose-specific ATGL does not affect net energy balance in response to iron rich diet

Littermate *Pnpla2;Fabp4 cre*- (Pnpla2^{WT}) and *Pnpla2;Fabp4 cre*+ (Pnpla2$^{WAT\ KO}$) males between six and eight-weeks old were housed in comprehensive laboratory animal monitoring system (CLAMS) metabolic cages for 6 days. Mice were provided 2% carbonyl iron diet (IRD) after brief acclimation period. Daily measurements were taken for body mass, core temperature and food intake. **(A)** Absolute body mass of Pnpla2^{WT} and Pnpla2$^{WAT\ KO}$ mice fed IRD. Data shown represents two pooled independent experiments (n=8-9 mice per group). **(B)** Average hourly absolute gas exchange volumes of O_2 consumed and CO_2 respired for Pnpla2^{WT} and Pnpla2$^{WAT\ KO}$ mice fed IRD. Data was used to calculate EEJ in **Figure 2.3.5 C** using modified Weir equation. Data shown represents one independent experiment (n=4-5 mice per group)**. (C)** Energy expenditure as a function of total body mass (TBM) over five day period and corresponding **(D)** ANCOVA-predicted EEJ at group average TBM of 21.3 g. Dotted vertical line in regression plot represents group average lean mass (Pnpla2^{WT} linear regression R^2 =.2294, F=6.550, dF= 1, 22, *P*=0.0179, Y=1311*X+ 14248; Pnpla2$^{WAT\ KO}$ linear regression R^2 =.7201, F=72.05, dF= 1, 28, *P*<0.0001, Y=1903*X+ 1059; pooled slope=1659) Data shown represents analysis of one independent experiment (n=4-5 mice per group). (**E**) Daily core temperature of Pnpla2^{WT} and Pnpla2$^{WAT\ KO}$ mice. Data represents two pooled independent experiments (n=10-11 mice per group). (**F**) Average hourly activity levels plotted as total X directional beam breaks per hour for Pnpla2^{WT} and Pnpla2$^{WAT\ KO}$ mice fed IRD and corresponding **(G)** Area under the curve (AUC) analysis. Data shown represents one independent experiment (n=4-5 mice per group)**.** (**H**) Principle component analysis for activity of IRD-fed Pnpla2^{WT} and Pnpla2$^{WAT\ KO}$ mice in light/dark cycles. Ellipses are indicative of 95% confidence intervals. Data shown represents analysis of one independent experiment (n=4-5 mice per group). (**I**) Body composition analyses of Pnpla2^{WT} and Pnpla2$^{WAT\ KO}$ mice fed control chow prior to IRD supplementation. Fat and lean mass is normalized to total body mass. Data shown represents one independent experiment (n=4-5 mice per group). Data represent mean ±SEM. Related to **Figure 2.3.5**

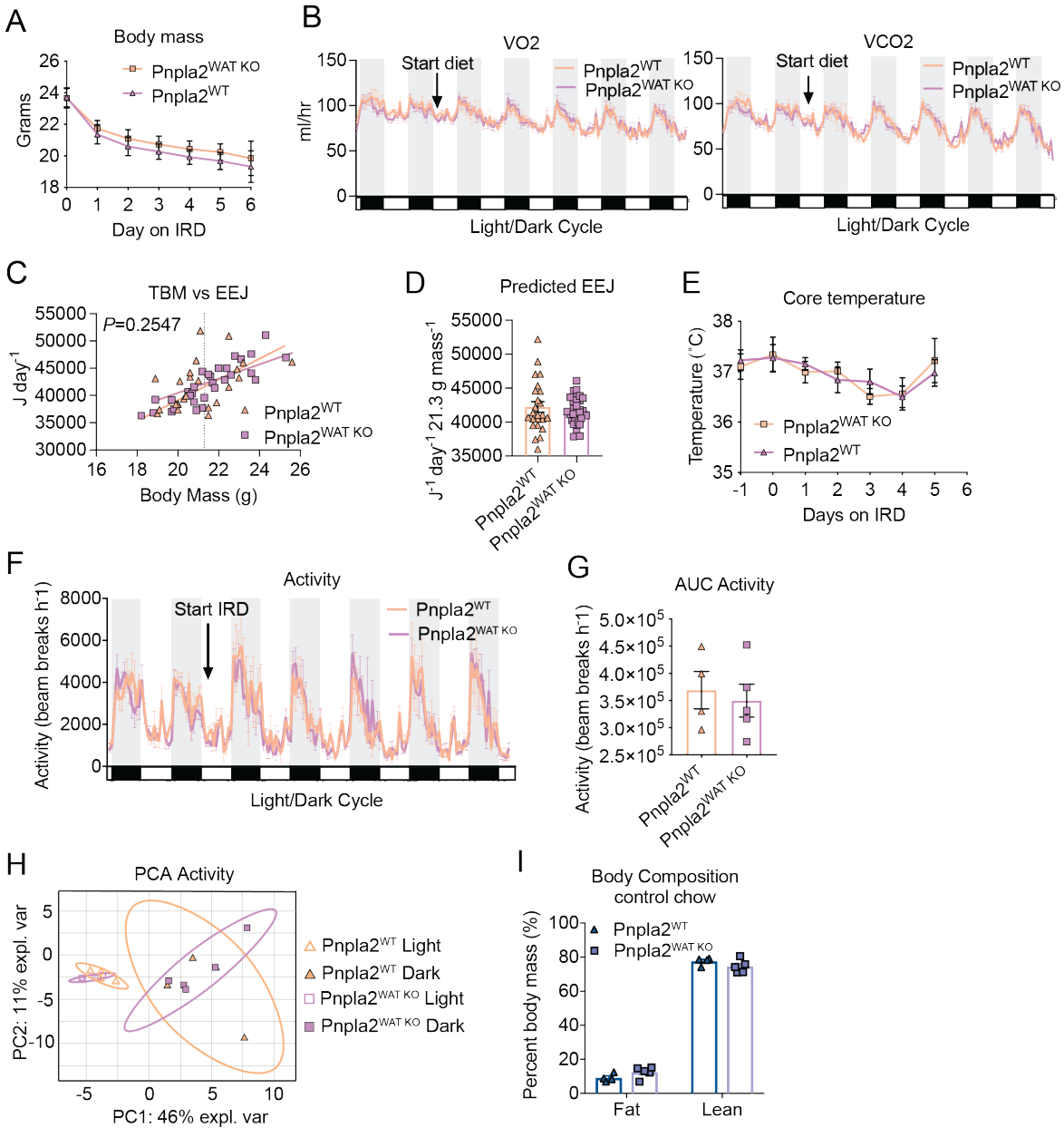
A
Body mass
Pnpla2WAT KO
Pnpla2WT
Grams
Day on IRD
B
VO2
Start diet
Pnpla2WT
Pnpla2WAT KO
ml/hr
Light/Dark Cycle
VCO2
Start diet
Pnpla2WT
Pnpla2WAT KO
Light/Dark Cycle
C
TBM vs EEJ
P=0.2547
J day-1
Pnpla2WT
Pnpla2WAT KO
Body Mass (g)
D
Predicted EEJ
J-1 day-1 21.3 g mass-1
Pnpla2WT
Pnpla2WAT KO
E
Core temperature
Temperature (˚C)
Pnpla2WAT KO
Pnpla2WT
Days on IRD
F
Activity
Start IRD
Pnpla2WT
Pnpla2WAT KO
Activity (beam breaks h-1)
Light/Dark Cycle
G
AUC Activity
Activity (beam breaks h-1)
Pnpla2WT
Pnpla2WAT KO
H
PCA Activity
PC2: 11% expl. var
PC1: 46% expl. var
Pnpla2WT Light
Pnpla2WT Dark
Pnpla2WAT KO Light
Pnpla2WAT KO Dark
I
Body Composition
control chow
Percent body mass (%)
Pnpla2WT
Pnpla2WAT KO
Fat
Lean

Chapter 3: Iron-induced metabolic rearrangements uncouple hallmarks of infectious colitis

3.1 Introduction

Iron is an essential micronutrient for nearly all living organisms and is a scarce and crucial resource for pathogens in the host environment. Hosts have evolved numerous strategies to limit pathogens' access to iron during infection that are collectively recognized as nutritional immunity. In instances of inflammation, infection or iron overload, hosts limit iron absorption in the gut, sequester iron intracellularly in host tissues, and decrease circulating availability of iron—strategies that aim to blunt pathogen proliferation and inhibit virulence [1–3]. Notably, mounting the iron sequestration response can dramatically alter host health and physiology on an organismal scale. The breadth of this response was first observed by physicians in the 1940's who reported that chronic infections were associated with anemia that could not be rescued by iron supplementation. It has become well appreciated in recent decades that iron overload and sequestration in host tissues can cause substantial physiological stress, including liver damage, immune and metabolic dysfunction, adipose tissue inflammation, and dysbiosis of the gut microbiome [4–8] The physiological effects of iron described here are likely the tip of the iceberg as host age, gender, genetics and environmental factors largely influence the severity and outcomes of iron overload.

While nutritional immunity describes hosts' strategy to limit pathogenicity during infection through iron withholding, it does not address how iron status affects host physiology and how these changes can independently influence pathogenicity. Our group recently reported that iron promotes health and survival in a lethal model of transmissible murine colitis through modulating insulin sensitivity- demonstrating that host iron metabolism can independently affect pathogenicity beyond the principle of nutritional immunity.

In the current study, we aimed to expand on the principle of nutritional immunity to demonstrate that iron-induced physiological effects can independently affect pathogenicity and disease in a non-lethal model of transmissible murine colitis. Here, we show that mice challenged with *Citrobacter rodentium* exhibit *increased* resistance defenses and protection from *C. rodentium*-induced mucosal pathology when fed an iron rich diet. Though dietary iron decreases the severity of colitis, mice fed an iron rich diet exhibit increased weight loss, fat wasting and lipolysis. We show that while fat wasting is dispensable for promoting resistance and protection from mucosal pathology, it is necessary to prevent *C. rodentium*-induced colon shortening and remodeling. This infection model demonstrates the need to expand on the principle of nutritional immunity to include the host's response to a dietary iron surplus and re-examine the etiology of infectious colitis. Our work has uncovered a novel iron-dependent adipose tissue-gut axis that decouples traditional hallmarks of infectious colitis into inflammatory and non-inflammatory stages.

3.2 Material and Methods

Mice. Six week-old male C57BL/6 mice were purchased from Jackson Laboratories and housed in our facility to acclimate for 2 days prior to experimentation. To study ATGL-dependent lipolysis, we performed crosses with *B6N.129S-Pnpla2tm1Eek/J* mice to *B6.Cg-Tg(Fabp4-cre)1Rev/J* both from Jackson labs to generate *Pnpla2;Fabp4 cre*+ and *Pnpla2;Fabp4 cre*- mice. For experiments, 6-8 week old male littermates were used. All animal experiments were done in accordance with The Salk Institute Animal Care and Use Committee and performed in our AALAC-certified vivarium.

Mouse diets. Mice were fed a 2% carbonyl iron supplemented diet or a control diet from Envigo. For infection experiments, diets were supplied on day 0. Daily food consumption was determined by measuring mass of food pellets daily from single-housed mice.

Bacteria and inoculum preparation. *Citrobacter rodentium* DBS100 was purchased from ATCC. To prepare inoculum, *C. rodentium* was grown overnight on sterile MacConkey agar plates at 37˚C and single colonies were used to inoculate sterile Luria-Bertani (LB) media and shook overnight at 37 ˚C and 225 rpm. The following morning, OD_{600} was measured to calculate the resuspension volume of sterile PBS to achieve a inoculum dose of ~$5x10^9$ CFU/ml determined from a growth curve. 20 ml of culture were pelleted by centrifugation and growth medium was decanted. Inoculum was immediately used for infection and a portion of inoculum was reserved for determining the infection dose. Inoculum was serially diluted and plated on sterile MacConkey agar to confirm CFU concentration for each experiment.

Mouse infection models. Animals were gavaged with 100 µl of *C. rodentium* inoculum prepared as described above to achieve a dose of ~$5x10^8$ CFU. Diets were supplied *ad libitum* on the same day as infection. For each infection, the inoculum was serially diluted and plated on sterile MacConkey plates to determine the infection dose. Inoculum dose for each set of experiments is noted in figure legends.

Quantification of *C. rodentium* in tissues or stool. Mouse tissue masses were measured prior to homogenizing in 1 ml of PBS containing 1% TritonX-100 in a bead beater with a ceramic bead for 2 min using Bead Mill 24 (Fischer Scintific). Fresh fecal pellet masses were measured prior to homogenizing with 1 ml PBS using a syringe plunger and allowed to settle for 5 minutes. Colony forming units (CFU) were quantified by plating serially diluted homogenized samples on MacConkey agar: *C.r.* pathogen loads from homogenized tissues was determined by normalizing CFU to tissue mass. *C.r.* fecal shedding determined by normalizing CFU to pellet mass.

Body composition measurements. Total body fat and lean mass were measured using an EchoMRI machine. Total fat or total lean mass(g) was normalized to total body mass(g) to determine the percent body composition of fat and lean tissues. Fat pad masses were measured by dissecting and weighing subcutaneous fat pads (inguinal WAT), visceral fat pads (gonadal WAT), and mesenteric WAT post mortem. Muscles from hindlimb were dissected and weighed postmortem. The following muscles were harvested to represent muscles of varied myofiber composition: Quadricep (primarily fast twitch), Tibialis anterior (fast/slow twitch), extensor digitorum longus (fast/slow twitch), Soleus (slow twitch), gastrocnemius (fast/slow twitch).

Histology. Colons were dissected and carefully removed from sacrificed animals. Before tissue preparation for histology, colon length was measured. Fecal content was not removed. Colons were inflated with 10% Formalin for 1-2 minutes. Following the brief fixation period, colon was arranged in a spiral pattern (swiss roll) with rectal end in center and cecal end on the outside of a counter-clockwise roll on top of a paper square. Colons were then transferred to formalin soaked sponges in cassettes. Cassettes were placed in 10% Formalin for 24-48 hours before transferring into 70% ethanol for storage prior to paraffin embedding and tissue sectioning. Colon slides were prepared in 4 μm sections and stained by H&E.

Metabolic phenotyping of global substrate utilization. *C. rodentium*-infected mice were fed control or 2 % carbonyl iron diets were singly housed in metabolic cages from the Columbus Instruments Comprehensive Lab Animal Monitoring System (CLAMS) where O_2 consumption, CO_2 production, and activity data was collected. Food consumption was measured by weighing food pellets daily. Mice were removed from metabolic cages daily to measure body mass with a scale and body composition using EchoMRI. Respiratory Exchange Ratio (RER) was determined by dividing VCO_2/VO_2.

Insulin tolerance tests. *C. rodentium*-infected mice were fed control or 2 % carbonyl iron diets for a period of 3, 6 or 9 days and fasted in fresh cages for 6 hours with *ad libitum* access to water. Blood glucose measurements were taken using a Nova Max plus by making small cuts to the tips of tails using a sterile razor blade and gently squeezing the tail from base to tip. Insulin was administered according to body mass (1U/kg) in a single

intraperitoneal injection at time=0 minutes. Blood glucose measurements were taken every 15 minutes for a period of 120 minutes. Blood glucose measurements were normalized to their time=0 fasted blood glucose levels to generate a curve representing the percent drop in glucose levels from t=0 blood glucose levels. Area under the curve analyses were performed for each mouse in Prism.

Gene expression analyses. Tissues were flash frozen in liquid nitrogen immediately following harvest from sacrificed animals. Tissues were ground into a powder using ceramic mortar and pestles equilibrated in liquid nitrogen. Powder was added to Trizol reagent and homogenized with a ceramic bead in a bead beater. Chloroform was added to homogenate and centrifuged to separate the organic and aqueous layers. Aqueous layer was carefully transferred to fresh nuclease-free tubes where isopropanol was added and mixture was left to precipitate at -20˚C for at least 1 hour. Isopropanol/aqueous layer solution was added to a Qiagen RNeasy column and RNeasy protocol was followed from this step, including the removal of genomic DNA using Qiagen's on-column DNase kit. RNA was eluted in nuclease-free h2o and quantified using a Nanodrop Spectrophotometer. cDNA was synthesized using SuperScript IV using ~200 ng RNA and oligo dT for mammalian cDNA and random hexamers for bacterial cDNA. Real time quantitative PCR was performed using SYBR green Mix on QuantStudio 5 from Applied Biosystems. Relative standard curve method was used to analyze gene expression relative to a dilution series of pooled samples. *Rps17* was used as an endogenous housekeeping control for relative normalization.

Primer table

Gene target	Forward 5'->3'	Reverse 5'->3'
map	AGCGGTTGAAAGCGTGATAC	CTTTACCGCACTGCTCATCA
tir	CTTCAGGAATGGGAGATGGA	CAACCGCCTGAACAATACCT
espA	AGTGATCTTGCGGCTGAGTT	ATCCACCGTCGTTGTCAAAT
espI	AGATGAAGGCCTGCTCTCAG	ATATGCCTGGAACGGAACTG
Il22	TCAACCGCACCTTTATGCTG	TGAGTTTGGTCAGGAAAGGC
Il17	AAGGCAGCAGCGATCATCC	GGAACGGTTGAGGTAGTCTGAG
Lipocalin-2	AATGTCACCTCCATCCTGGTCA	GCGAACTGGTTGTAGTCCGTGGT
Reg3g	TCTGCAAGACAGACAAGATGCT	GGGGCATCTTTCTTGGCAAC
Reg3b	ATGGCTCCTACTGCTATGCC	GTGTCCTCCAGGCCTCTT
Rps17	CGCCATTATCCCCAGCAAG	TGTCGGGATCCACCTCAATG
sig70S/A (C.r. DBS100 rpoD)	TCCAGCGTAGAGTCCGAAATC	TGCCCATTTCGCGCATAT
Genotyping primers		
cre recombinase	CGCGCTCTGGCAGTAAAAACTATC	CCCACCGTCAGTACGTGAGATATC

***Ex vivo* lipolysis assay.** *C. rodentium*-infected or unchallenged mice were fed control or 2 % carbonyl iron diets for a period of 6, 8 or 9 days and fasted in fresh cages for 6 hours with *ad libitum* access to water (time points indicated in figure legends). Inguinal and gonadal white adipose tissue pads were harvested, cut into 2 ~30-50 mg pieces and placed into separate wells in a 24 well plate with 300 µl of ice-cold PBS. Following the completion of tissue harvest, all fat pads were gently dabbed on a paper towel, cut with scissors in a central latitudinal location to introduce freshly cut exposed tissue, and carefully transferred to 24 well plates containing 300 µl of room-temperature Krebs-Ringer bicarbonate Hepes buffer ph 7.4 (120mM $NaCl_2$, 4mM KH_2PO_4, 1mM $MgSO_4$, 0.75 mM $CaCl_2$, 30 mM Hepes pH 7.4, 10mM $NaHCO_3$; solution was sterilized and stored at 4˚C until day of *ex vivo* lipolysis assay when fatty acid free bovine serum albumin (to 2% wbv) and D-glucose (5mM) was added. Plates were incubated for 4 hours in a 37˚C tissue culture incubator and supernatants were

transferred to fresh tubes and frozen at -20˚C until they were used to quantify free fatty acids and glycerol content as described below.

Free Fatty Acid and Glycerol content assays. *C. rodentium*-infected or unchallenged mice were fed control or 2 % carbonyl iron diets for a period of 6, 8 or 9 days and fasted in fresh cages for 6 hours with *ad libitum* access to water (time points indicated in figure legends). Serum or supernatant from *ex vivo* lipolysis assay were added to a 96 well plate according to the Wako Fuji Film protocol and reagents were added and incubated according to the manufacturers' protocols. Standards were generated using a dilution series of glycerol or non-esterified fatty acids (WAKO). A 1:2 dilution series from 1mM to 0.03125mM was used to generate the FFA standard curve. The standard curve for glycerol used the following series in mM: 8, 7, 6, 5, 4, 3, 2, 1, 0.5, 0.25. To determine FFA and glycerol content, 5 µl of samples and standards were used. Following methods outlined in manufacturer's protocols, samples were quantified from standard curve analyses using a 96-well VERSAmax microplate reader and SoftMax Pro software. FFA and glycerol levels from *ex vivo* lipolysis assays were normalized to recorded tissue masses.

Statistics. All variables were analyzed using GraphPad Prism 9.0e. Categorical variables are expressed as numbers and percentages, and quantitative variables as means ± standard error of the mean (SEM). Where data is shown as dot plots, each dot represents a single mouse or biological replicate. One-way analysis of variance (ANOVA) with a post Tukey's test or Two-way ANOVA were used as appropriate. Student's two tailed t-test was performed to evaluate the differences between two independent groups or paired samples as appropriate. A P value <0.05 was used to reject the null hypothesis. All experiments used an

n of 3 or more and represent 1-4 independent experiments. Further information regarding specific *P* values, *n* used, number of independent experiments performed for each figure, and how data are presented can be found in the figure legends.

3.3 Results

3.3.1 Dietary iron protects from C. rodentium-induced colitis

We have previously demonstrated that dietary iron promotes anti-virulence defenses against *C. rodentium* in a lethal model of transmissible murine colitis through inducing insulin resistance. We hypothesized that dietary iron supplementation could alter the pathogenicity of a non-lethal model of *C. rodentium*-induced colitis through modulation of organismal physiology. To examine the role of dietary iron in the progression and severity of *C. rodentium*-induced colitis model, we infected 6 week old C57BL/6 mice with *C. rodentium* through oral gavage and supplied either iron rich diet (IRD) (2% carbonyl iron supplemented) or a nutrient-matched control iron diet (CID) starting the same day as infection (**Figure 3.3.1A**). *C. rodentium* infection-induced colitis is characterized by colon shortening, mucosal damage and inflammation and development of colonic crypt hyperplasia [9,10]. Consistently, we observed colon shortening in *C.r.*-infected mice fed CID (**Figure 3.3.1B-C, Supplemental Figure 3.3.1A**) which was associated with increased histological colitis severity and splenomegaly (**Figure 3.3.1D-F, Supplemental Figure 3.3.1B)**. In comparison, mice fed IRD were protected from *C.r.*-induced colonic shortening, splenomegaly, and histopathological parameters of inflammation relative to uninfected controls (**Figure 3.3.1B-F, Supplemental Figure 3.3.1A,B,C)** [11]**.** In the same experiment, unchallenged mice fed IRD displayed increased hyperplasia and mucosal thickening relative to unchallenged mice fed CID, conceivably through inducing mild gastrointestinal inflammation that's reported during dietary iron supplementation (**Figure 3.3.1E-F, Supplemental Figure 3.3.1B,C**) [12,13]. As most of the pathology observed during *C.r.* infection is localized to the distal region of the colon, we next examined the mucosa, submucosa and muscularis of the distal colon for abnormalities[9,14–17]. Indeed, we observed significant thickening of the muscularis layer at the proximal end of the sphincter only in *C.r.*-infected mice fed CID (**Figure 3.3.1G-H**). Muscularis thickening was not

observed in any other region of the colon nor was it observed in unchallenged animals or animals fed IRD (**Figure 3.3.1G-H, Supplemental Figure 3.3.1C)**.

Colitis models are often accompanied by weight loss and wasting from reduced nutrient absorption and systemic inflammation [9,18]. We were surprised to find that while IRD-fed mice were protected from *C.r.*-induced colon shortening and pathology, all mice fed IRD exhibited significant weight loss compared to mice fed CID despite having comparable rates of food consumption after one day post infection (dpi) (**Figure 3.3.1I, Supplemental Figure 3.3.1D,E**). Together, these data show that IRD protects from *C.r.*-induced colitis both macroscopically and from colonic crypt hyperplasia, but induces weight loss in animals even in the absence of infection.

3.3.2 Dietary iron protects from colitis by promoting resistance defenses

To improve health during an infection, a host relies on two defense strategies that are distinguished by their effects on pathogen fitness[19]. Antagonistic defense strategies operate to kill and prevent colonization and expansion of pathogens while physiological defense strategies operate to prevent damage to the host while having a neutral to positive effect on pathogen fitness—yielding an apparent cooperation between the host and the pathogen. As described above, iron is regarded as collateral in antagonistic defenses and nutritional immunity encompasses host mechanisms that operate to starve pathogens of iron and prevent their expansion [1,2]. We therefore addressed whether IRD-induced protection from colitis was mediated through antagonistic or cooperative defenses (**Figure 3.3.2A-C**). In stark contrast to the principle of nutritional immunity, we found that CID-fed mice had increased fecal shedding of *C.r.* relative to mice fed IRD during the expansion phase of infection that occurs between dpi 3 and 9 (**Figure 3.3.2B)**. Likewise, mice fed CID had a corresponding increase in *C.r.* burden in gastrointestinal tissues and extraintestinal dissemination on dpi 8 (**Figure 3.3.2C**).

C. rodentium inoculum prepared from broth cultures will initially colonize the caecal lymphoid patch and establish a "seeding" population within the first three days of infection. The caecal population will subsequently colonize the distal region of the colon from dpi 4 onwards [14–17]. Because we observed decreased CFU in both the caecum and colons of IRD mice, we hypothesized that IRD also disrupts the colonization pattern of *C.r.* in the colon. We performed quantitative PCR on transcripts from the proximal and distal portions of the colon to measure expression of a *C.r.*-specific housekeeping gene (*C.r.* DBS100 *rpoD*) on dpi 8 [20]. We observed a relatively uniform distribution of *C.r.* expression in both colon portions of mice

fed CID–where the distal portion displayed an approximate two-fold increase in signal (**Figure 3.3.2D, Supplemental Figure 3.3.2A)**. In contrast, *C.r.* expression was blunted in the proximal end of mice fed IRD and was primarily detected in the distal colon (**Figure 3.3.2D, Supplemental Figure 3.3.2A).**

C. rodentium infection in C57BL/6 is characterized by a well-known sequence of events resulting in the development of colonic crypt hyperplasia and colitis [10,21]. The severity and progression of disease is marked by induction of host factors and expression of *C. rodentium*-encoded virulence factors. *C. rodentium* encodes the locus of enterocyte effacement (LEE) pathogenicity islands which expresses a type three secretion system (TTSS) and virulence factors required for expansion, attachment/effacement lesions and development of colonic crypt hyperplasia. We therefore examined expression of *C. rodentium* virulence factor expression and canonical innate immune signaling in colons from infected mice fed CID or IRD (**Figure 3.3.2E-G, Supplemental Figure 3.3.2B-D**). In agreement with our *C.r.* CFU data, we found increased expression of *C.r.* virulence factors in colons from mice fed CID, in which virulence factor expression mirrored that of housekeeping gene *rpoD*—suggesting that IRD does not prevent colitis through dampening *C.r.* virulence expression (**Figure 3.3.2E, Supplemental Figure 3.3.2B).** As for the innate immune cascade, when we analyzed the induction of host innate immune factors in *C.r.*-infected colons, induction of IL-17a, IL-22 and Lipocalin-2 was ablated in mice fed IRD in both the proximal and distal regions of the colon [22] (**Figure 3.3.2F, Supplemental Figure 3.3.2C**). However, we were surprised to find that IRD caused increased basal expression of antimicrobial peptides Reg3β and Reg3γ in the proximal colon of uninfected mice (**Figure 3.3.2G, Supplemental Figure 3.3.2D)**.

Together, these data demonstrate that contrary to the principle of nutritional immunity which predicts that an iron surplus will promote pathogen expansion and virulence expression, we show that dietary iron supplementation promotes host resistance defenses and does not impact virulence expression *in vivo*. IRD appears to promote resistance independent of canonical *C.r.*-induced innate inflammatory signaling, though it is conceivable that increased basal expression of antimicrobial peptides observed in IRD-fed mice may disrupt the colonization and pathogenesis of *C. rodentium*.

3.3.3 Iron promotes fat wasting during *C. rodentium* infection in an ATGL-dependent manner

Given the role of iron as an essential micronutrient in mammalian physiology and metabolism, we next asked how a dietary iron surplus affects systemic metabolism during *C. rodentium* infection. Inflammation and iron overload trigger a systemic response in which iron absorption is stalled in the gut, sequestered intracellularly, and depleted from circulation [4,23–25]. This response limits iron availability to pathogenic threats but initiates physiological rearrangements in host tissues. Most notably, iron overload can increase production of reactive oxygen species (ROS), induce ferroptosis, lipolysis, and is associated with insulin resistance [8,26]. In C3H/HeJ mice, dietary iron induces insulin resistance during *C.r.* infection and is necessary to promote anti-virulence defenses and survival [27]. However, iron did not induce insulin resistance in *C.r.*-infected C57BL/6 mice (**Supplemental Figure 3.3.3A-F)**, prompting us to consider other IRD-induced effects that could influence infection.

In Chapter 2, we found that IRD causes profound whole-body wasting in uninfected C57BL/6 mice, which was associated with marked wasting and lipolysis in subcutaneous and visceral white adipose tissues (WAT). As IRD appears to also drive whole-body wasting during *C.r.* infection (**Figure 3.3.1I**), we next examined the extent of IRD-induced effects on fat and lean tissues (**Figure 3.3.3A**).

Interestingly, compared to uninfected mice, *C.r.* infection did not cause a greater degree of fat or lean tissue wasting in mice fed IRD as is observed in mice fed CID (**Figure 3.3.3B-G**). All mice fed IRD exhibited a comparable decrease in total fat composition and subcutaneous (inguinal WAT) and visceral (gonadal WAT, mesenteric WAT) fat pads relative

to mice fed CID (**Figure 3.3.3C-E**). Lean body composition and hindlimb muscle masses were also significantly reduced in all mice fed IRD relative to CID-fed mice, suggesting that weight loss and wasting of lean and adipose tissue is dependent on IRD rather than infection (**Figure 3.3.3B-G**).

Because IRD induces white adipose tissue (WAT) lipolysis in unchallenged mice (Chapter 2), we used an *ex vivo* lipolysis assay to examine rates of WAT lipolysis from unchallenged and *C.r.*-infected mice fed CID or IRD. In line with our fat pad observations, there was increased secretion of free fatty acids (FFA) and glycerol from subcutaneous and visceral WAT from unchallenged mice fed IRD and in *C.r.*-infected mice (**Figure 3.3.3H-I**). All mice fed IRD or infected with *C.r.* displayed a moderate decrease in circulating levels of glycerol, conceivably to sustain increased metabolic demand and support gluconeogenesis (**Figure 3.3.3J**).

We demonstrated in unchallenged mice in Chapter 2 that IRD-induced fat wasting and lipolysis is mediated by adipose triglyceride lipase (ATGL) activity in subcutaneous WAT. Thus, we hypothesized that ATGL is also required to mediate IRD-induced fat wasting and lipolysis during *C.r.* infection. We therefore investigated the necessity of adipose-specific ATGL in mediating fat wasting and lipolysis during *C.r.* infection using a transgenic mouse line with an adipose-specific deletion of the gene *Pnpla2* encoding ATGL ($Pnpla2^{WAT\ KO}$) (**Figure 3.3.4A**). $Pnpla2^{WT}$ and $Pnpla2^{WAT\ KO}$ mice fed IRD had comparable weight loss over the course of infection (**Figure 3.3.4B, Supplemental Figure 3.3.4A**), but $Pnpla2^{WAT\ KO}$ mice had significantly greater fat composition relative to $Pnpla2^{WT}$ mice at dpi 9 (**Figure 3.3.4C**). In Chapter 2, we found that IRD-induced fat tissue wasting was ATGL-dependent in

subcutaneous but not visceral WAT depots. In contrast with the unchallenged model, both subcutaneous and visceral WAT masses were significantly greater in Pnpla2$^{WAT\ KO}$ mice fed IRD compared with Pnpla2^{WT}— suggesting that during *C.r.* infection, lipolytic stimuli acts through ATGL-dependent lipolysis in WAT (**Figure 3.3.4D-F**).

Unchallenged mice fed IRD undergo ATGL-dependent lipolysis to liberate FFA and glycerol from WAT in order to accommodate increased energy demands imposed by IRD. We found that inhibiting ATGL activity in adipose tissue drives increased wasting of lean energy stores—presumably to release muscle-derived substrates that support gluconeogenesis (Chapter 2). Given that Pnpla2$^{WAT\ KO}$ mice have reduced fat wasting on IRD, we hypothesized that we would observe increased wasting of lean tissues in Pnpla2$^{WAT\ KO}$ mice relative to Pnpla2^{WT} mice in order to accommodate increased energy demands imposed by infection and IRD. However, IRD caused comparable wasting of lean mass and hindlimb gastrocnemius muscle in *C.r.*-infected Pnpla2$^{WAT\ KO}$ and Pnpla2^{WT} mice (**Figure 3.3.4G, Supplemental Figure 3.3.4C**).

Because *C.r.*-infected Pnpla2$^{WAT\ KO}$ mice fed IRD exhibited reduced WAT wasting, we predicted this would correspond with decreased lipolysis and global lipid utilization. First, we performed an *ex vivo* lipolysis assay on *C.r.*-infected mice which confirmed that IRD did not increase secretion of FFA or glycerol from Pnpla2$^{WAT\ KO}$ WAT (**Figure 3.3.4H,I**). We next asked whether reduced lipolysis in Pnpla2$^{WAT\ KO}$ would result in decreased global lipid substrate utilization. We housed *C.r.*-infected Pnpla2^{WT} mice fed CID or IRD, and Pnpla2$^{WAT\ KO}$ mice fed IRD in Comprehensive Lab Animal Monitoring System (CLAMS) to measure gas exchange rates of O_2 and CO_2 and calculate respiratory exchange ratio (RER) over the

course of infection (**Figure 3.3.4J, Supplemental Figure 3.3.4D**). RER values close to 1.0 are indicative of carbohydrate utilization while values close to 0.7 indicate utilization of lipids [28]. Area under the curve (AUC) analysis of RER values showed that *C.r.*-infected Pnpla2$^{WAT\ KO}$ mice fed IRD exhibited a significant increase in RER values relative to Pnpla2^{WT} mice fed IRD, indicating decreased reliance on lipid energy substrates (**Figure 3.3.4J-K, Supplemental Figure 3.3.4D**). Further, we saw a significant decrease in circulating levels of FFA and glycerol in *C.r.*-infected Pnpla2$^{WAT\ KO}$ mice fed IRD—suggesting that the lack of adipose-derived lipolysis products leads to depletion of lipolysis-derived energy substrates in circulation (**Figure 3.3.4L**).

Together, these data suggest that IRD in combination with *C.r.* infection triggers a profound lipolytic stimulus that is mediated through ATGL in both subcutaneous and visceral adipose depots. However, the lack of lipolytic substrate in Pnpla2$^{WAT\ KO}$ mice does not drive increased lean tissue wasting but depletes circulating lipolysis-derived energy substrates.

3.3.4 Iron-induced fat wasting and lipolysis is dispensable for resistance during *C. rodentium* infection

Given that IRD induces fat wasting independent of infection, we next addressed if fat wasting is important for mediating IRD-induced resistance defenses during *C. rodentium* infection. To determine the causality of IRD-induced fat wasting in resistance defenses, we measured fecal shedding and gastrointestinal burdens of *C.r.* from Pnpla2^{WT} and Pnpla2 $^{WAT\ KO}$ mice fed CID or IRD (**Figure 3.3.5A**). *C.r.* fecal shedding and organ burdens were comparable in Pnpla2^{WT} and Pnpla2$^{WAT\ KO}$ mice fed IRD (**Figure 3.3.5B,C**), indicating that IRD-induced resistance is not mediated through fat wasting and lipolysis. Furthermore, IRD-induced fat wasting had no effect on *C.r.* colonization of proximal vs distal colon regions (**Figure 3.3.5D**). This result prompted us to examine if IRD-induced fat wasting mediates protection from pathology (**Figure 3.3.1**) through altering *C.r.* virulence expression and/or induction of the innate inflammatory response during infection. In line with our *C.r.* CFU and *C.r. rpoD* expression data, both Pnpla2^{WT} and Pnpla2 $^{WAT\ KO}$ mice fed IRD had a corresponding decrease in whole colon expression of *C.r.* virulence genes compared to mice fed CID (**Figure 3.3.5E-G**). Analysis of transcripts from proximal and distal colon sections confirmed that *C.r.* virulence factor expression mirrored that of housekeeping gene *rpoD*—suggesting that IRD-induced lipolysis does not alter *C.r.* virulence expression (**Supplemental Figure 3.3.5A,B**). Further, we found that IRD-induced lipolysis is not necessary to blunt the induction of innate immune signaling in whole colons or colon regions (**Figure 3.3.5F,G, Supplemental Figure 3.3.6A-D**). Together, these findings demonstrate that dietary iron supplementation promotes resistance defenses and disrupts *C.r.* pathogenesis independent of induction of fat wasting and lipolysis.

3.3.5 Iron-induced lipolysis is necessary to prevent colon shortening and remodeling during *C. rodentium* infection

IRD protects from *C. rodentium*-induced colitis both macroscopically and in regards to tissue pathology (**Figure 3.3.1**). IRD promotes weight loss and fat wasting independent of colitis severity, yet, fat wasting is dispensable for promoting resistance defenses. Thus, we hypothesized that IRD-induced fat wasting and lipolysis may be important to mediate protection from IRD-dependent protection from *C.r.*-induced colitis.

Colon lengths were comparable between unchallenged Pnpla2^{WT} and Pnpla2$^{WAT\ KO}$ mice fed CID or IRD—confirming that colon length is not affected by diet or IRD-induced lipolysis (**Supplemental Figure 3.3.7A**). We examined colons on dpi 6 and 9 from Pnpla2^{WT} and Pnpla2$^{WAT\ KO}$ mice fed CID or IRD (**Figure 3.3.6A**) and were surprised to find that colons from Pnpla2$^{WAT\ KO}$ mice fed IRD were significantly shortened compared to colons from Pnpla2^{WT} mice fed IRD (**Figure 3.3.6B-D, Supplemental Figure 3.3.7B**). However, colonic shortening in IRD-fed Pnpla2$^{WAT\ KO}$ mice was not associated with increased mucosal damage and pathology or splenomegaly—such that Pnpla2$^{WAT\ KO}$ and Pnpla2^{WT} mice fed IRD showed comparable pathology scores and spleen mass (**Figure 3.3.6E-G, Supplemental Figure 3.3.7C,D**). Though colon shortening is typically associated with mucosal damage, there is no previous association between colitis, colon shortening and distal muscle thickening. In wildtype mice infected with *C.r.*, we found that colitis is accompanied by a thickening of the distal muscularis preceding the sphincter. Though shortened colons from Pnpla2$^{WAT\ KO}$ mice fed IRD did not exhibit increased mucosal damage, we observed thickening of the distal muscularis layer (**Figure 3.3.6H,I**). Thus, our data demonstrate that IRD induces a novel colon remodeling program that is dependent on adipose-specific ATGL

during *C.r.* infection. Dietary iron supplementation protects from colon shortening and distal muscularis thickening that is induced during *C.r.* infection—presumably through induction of WAT lipolysis that is dependent on adipose tissue activation of ATGL.

Together, these data suggest that colonic crypt hyperplasia and traditional histopathological markers of colitis are dependent on both the colonization pattern and expansion of *C.r.* that lead to the induction of the innate immune cascade. Further, our model features the first instance of macroscopic markers of infectious colitis being uncoupled from histopathological and molecular markers of colitis (**Figure 3.3.7**). We found that the widely observed feature of colonic shortening is solely dependent on the incidence of *C.r.* colonization rather than the expansion of *C.r.* and induction of virulence expression and inflammatory signaling cascade. Altogether, our study highlights a role for iron in modulating host defense in a non-lethal model of transmissible murine colitis beyond the principle of nutritional immunity.

3.4 Discussion

Iron has long been regarded as a centerpiece in an evolutionary tug-of-war between host and invading pathogens. Both parties have coevolved intricate systems to acquire and regulate iron levels that function to promote survival and fitness. More recently, this principle has been challenged and iron has been shown to be beneficial to host health under certain contexts of infectious challenge—highlighting the importance of iron in influencing infection outcomes independent of restricting pathogen's access to iron [1–4,24]. For instance, iron supplementation was found to promote resistance to mycobacterial infection in mice while reducing inflammation and recruitment of neutrophils and macrophages [29]. Along the same lines, dietary iron supplementation prior to and throughout *C. rodentium* infection reduced colon inflammation and lipocalin-2 production while having no effect on bacterial burdens—demonstrating that iron supplementation does not promote pathogen fitness [20]. A related relationship has also been observed in *Helicobacter pylori* infections, where iron deficiency promotes *H. pylori* virulence expression and gastric pathology [30,31]. In tangential work, our lab found that dietary iron supplementation transiently induces insulin resistance in C3H/HeJ mice and enables anti-virulence defenses in a lethal model of infectious colitis [27]. These studies collectively show that 1) iron does not reside solely in the realm of antagonistic defenses, and 2) iron's physiological role in host defense is highly context dependent in regards to mouse background, tropism and infection models [1,2,4,24]. Altogether, the principle of nutritional immunity does not account for the complex physiological host defense mechanisms that are important for modulating the progression and severity of infectious disease.

Iron has proven to be beneficial under certain infectious challenges through promoting resistance or dampening virulence. Our study further demonstrates that contrary to the principle of nutritional immunity, iron excess can negatively impact a pathogen's fitness. We found that dietary iron supplementation promotes resistance against *C. rodentium* independent of induction of the host innate inflammatory cascade. This is consistent with reports where hepcidin treatment blunts the inflammatory response of mice challenged with a sub lethal dose of lipopolysaccharide (LPS) or during polymicrobial sepsis [32–35], setting a precedent for observations in the current model. Although we found increased basal expression of antimicrobial peptides Reg3β and Reg3γ in the proximal region of the colon in iron supplemented mice, it is unlikely that *C. rodentium* burden is directly impacted by increased Reg3 production [36]. Rather, Zheng and colleagues showed that ablating the IL-22/Reg3 axis does not directly impact loads of cecal or colonic *C. rodentium* and likely prevents *C. rodentium* from invading colonic crypts [22]. Thus, we speculate that iron-induced upregulation of Reg3 expression in the our study may alter mucosal-associated microbe composition and hinder the ability of *C. rodentium* to access this niche. Reg3β and Reg3γ are proposed to maintain barrier integrity through promoting wound healing and proliferation of the epithelium during inflammation—conceivably to limit extraintestinal dissemination of microbiota during infection and inflammatory states [22,37]. Thus, it is possible that iron-induced Reg3 upregulation limits dissemination of *C. rodentium* into systemic organs in mice fed IRD. Additionally, iron supplementation caused hyperplasia and mild pathology in unchallenged mice, which may be due in part, to the proliferative effects of Reg3. However, we are unable to determine whether iron-induced upregulation of Reg3 promotes colonic hyperplasia or iron-induced hyperplasia promotes Reg3 expression.

Though host immune factors influence the severity of *C. rodentium* infection, *C. rodentium* infection is largely influenced by the microbiome and the mucosal microenvironment [21,38]. Prior to defining the genetic underpinnings of susceptibility to *C. rodentium*[17,39] *,* the microbiome was considered to be the deterministic factor in susceptibility to severe infection and mortality[40]. Transplantation of microbiomes between susceptible and resistant populations following antibiotic treatment determined *C. rodentium* infection severity and outcomes, including survival [41,42]. It has since been shown that the microbiome is necessary for *C. rodentium* expansion in the distal colon and provides signals that promote virulence expression [14,16,21,43]. The microbiome is also necessary to mediate clearance of virulent *C. rodentium* and certain members of the microbiome are capable of mediating colonization resistance and exclusion of *C. rodentium* through nutrient competition [14,43]*.* This phenomena is also observed for other pathogens in the same family as *C. rodentium* [44]. Further, *C. rodentium* infection itself initiates remodeling of the microbiome that occurs during the expansion phase of infection (dpi 4-9)[45]. *C. rodentium* expansion is associated with depletion of beneficial members of the phyla Firmicutes and Bacteroides and enrichment in the abundance of facultative anaerobes from the phylum Proteobacteria—in particular, those belonging to the family *Enterobacteriaceae* [15,46]. These studies prompted others to investigate whether host encode mechanisms that can alter the gut environment in favor of facultative anaerobes to promote colonization resistance and clearance of pathogens. In support of this, Yang and colleagues found that TLR9 signaling contributes to colonization resistance against *C. rodentium* by dampening induction of antimicrobial peptides [47].

It's been proposed that enteric pathogens harboring type 3 secretion systems, like *C. rodentium,* utilize virulence factors to as a means to disrupt colonocyte mitochondrial

function, generate attaching and effacing lesions, and promote proliferation through oxygenation of the colonic lumen [48,49]. Luminal oxygenation not only promotes expansion of *C. rodenitum,* but it is considered to be a general virulence strategy for opportunistic pathogens and other facultative anaerobic enteric pathogens like *Salmonella enterica* Typhimurium [50]. At any rate, utilization of virulence factors that promote luminal oxygenation allows facultative anaerobes to proliferate such that the normal flora is disrupted. We found that on the organ level, iron supplementation decreased virulence expression. However, in examining virulence expression in distinct colon regions, virulence expression was scaled with pathogen burdens. Thus, iron supplementation does not appear to impact the virulence program of *C. rodentium*, and therefore, virulence factor expression does not provide a fitness advantage in the current model.

In terms of timing, our data suggests that iron-mediated resistance occurs during the colonization phase of infection and is likely to be dependent on the microbiome. The general shift of gut microbiome composition towards increased abundance of *Enterobacteriaceae* and reduction in Firmicutes and Bacteroides is associated with inflammatory states and diseases, antibiotic administration as well as western-style diets [38,51,52]. Indeed, a similar microbiome composition is observed in mice and patients receiving iron supplementation [12,13,53,54]. Though oral iron supplementation is known to drastically alter composition of the gut microbiome, both intravenous (i.v.) and dietary routes of administration cause a marked effect on microbiome composition [55]. Similar to inflammatory diseases, iron promotes the expansion of facultative anaerobes that are known to outcompete *C. rodentium* in the clearance phase of infection [53]. Consistent with this, we observed growth of *Enterobacteriaceae* members in stool from *C. rodenitium* infected mice fed an iron rich diet

and this was not observed in mice fed control diets (data not shown). Notably, because dietary iron supplementation itself caused marked hyperplasia in colons of unchallenged animals in our study, this may be sufficient to disrupt the mucosal microenvironment such that facultative anaerobic commensals would bloom [45]. However, the we cannot uncouple the effects of iron excess and mild colonic inflammation on the mucosal microenvironment and presumed alterations of the microbiome.

Altogether, we propose that iron supplementation itself, or iron-mediated hyperplasia and colon inflammation promotes a bloom of *Enterobacteriaceae* in the colonization phase of *C. rodentium* infection (dpi0-4), thus limiting expansion but not virulence expression of *C. rodentium* and disrupting normal colonization within the caecum and colon. Our findings raise the intriguing perspective that preemptive induction of mild intestinal inflammation may be beneficial in preventing more severe infection outcomes.

Colon shortening is a hallmark associated with gastrointestinal inflammatory diseases ranging from infection-induced colitis to inflammatory bowel diseases [9,18,56–58]. Due to the association with inflammatory states, colon shortening has been used as a macroscopic indicator of colitis that is coupled with inflammatory signaling cascades and histological damage to the epithelium—especially in mouse models of gastrointestinal disease. Our study marks the first report wherein infection-induced colon shortening occurs independent of canonical histopathological features of inflammation or expression of innate inflammatory cascades. Thus, our finding prompts a reexamination of the etiology of infectious colitis and the colon shortening response associated with inflammation and infectious colitis.

In the handful of works that have discussed the etiology of colon shortening, propositions into the cause of colon shortening have ranged from mucosal thickening and hyperplasia, to hypertrophy of the muscularis, to fibrosis [18,59,60]. Our study demonstrates that neither mucosal thickening nor hypertrophy of the circular or longitudinal colonic muscularis layers (preceding the rectal region) are necessary for colon shortening. Moreover, substantial epithelial thickening was observed in unchallenged mice fed IRD where colon shortening was absent—confirming that mucosal hyperplasia alone does not cause colon shortening. Thus, it is conceivable that colon shortening may be dependent on fibrosis of the submucosa or muscularis [60]. However, we did not find evidence to support an increase in fibrosis or fibrotic signaling cascades in shortened colons in our study (data not shown), though a more thorough investigation is necessary to confirm this.

In 1992, Gore proposed that colon shortening observed during ulcerative colitis in humans may be due to enlargement or sustained contraction of longitudinally oriented muscularis mucosae rather than mucosal damage itself [61]. In support of this, a recent investigation into the physiological function of proto-oncogene c-Abl, found that c-Abl deficient mice display thickening of smooth muscle along the gastrointestinal tract. Smooth muscle thickening, particularly in the colon-rectum region, was associated with rectal prolapse and colon shortening. Smooth muscle thickening and rectal prolapse was not associated with increased mucosal damage, inflammatory signaling or differences in $CD3^+$ cell infiltration [62]. This study demonstrates that similar to our findings, colon shortening and rectal muscularis thickening can occur independent of inflammation and mucosal damage. We thus speculate that colon shortening observed in *C. rodentium* infection may be dependent on smooth muscle thickening and dysfunction within the distal colon.

Though we found no evidence of structural differences in muscularis layers preceding the rectal muscularis, it has also been proposed that muscularis function is compromised in colitis models, potentially leading to the macroscopic feature of colon shortening [63–65]. For example, gastrointestinal motility can become compromised in inflammatory diseases and colitis, leading to disruptions to peristalsis and slowed passage of luminal content . In the basal enteric environment, colonic motility is initiated by distention of the colonic walls or serotonin release, which induce the coordinated contraction/relaxation of longitudinal and circular smooth muscle to pass luminal contents towards the distal end of the colon. This intestinal muscle layer is comprised of resident macrophages, myenteric plexus and the inner muscle regions that orchestrate normal enteric transit [66]. Inflammatory states such as intestinal bowel disease (IBD), enteric infections, and allergic diarrhea, can impair the ability of the intestinal muscle layer to coordinate regular bowel movement along the gastrointestinal tract [63,67]. *C. rodentium* infection induces a robust innate inflammatory response that alters serotonin availability and nitric oxide production and altogether impairs gastrointestinal motility and peristalsis [68,69]. It is therefore intriguing to speculate on the additive effects that smooth muscle function and structure elicit on colon length during enteric infection.

We were astounded to discover that colon remodeling, including colon shortening and distal muscularis thickening, occur independent of inflammation and are ablated by iron-induced lipolysis in white adipose tissue (WAT). We found that *C. rodentium* colonization is sufficient to induce colon shortening when fat wasting and lipolysis are minimal. Our discovery raises the question of how adipose tissue and organismal lipid metabolism influence host defense responses in the gut and what mechanisms mediate the crosstalk

between adipose tissue and gut. There is an established association between colitis susceptibility and gastrointestinal inflammation and increased adiposity or western-style diets [56,70–73]. However, in the context of C. *rodentium*-induced colitis, increased adiposity and high fat diet are reported to differentially impact host defenses and disease severity through distinct mechanisms [27,38,71]. With the additional complexity of dietary iron overloading, our model likely reflects a novel relationship between adipose tissue and *C. rodentium*-induced colitis.

It is well appreciated that adipose tissue and organismal lipid metabolism are intricately linked with metabolic status, inflammation and infection [74–77]. Moreover, the recent appreciation of adipose tissue as an endocrine organ has spurred investigation into the adipose-gut axis [78,79]. These relationships are mediated through direct interactions with microbiota and pathogens, bidirectional endocrine signaling, and endogenous lipid mediators. First, microbes are known to directly interact with or colonize white adipose tissue (WAT). *Escherichia coli*, *Plasmodium*, *Trypanosoma* and viral infections can occupy or colonize WAT, though there is still considerable debate over the *pourquoi tale* of adipose-resident infections [80,81]. It has also been demonstrated that WAT colonization can be beneficial to the host. In murine sepsis models, *Escherichia coli* serotype O21:H+ translocates form the gut to WAT and induces upregulation of insulin growth factor (IGF)—leading to maintenance of muscle mass and promoting survival from systemic infections [82]. Additionally, inflammation and translocation of microbes into visceral fat and mesenteric fat is associated with Crohn's disease and induces the formation of *creeping fat* [83]. "Creeping fat" is observed as a macroscopic marker of lesions in colonic and illeal Crohn's disease [84,85]. However, creeping fat is not commonly observed in ulcerative colitis and is therefore less

relevant to *C. rodentium* induced colitis whose pathology is more similar to ulcerative colitis. Nonetheless, mesenteric fat, with such close proximity to the colon, is observed to have a bidirectional influence over the severity of Crohn's disease and influence the immune milieu of the gut in response to inflammation and infection, raising the possibility the maintenance of visceral adipose tissue promotes ultrastructural rearrangements in the colon [86,87].

Recently, adipose iron content has been shown to modulate lipid absorption in the gut such that iron depletion in white adipocytes confers resistance to high fat diet induced obesity and development of insulin resistance in mice[88]. Importantly, iron-replete adipose transplants into mice with iron-depleted adipose tissue was sufficient to increase nutrient absorption; demonstrating that adipose tissue releases endocrine signals that directly modulate intestinal function [88]. Interorgan crosstalk between gut and adipose tissue can also be modulated by translocation of anti-inflammatory macrophages from the gut to adipose tissue [89]. Specific *Lactobacillus* strains were found to increase abundance of anti-inflammatory macrophages that afford protection from HFD-induced obesity when they migrate to adipose tissue [89].

Adipokines also play a significant role in gut health. Leptin, a satiety hormone whose levels are directly correlated with adiposity, has been implicated in gut health and inflammatory states. Leptin has inflammatory effects in the gut, suggesting that increased adiposity may contribute to gut inflammation at least in part, through adipokines [90–93]. Given that iron induces fat wasting in our study, we propose that fat wasting could be beneficial by decreasing the abundance of circulating inflammatory adipokines like leptin. Importantly,

leptin is influenced by iron status as well. Iron levels negatively regulate leptin production in adipose tissue [94]. Thus, the combination of iron overload and reduced adipose tissue may substantially decrease leptin levels and dampen inflammation during *C. rodentium* infection [94,95].

Finally, adiposity can be beneficial and maladaptive hyperglycemia and obesity are associated with poor health metrics as are minimal adiposity and hypolipidemia [71,78,96,97]. However, in general, fat wasting is associated with poor prognoses during infection. Yet, recent studies in invertebrates have demonstrated that fat wasting can impart an energy tradeoff in the form of reproduction/lifespan reduction in order to promote host defenses [96,98,99]. Thus, our model falls along these lines and shows that fat wasting is beneficial in protecting from colon remodeling but is likely maladaptive for organismal health. As fat wasting is induced by iron itself, there's likely a cost associated with iron-induced fat wasting that we did not detect in the current study.

3.5 Acknowledgements

Chapter 3 is currently being prepared for submission for publication of the material in the working citation: **Romero, A.R.,** Gerner, R.G., Ayres, J.S., Iron-induced metabolic rearrangements uncouple hallmarks of infectious colitis. The dissertation author was a primary investigator and the first author of this material. The authors would like to thank Dr. Justin McCarville and Dr. Grischa Chen (Ayres Lab) for thoughtful discussions and Zbignew and Kasia at La Jolla Institute of Immunology for technical guiance with histology.

3.6 References

1. Gerner, R. R., Nuccio, S.-P. & Raffatellu, M. Iron at the host-microbe interface. *Mol. Aspects Med.* **75**, 100895 (2020).

2. Chen, G. Y. & Ayres, J. S. Beyond tug-of-war: Iron metabolism in cooperative host–microbe interactions. *PLOS Pathog.* **16**, e1008698 (2020).

3. Kortman, G. A. M., Raffatellu, M., Swinkels, D. W. & Tjalsma, H. Nutritional iron turned inside out: intestinal stress from a gut microbial perspective. *FEMS Microbiol. Rev.* **38**, 1202–1234 (2014).

4. Ganz, T. & Nemeth, E. Iron homeostasis in host defence and inflammation. *Nat. Rev. Immunol.* **15**, 500–510 (2015).

5. Coffey, R. & Ganz, T. Iron homeostasis: An anthropocentric perspective. *J. Biol. Chem.* **292**, 12727–12734 (2017).

6. Simcox, J. A. & McClain, D. A. Iron and Diabetes Risk. *Cell Metab.* **17**, 329–341 (2013).

7. Gordeuk, V. R. Hereditary and nutritional iron overload. *Baillières Clin. Haematol.* **5**, 169–186 (1992).

8. Pantopoulos, K. Inherited Disorders of Iron Overload. *Front. Nutr.* **5**, 103 (2018).

9. Mundy, R., MacDonald, T. T., Dougan, G., Frankel, G. & Wiles, S. Citrobacter rodentium of mice and man. *Cell. Microbiol.* **7**, 1697–1706 (2005).

10. Collins, J. W., Keeney, K. M., Crepin, V. F., Rathinam, V. A. K., Fitzgerald, K. A., Finlay, B. B. & Frankel, G. Citrobacter rodentium: infection, inflammation and the microbiota. *Nat. Rev. Microbiol.* **12**, 612–623 (2014).

11. Moschen, A. R., Gerner, R. R., Wang, J., Klepsch, V., Adolph, T. E., Reider, S. J., Hackl, H., Pfister, A., Schilling, J., Moser, P. L., Kempster, S. L., Swidsinski, A., Orth Höller, D., Weiss, G., Baines, J. F., Kaser, A. & Tilg, H. Lipocalin 2 Protects from Inflammation and Tumorigenesis Associated with Gut Microbiota Alterations. *Cell Host Microbe* **19**, 455–469 (2016).

12. Mahalhal, A., Williams, J. M., Johnson, S., Ellaby, N., Duckworth, C. A., Burkitt, M. D., Liu, X., Hold, G. L., Campbell, B. J., Pritchard, D. M. & Probert, C. S. Oral iron exacerbates colitis and influences the intestinal microbiome. *PLoS ONE* **13**, e0202460 (2018).

13. Jaeggi, T., Kortman, G. A. M., Moretti, D., Chassard, C., Holding, P., Dostal, A., Boekhorst, J., Timmerman, H. M., Swinkels, D. W., Tjalsma, H., Njenga, J., Mwangi, A., Kvalsvig, J., Lacroix, C. & Zimmermann, M. B. Iron fortification adversely affects the gut microbiome, increases pathogen abundance and induces intestinal inflammation in Kenyan infants. *Gut* **64**, 731–742 (2015).

14. Mullineaux-Sanders, C., Collins, J. W., Ruano-Gallego, D., Levy, M., Pevsner-Fischer, M., Glegola-Madejska, I. T., Sågfors, A. M., Wong, J. L. C., Elinav, E., Crepin, V. F. & Frankel, G. Citrobacter rodentium Relies on Commensals for Colonization of the Colonic Mucosa. *Cell Rep.* **21**, 3381–3389 (2017).

15. Hopkins, E. G. D., Roumeliotis, T. I., Mullineaux-Sanders, C., Choudhary, J. S. & Frankel, G. Intestinal Epithelial Cells and the Microbiome Undergo Swift Reprogramming at the Inception of Colonic Citrobacter rodentium Infection. *mBio* **10**, e00062-19.

16. Wiles, S., Clare, S., Harker, J., Huett, A., Young, D., Dougan, G. & Frankel, G. Organ specificity, colonization and clearance dynamics in vivo following oral challenges with the murine pathogen Citrobacter rodentium. *Cell. Microbiol.* **6**, 963–972 (2004).

17. Carson, D., Barry, R., Hopkins, E. G. D., Roumeliotis, T. I., García-Weber, D., Mullineaux-Sanders, C., Elinav, E., Arrieumerlou, C., Choudhary, J. S. & Frankel, G. Citrobacter rodentium induces rapid and unique metabolic and inflammatory responses in mice suffering from severe disease. *Cell. Microbiol.* **22**, (2020).

18. Bhinder, G., Sham, H. P., Chan, J. M., Morampudi, V., Jacobson, K. & Vallance, B. A. The Citrobacter rodentium Mouse Model: Studying Pathogen and Host Contributions to Infectious Colitis. *J. Vis. Exp. JoVE* 50222 (2013) doi:10.3791/50222.

19. Ayres, J. S. Cooperative Microbial Tolerance Behaviors in Host-Microbiota Mutualism. *Cell* **165**, 1323–1331 (2016).

20. Kortman, G. A. M., Mulder, M. L. M., Richters, T. J. W., Shanmugam, N. K. N., Trebicka, E., Boekhorst, J., Timmerman, H. M., Roelofs, R., Wiegerinck, E. T., Laarakkers, C. M., Swinkels, D. W., Bolhuis, A., Cherayil, B. J. & Tjalsma, H. Low dietary iron intake restrains the intestinal inflammatory response and pathology of enteric infection by food-borne bacterial pathogens: Immunity to infection. *Eur. J. Immunol.* **45**, 2553–2567 (2015).

21. Mullineaux-Sanders, C., Sanchez-Garrido, J., Hopkins, E. G. D., Shenoy, A. R., Barry, R. & Frankel, G. Citrobacter rodentium–host–microbiota interactions: immunity, bioenergetics and metabolism. *Nat. Rev. Microbiol.* **17**, 701–715 (2019).

22. Zheng, Y., Valdez, P. A., Danilenko, D. M., Hu, Y., Sa, S. M., Gong, Q., Abbas, A. R., Modrusan, Z., Ghilardi, N., de Sauvage, F. J. & Ouyang, W. Interleukin-22 mediates early host defense against attaching and effacing bacterial pathogens. *Nat. Med.* **14**, 282–289 (2008).

23. Weinberg, E. D. Nutritional Immunity: Host's Attempt to Withhold Iron From Microbial Invaders. *JAMA* **231**, 39 (1975).

24. Lopez, C. A. & Skaar, E. P. The Impact of Dietary Transition Metals on Host-Bacterial Interactions. *Cell Host Microbe* **23**, 737–748 (2018).

25. Núñez, G., Sakamoto, K. & Soares, M. P. Innate Nutritional Immunity. *J. Immunol.* **201**, 11–18 (2018).

26. Conway, D. & Henderson, M. A. Iron metabolism. *Anaesth. Intensive Care Med.* **20**, 175–177 (2019).

27. Sanchez, K. K., Chen, G. Y., Schieber, A. M. P., Redford, S. E., Shokhirev, M. N., Leblanc, M., Lee, Y. M. & Ayres, J. S. Cooperative Metabolic Adaptations in the Host Can Favor Asymptomatic Infection and Select for Attenuated Virulence in an Enteric Pathogen. *Cell* **175**, 146-158.e15 (2018).

28. Speakman, J. R. Measuring Energy Metabolism in the Mouse – Theoretical, Practical, and Analytical Considerations. *Front. Physiol.* **4**, (2013).

29. Agoro, R., Benmerzoug, S., Rose, S., Bouyer, M., Gozzelino, R., Garcia, I., Ryffel, B., Quesniaux, V. F. J. & Mura, C. An Iron-Rich Diet Decreases the Mycobacterial Burden and Correlates With Hepcidin Upregulation, Lower Levels of Proinflammatory Mediators, and Increased T-Cell Recruitment in a Model of Mycobacterium bovis Bacille Calmette-Guerin Infection. *J. Infect. Dis.* **216**, 907–918 (2017).

30. Merrell, D. S., Thompson, L. J., Kim, C. C., Mitchell, H., Tompkins, L. S., Lee, A. & Falkow, S. Growth Phase-Dependent Response of Helicobacter pylori to Iron Starvation. *Infect. Immun.* (2003) doi:10.1128/IAI.71.11.6510-6525.2003.

31. Beckett, A. C., Piazuelo, M. B., Noto, J. M., Peek, R. M., Washington, M. K., Algood, H. M. S. & Cover, T. L. Dietary Composition Influences Incidence of Helicobacter

pylori-Induced Iron Deficiency Anemia and Gastric Ulceration. *Infect. Immun.* **84**, 3338–3349 (2016).

32. Pagani, A., Nai, A., Corna, G., Bosurgi, L., Rovere-Querini, P., Camaschella, C. & Silvestri, L. Low hepcidin accounts for the proinflammatory status associated with iron deficiency. *Blood* **118**, 736–746 (2011).

33. Domenico, I. D., Zhang, T. Y., Koening, C. L., Branch, R. W., London, N., Lo, E., Daynes, R. A., Kushner, J. P., Li, D., Ward, D. M. & Kaplan, J. Hepcidin mediates transcriptional changes that modulate acute cytokine-induced inflammatory responses in mice. https://www.jci.org/articles/view/42011/pdf (2010) doi:10.1172/JCI42011.

34. Wang, L., Johnson, E. E., Shi, H. N., Walker, W. A., Wessling-Resnick, M. & Cherayil, B. J. Attenuated Inflammatory Responses in Hemochromatosis Reveal a Role for Iron in the Regulation of Macrophage Cytokine Translation. *J. Immunol.* **181**, 2723–2731 (2008).

35. Wang, L., Harrington, L., Trebicka, E., Shi, H. N., Kagan, J. C., Hong, C. C., Lin, H. Y., Babitt, J. L. & Cherayil, B. J. Selective modulation of TLR4-activated inflammatory responses by altered iron homeostasis in mice. *J. Clin. Invest.* **119**, 3322–3328 (2009).

36. Shin, J. H. & Seeley, R. J. Reg3 Proteins as Gut Hormones? *Endocrinology* **160**, 1506–1514 (2019).

37. Pickert, G., Neufert, C., Leppkes, M., Zheng, Y., Wittkopf, N., Warntjen, M., Lehr, H.-A., Hirth, S., Weigmann, B., Wirtz, S., Ouyang, W., Neurath, M. F. & Becker, C. STAT3 links IL-22 signaling in intestinal epithelial cells to mucosal wound healing. *J. Exp. Med.* **206**, 1465–1472 (2009).

38. An, J., Zhao, X., Wang, Y., Noriega, J., Gewirtz, A. T. & Zou, J. Western-style diet impedes colonization and clearance of Citrobacter rodentium. *PLOS Pathog.* **17**, e1009497 (2021).

39. Papapietro, O., Teatero, S., Thanabalasuriar, A., Yuki, K. E., Diez, E., Zhu, L., Kang, E., Dhillon, S., Muise, A. M., Durocher, Y., Marcinkiewicz, M. M., Malo, D. & Gruenheid, S. R-Spondin 2 signalling mediates susceptibility to fatal infectious diarrhoea. *Nat. Commun.* **4**, 1898 (2013).

40. Bäumler, A. J. & Sperandio, V. Interactions between the microbiota and pathogenic bacteria in the gut. *Nature* **535**, 85–93 (2016).

41. Willing, B. P., Vacharaksa, A., Croxen, M., Thanachayanont, T. & Finlay, B. B. Altering host resistance to infections through microbial transplantation. *PloS One* **6**, e26988 (2011).

42. Ghosh, S., Dai, C., Brown, K., Rajendiran, E., Makarenko, S., Baker, J., Ma, C., Halder, S., Montero, M., Ionescu, V. A., Klegeris, A., Vallance, B. A. & Gibson, D. L. Colonic microbiota alters host susceptibility to infectious colitis by modulating inflammation, redox status, and ion transporter gene expression. *Am. J. Physiol. Gastrointest. Liver Physiol.* **301**, G39-49 (2011).

43. Kamada, N., Kim, Y.-G., Sham, H. P., Vallance, B. A., Puente, J. L., Martens, E. C. & Núñez, G. Regulated Virulence Controls the Ability of a Pathogen to Compete with the Gut Microbiota. *Science* **336**, 1325–1329 (2012).

44. Oliveira, R. A., Ng, K. M., Correia, M. B., Cabral, V., Shi, H., Sonnenburg, J. L., Huang, K. C. & Xavier, K. B. Klebsiella michiganensis transmission enhances resistance to Enterobacteriaceae gut invasion by nutrition competition. *Nat. Microbiol.* **5**, 630–641 (2020).

45. Lupp, C., Robertson, M. L., Wickham, M. E., Sekirov, I., Champion, O. L., Gaynor, E. C. & Finlay, B. B. Host-Mediated Inflammation Disrupts the Intestinal Microbiota and Promotes the Overgrowth of Enterobacteriaceae. *Cell Host Microbe* **2**, 119–129 (2007).

46. Berger, C. N., Crepin, V. F., Roumeliotis, T. I., Wright, J. C., Carson, D., Pevsner-Fischer, M., Furniss, R. C. D., Dougan, G., Dori-Bachash, M., Yu, L., Clements, A., Collins, J. W., Elinav, E., Larrouy-Maumus, G. J., Choudhary, J. S. & Frankel, G. Citrobacter rodentium Subverts ATP Flux and Cholesterol Homeostasis in Intestinal Epithelial Cells In Vivo. *Cell Metab.* **26**, 738-752.e6 (2017).

47. Yang, H., Yu, H. B., Bhinder, G., Ryz, N. R., Lee, J., Yang, H., Fotovati, A., Gibson, D. L., Turvey, S. E., Reid, G. S. & Vallance, B. A. TLR9 limits enteric antimicrobial responses and promotes microbiota-based colonisation resistance during Citrobacter rodentium infection. *Cell. Microbiol.* **21**, e13026 (2019).

48. Lopez, C. A., Miller, B. M., Rivera-Chavez, F., Velazquez, E. M., Byndloss, M. X., Chavez-Arroyo, A., Lokken, K. L., Tsolis, R. M., Winter, S. E. & Baumler, A. J. Virulence factors enhance Citrobacter rodentium expansion through aerobic respiration. *Science* **353**, 1249–1253 (2016).

49. Byndloss, M. X., Olsan, E. E., Rivera-Chávez, F., Tiffany, C. R., Cevallos, S. A., Lokken, K. L., Torres, T. P., Byndloss, A. J., Faber, F., Gao, Y., Litvak, Y., Lopez, C. A., Xu, G., Napoli, E., Giulivi, C., Tsolis, R. M., Revzin, A., Lebrilla, C. B. & Bäumler,

A. J. Microbiota-activated PPAR-γ signaling inhibits dysbiotic Enterobacteriaceae expansion. *Science* **357**, 570–575 (2017).

50. Rivera-Chávez, F., Zhang, L. F., Faber, F., Lopez, C. A., Byndloss, M. X., Olsan, E. E., Xu, G., Velazquez, E. M., Lebrilla, C. B., Winter, S. E. & Bäumler, A. J. Depletion of Butyrate-Producing Clostridia from the Gut Microbiota Drives an Aerobic Luminal Expansion of Salmonella. *Cell Host Microbe* **19**, 443–454 (2016).

51. Lee, J.-Y., Cevallos, S. A., Byndloss, M. X., Tiffany, C. R., Olsan, E. E., Butler, B. P., Young, B. M., Rogers, A. W. L., Nguyen, H., Kim, K., Choi, S.-W., Bae, E., Lee, J. H., Min, U.-G., Lee, D.-C. & Bäumler, A. J. High-Fat Diet and Antibiotics Cooperatively Impair Mitochondrial Bioenergetics to Trigger Dysbiosis that Exacerbates Pre-inflammatory Bowel Disease. *Cell Host Microbe* **28**, 273-284.e6 (2020).

52. Niepel, D., Klag, T., Malek, N. P. & Wehkamp, J. Practical guidance for the management of iron deficiency in patients with inflammatory bowel disease. *Ther. Adv. Gastroenterol.* **11**, 1756284818769074 (2018).

53. Constante, M., Fragoso, G., Lupien-Meilleur, J., Calvé, A. & Santos, M. M. Iron Supplements Modulate Colon Microbiota Composition and Potentiate the Protective Effects of Probiotics in Dextran Sodium Sulfate-induced Colitis. *Inflamm. Bowel Dis.* **23**, 753–766 (2017).

54. Lee, T., Clavel, T., Smirnov, K., Schmidt, A., Lagkouvardos, I., Walker, A., Lucio, M., Michalke, B., Schmitt-Kopplin, P., Fedorak, R. & Haller, D. Oral versus intravenous iron replacement therapy distinctly alters the gut microbiota and metabolome in patients with IBD. *Gut* **66**, 863–871 (2017).

55. La Carpia, F., Wojczyk, B. S., Annavajhala, M. K., Rebbaa, A., Culp-Hill, R., D'Alessandro, A., Freedberg, D. E., Uhlemann, A.-C. & Hod, E. A. Transfusional iron overload and intravenous iron infusions modify the mouse gut microbiota similarly to dietary iron. *Npj Biofilms Microbiomes* **5**, 1–11 (2019).

56. Al Nabhani, Z., Dulauroy, S., Lécuyer, E., Polomack, B., Campagne, P., Berard, M. & Eberl, G. Excess calorie intake early in life increases susceptibility to colitis in adulthood. *Nat. Metab.* **1**, 1101–1109 (2019).

57. Zhang, J., Jiao, Y., Hou, S., Tian, T., Yuan, Q., Hao, H., Wu, Z. & Bao, X. S100A4 contributes to colitis development by increasing the adherence of Citrobacter rodentium in intestinal epithelial cells. *Sci. Rep.* **7**, 12099 (2017).

58. Wang, Y., Tao, H., Huang, H., Xiao, Y., Wu, X., Li, M., Shen, J., Xiao, Z., Zhao, Y., Du, F., Ji, H., Chen, Y., Cho, C. H., Wang, Y., Wang, S. & Wu, X. The dietary

supplement *Rhodiola crenulata* extract alleviates dextran sulfate sodium-induced colitis in mice through anti-inflammation, mediating gut barrier integrity and reshaping the gut microbiome. *Food Funct.* **12**, 3142–3158 (2021).

59. Roulis, M. & Flavell, R. A. Fibroblasts and myofibroblasts of the intestinal lamina propria in physiology and disease. *Differentiation* **92**, 116–131 (2016).

60. Rieder, F. & Fiocchi, C. Intestinal fibrosis in inflammatory bowel disease — Current knowledge and future perspectives. *J. Crohns Colitis* **2**, 279–290 (2008).

61. Gore, R. M. Colonic contour changes in chronic ulcerative colitis: reappraisal of some old concepts. *Am. J. Roentgenol.* **158**, 59–61 (1992).

62. Xiang, J., Zhang, Y., Bao, D., Cao, N., Zhang, X., Li, P., Qiu, S., Guo, J., He, D., Li, B., Yao, L. & Liu, H. c-Abl regulates gastrointestinal muscularis propria homeostasis via ERKs. *Sci. Rep.* **7**, 3563 (2017).

63. Tajima, T., Murata, T., Aritake, K., Urade, Y., Michishita, M., Matsuoka, T., Narumiya, S., Ozaki, H. & Hori, M. EP_2 and EP_4 receptors on muscularis resident macrophages mediate LPS-induced intestinal dysmotility via iNOS upregulation through cAMP/ERK signals. *Am. J. Physiol.-Gastrointest. Liver Physiol.* **302**, G524–G534 (2012).

64. Li, Z. S. Physiological Modulation of Intestinal Motility by Enteric Dopaminergic Neurons and the D2 Receptor: Analysis of Dopamine Receptor Expression, Location, Development, and Function in Wild-Type and Knock-Out Mice. *J. Neurosci.* **26**, 2798–2807 (2006).

65. Li, Z., Chalazonitis, A., Huang, Y. -y., Mann, J. J., Margolis, K. G., Yang, Q. M., Kim, D. O., Cote, F., Mallet, J. & Gershon, M. D. Essential Roles of Enteric Neuronal Serotonin in Gastrointestinal Motility and the Development/Survival of Enteric Dopaminergic Neurons. *J. Neurosci.* **31**, 8998–9009 (2011).

66. Muller, P. A., Koscsó, B., Rajani, G. M., Stevanovic, K., Berres, M.-L., Hashimoto, D., Mortha, A., Leboeuf, M., Li, X.-M., Mucida, D., Stanley, E. R., Dahan, S., Margolis, K. G., Gershon, M. D., Merad, M. & Bogunovic, M. Crosstalk between Muscularis Macrophages and Enteric Neurons Regulates Gastrointestinal Motility. *Cell* **158**, 300–313 (2014).

67. Moynes, D. M., Lucas, G. H., Beyak, M. J. & Lomax, A. E. Effects of Inflammation on the Innervation of the Colon. *Toxicol. Pathol.* **42**, 111–117 (2014).

68. Chen, J. J., Li, Z., Pan, H., Murphy, D. L., Tamir, H., Koepsell, H. & Gershon, M. D. Maintenance of Serotonin in the Intestinal Mucosa and Ganglia of Mice that Lack the High-Affinity Serotonin Transporter: Abnormal Intestinal Motility and the Expression of Cation Transporters. *J. Neurosci.* **21**, 6348–6361 (2001).

69. O'Hara, J. R., Skinn, A. C., MacNaughton, W. K., Sherman, P. M. & Sharkey, K. A. Consequences of Citrobacter rodentium infection on enteroendocrine cells and the enteric nervous system in the mouse colon. *Cell. Microbiol.* **8**, 646–660 (2006).

70. Eder, P., Adler, M., Dobrowolska, A., Kamhieh-Milz, J. & Witowski, J. The Role of Adipose Tissue in the Pathogenesis and Therapeutic Outcomes of Inflammatory Bowel Disease. *Cells* **8**, 628 (2019).

71. Thaiss, C. A., Levy, M., Grosheva, I., Zheng, D., Soffer, E., Blacher, E., Braverman, S., Tengeler, A. C., Barak, O., Elazar, M., Ben-Zeev, R., Lehavi-Regev, D., Katz, M. N., Pevsner-Fischer, M., Gertler, A., Halpern, Z., Harmelin, A., Aamar, S., Serradas, P., Grosfeld, A., Shapiro, H., Geiger, B. & Elinav, E. Hyperglycemia drives intestinal barrier dysfunction and risk for enteric infection. *Science* **359**, 1376–1383 (2018).

72. Ananthakrishnan, A. N., Khalili, H., Konijeti, G. G., Higuchi, L. M., de Silva, P., Fuchs, C. S., Willett, W. C., Richter, J. M. & Chan, A. T. Long-term intake of dietary fat and risk of ulcerative colitis and Crohn's disease. *Gut* **63**, 776–784 (2014).

73. Gonçalves, P., Magro, F. & Martel, F. Metabolic Inflammation in Inflammatory Bowel Disease: Crosstalk Between Adipose Tissue and Bowel. *Inflamm. Bowel Dis.* **21**, 453–467 (2015).

74. Kwon, J., Lee, C., Heo, S., Kim, B. & Hyun, C.-K. DSS-induced colitis is associated with adipose tissue dysfunction and disrupted hepatic lipid metabolism leading to hepatosteatosis and dyslipidemia in mice. *Sci. Rep.* **11**, 5283 (2021).

75. Romacho, T., Elsen, M., Röhrborn, D. & Eckel, J. Adipose tissue and its role in organ crosstalk. *Acta Physiol.* **210**, 733–753 (2014).

76. Burhans, M. S., Hagman, D. K., Kuzma, J. N., Schmidt, K. A. & Kratz, M. Contribution of adipose tissue inflammation to the development of type 2 diabetes mellitus. *Compr. Physiol.* **9**, 1–58 (2018).

77. Chait, A. & den Hartigh, L. J. Adipose Tissue Distribution, Inflammation and Its Metabolic Consequences, Including Diabetes and Cardiovascular Disease. *Front. Cardiovasc. Med.* **0**, (2020).

78. Lundgren, P. & Thaiss, C. A. The microbiome-adipose tissue axis in systemic metabolism. *Am. J. Physiol.-Gastrointest. Liver Physiol.* **318**, G717–G724 (2020).

79. Rosendo-Silva, D. & Matafome, P. Gut–adipose tissue crosstalk: A bridge to novel therapeutic targets in metabolic syndrome? *Obes. Rev.* **22**, (2021).

80. Tanowitz, H. B., Scherer, P. E., Mota, M. M. & Figueiredo, L. M. Adipose Tissue: A Safe Haven for Parasites? *Trends Parasitol.* **33**, 276–284 (2017).

81. Troha, K. & Ayres, J. S. Metabolic Adaptations to Infections at the Organismal Level. *Trends Immunol.* **41**, 113–125 (2020).

82. Palaferri Schieber, A. M., Lee, Y. M., Chang, M. W., Leblanc, M., Collins, B., Downes, M., Evans, R. M. & Ayres, J. S. Disease tolerance mediated by commensal E. coli via inflammasome and IGF-1 signaling. *Science* **350**, 558–563 (2015).

83. Ha, C. W. Y., Martin, A., Sepich-Poore, G. D., Shi, B., Wang, Y., Gouin, K., Humphrey, G., Sanders, K., Ratnayake, Y., Chan, K. S. L., Hendrick, G., Caldera, J. R., Arias, C., Moskowitz, J. E., Ho Sui, S. J., Yang, S., Underhill, D., Brady, M. J., Knott, S., Kaihara, K., Steinbaugh, M. J., Li, H., McGovern, D. P. B., Knight, R., Fleshner, P. & Devkota, S. Translocation of Viable Gut Microbiota to Mesenteric Adipose Drives Formation of Creeping Fat in Humans. *Cell* **183**, 666-683.e17 (2020).

84. Peyrin-Biroulet, L., Chamaillard, M., Gonzalez, F., Beclin, E., Decourcelle, C., Antunes, L., Gay, J., Neut, C., Colombel, J. & Desreumaux, P. Mesenteric fat in Crohn's disease: a pathogenetic hallmark or an innocent bystander? *Gut* **56**, 577–583 (2007).

85. Zulian, A., Cancello, R., Ruocco, C., Gentilini, D., Di Blasio, A. M., Danelli, P., Micheletto, G., Cesana, E. & Invitti, C. Differences in Visceral Fat and Fat Bacterial Colonization between Ulcerative Colitis and Crohn's Disease. An In Vivo and In Vitro Study. *PLoS ONE* **8**, e78495 (2013).

86. Fonseca, D. M. da, Hand, T. W., Han, S.-J., Gerner, M. Y., Zaretsky, A. G., Byrd, A. L., Harrison, O. J., Ortiz, A. M., Quinones, M., Trinchieri, G., Brenchley, J. M., Brodsky, I. E., Germain, R. N., Randolph, G. J. & Belkaid, Y. Microbiota-Dependent Sequelae of Acute Infection Compromise Tissue-Specific Immunity. *Cell* **163**, 354–366 (2015).

87. Kredel, L. I. & Siegmund, B. Adipose-Tissue and Intestinal Inflammation – Visceral Obesity and Creeping Fat. *Front. Immunol.* **5**, (2014).

88. Zhang, Z., Funcke, J.-B., Zi, Z., Zhao, S., Straub, L. G., Zhu, Y., Zhu, Q., Crewe, C., An, Y. A., Chen, S., Li, N., Wang, M., Ghaben, A. L., Lee, C., Gautron, L., Engelking, L. J., Raj, P., Deng, Y., Gordillo, R., Kusminski, C. M. & Scherer, P. E. Adipocyte iron levels impinge on a fat-gut crosstalk to regulate intestinal lipid absorption and mediate protection from obesity. *Cell Metab.* **33**, 1624-1639.e9 (2021).

89. Huang, Y., Qi, H., Zhang, Z., Wang, E., Yun, H., Yan, H., Su, X., Liu, Y., Tang, Z., Gao, Y., Shang, W., Zhou, J., Wang, T., Che, Y., Zhang, Y. & Yang, R. Gut REG3γ-Associated Lactobacillus Induces Anti-inflammatory Macrophages to Maintain Adipose Tissue Homeostasis. *Front. Immunol.* **8**, 1063 (2017).

90. Singh, U. P., Singh, N. P., Guan, H., Busbee, B., Price, R. L., Taub, D. D., Mishra, M. K., Fayad, R., Nagarkatti, M. & Nagarkatti, P. S. Leptin antagonist ameliorates chronic colitis in IL-10−/− mice. *Immunobiology* **218**, 1439–1451 (2013).

91. Fazolini, N. P., Cruz, A. L., Werneck, M. B., Viola, J. P., Maya-Monteiro, C. M. & Bozza, P. T. Leptin activation of mTOR pathway in intestinal epithelial cell triggers lipid droplet formation, cytokine production and increased cell proliferation. *Cell Cycle* **14**, 2667–2676 (2015).

92. Ziegler, J. F., Böttcher, C., Letizia, M., Yerinde, C., Wu, H., Freise, I., Rodriguez-Sillke, Y., Stoyanova, A. K., Kreis, M. E., Asbach, P., Kunkel, D., Priller, J., Anagnostopoulos, I., Kühl, A. A., Miehle, K., Stumvoll, M., Tran, F., Fredrich, B., Forster, M., Franke, A., Bojarski, C., Glauben, R., Löscher, B.-S., Siegmund, B. & Weidinger, C. Leptin induces TNFα-dependent inflammation in acquired generalized lipodystrophy and combined Crohn's disease. *Nat. Commun.* **10**, 5629 (2019).

93. de Carvalho, L. G. F., Lima, W. G., Coelho, L. G. V., Cardoso, V. N. & Fernandes, S. O. A. Circulating Leptin Levels as a Potential Biomarker in Inflammatory Bowel Diseases: A Systematic Review and Meta-Analysis. *Inflamm. Bowel Dis.* **27**, 169–181 (2021).

94. Gao, Y., Li, Z., Gabrielsen, J. S., Simcox, J. A., Lee, S., Jones, D., Cooksey, B., Stoddard, G., Cefalu, W. T. & McClain, D. A. Adipocyte iron regulates leptin and food intake. *J. Clin. Invest.* **125**, 3681–3691 (2015).

95. Dongiovanni, P., Ruscica, M., Rametta, R., Recalcati, S., Steffani, L., Gatti, S., Girelli, D., Cairo, G., Magni, P., Fargion, S. & Valenti, L. Dietary Iron Overload Induces Visceral Adipose Tissue Insulin Resistance. *Am. J. Pathol.* **182**, 2254–2263 (2013).

96. Ayres, J. S. Immunometabolism of infections. *Nat. Rev. Immunol.* **20**, 79–80 (2020).

97. Dobner, J. & Kaser, S. Body mass index and the risk of infection - from underweight to obesity. *Clin. Microbiol. Infect.* **24**, 24–28 (2018).

98. Zhao, X. & Karpac, J. Glutamate metabolism directs energetic trade-offs to shape host-pathogen susceptibility in Drosophila. *Cell Metab.* **33**, 2428-2444.e8 (2021).

99. Nhan, J. D., Turner, C. D., Anderson, S. M., Yen, C.-A., Dalton, H. M., Cheesman, H. K., Ruter, D. L., Uma Naresh, N., Haynes, C. M., Soukas, A. A., Pukkila-Worley, R. & Curran, S. P. Redirection of SKN-1 abates the negative metabolic outcomes of a perceived pathogen infection. *Proc. Natl. Acad. Sci. U. S. A.* **116**, 22322–22330 (2019).

Figure 3.3.1 Dietary iron supplementation protects mice from *C. rodentium*-induced colitis

(A) Six-week old C57BL/6 males were provided control iron diet (CID) or 2% carbonyl iron diet (IRD) and infected with 2.9-4.75 x10^8 CFU *C. rodentium* by oral gavage or fed diet only. **(B)** Representative images of dissected cecum and colons from *C.r.*-infected and uninfected mice fed CID or IRD for 8 days (metric ruler for scale) and **(C)** corresponding colon lengths and **(D)** spleen mass normalized to total body mass from uninfected and *C.r.*-infected mice on CID or IRD for 6-8 days. Data shown represents four pooled independent experiments (n= 14-22 mice per group). **(E)** Representative images of H/E-stained colon sections and **(F)** corresponding total pathology scores of colonic mucosal damage from uninfected and *C.r.*-infected mice fed CID or IRD for 6 days. Data shown represents two pooled independent experiments (n=4-5 mice per group) (**G)** Representative images of H/E-stained distal muscularis and **(H)** corresponding thickness values of distal muscularis layer from uninfected and *C.r.*-infected mice fed CID or IRD for 6 days. Data shown represents two pooled independent experiments (n=4-5 mice per group). Yellow bar scale 100 μm. **(I)** Percent original weight of *C.r.* infected or uninfected mice fed CID or IRD. Data shown represents four pooled independent experiments (n=14-22 mice per group). Blue asterisks indicate statistical comparison between CID and CID + *C.r.* Gold asterisks indicate statistical comparison between IRD and IRD + *C.r.* Data represent mean ±SEM. **P*<0.05, ***P*<0.01, ****P*<0.001, *****P*<0.0001. Related to **Supplemental Figure 3.3.1**

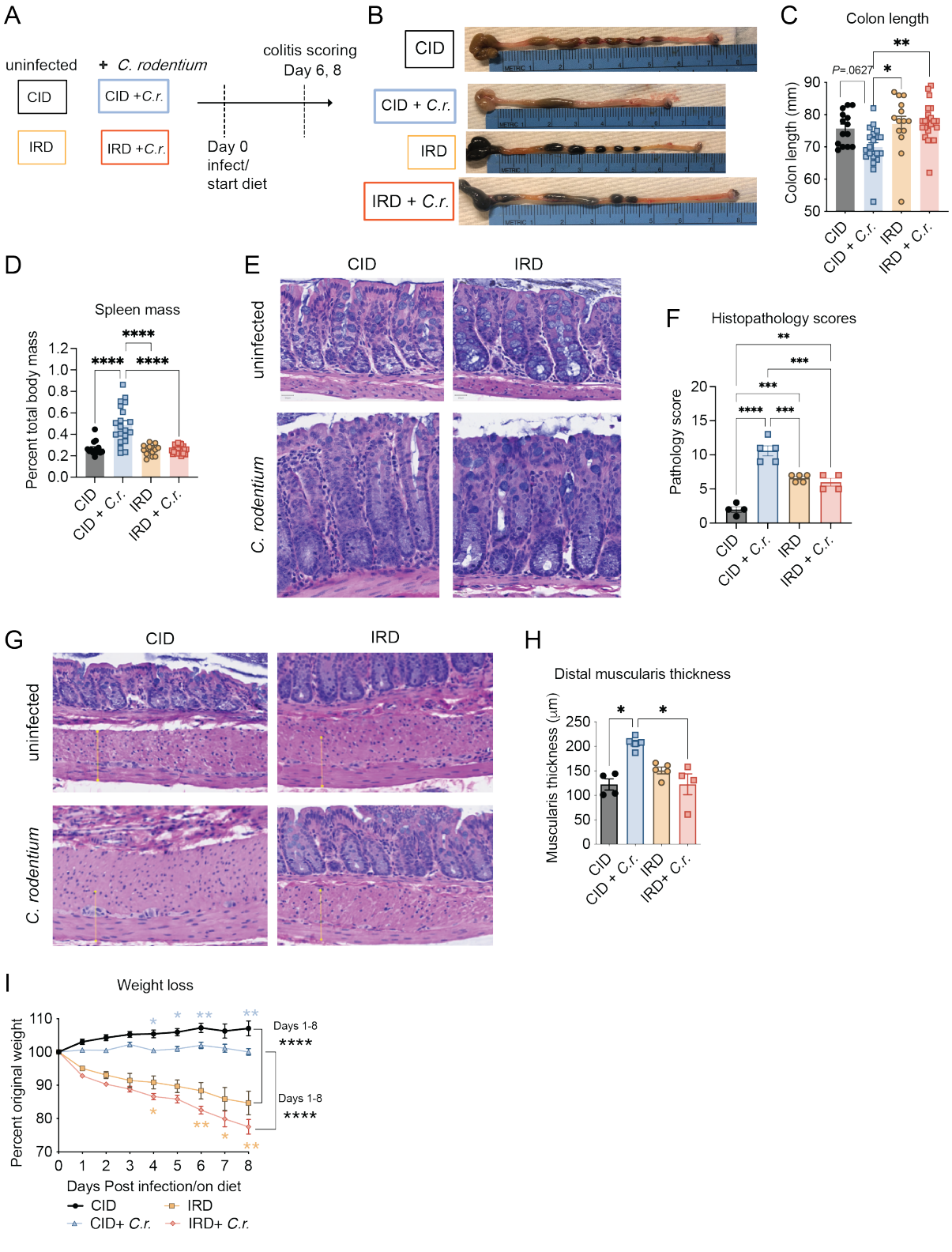
A
uninfected
+ C. rodentium
CID
CID +C.r.
IRD
IRD +C.r.
colitis scoring
Day 6, 8
Day 0
infect/
start diet
B
CID
CID + C.r.
IRD
IRD + C.r.
C
Colon length
P=.0627
Colon length (mm)
CID
CID + C.r.
IRD
IRD + C.r.
D
Spleen mass
Percent total body mass
E
CID
IRD
uninfected
C. rodentium
F
Histopathology scores
Pathology score
G
CID
IRD
uninfected
C. rodentium
H
Distal muscularis thickness
Muscularis thickness (μm)
I
Weight loss
Percent original weight
Days 1-8
Days 1-8
Days Post infection/on diet
CID
IRD
CID+ C.r.
IRD+ C.r.

Figure 3.3.2 Dietary iron promotes resistance defenses by disrupting *C. rodentium* pathogenesis

(A) Six-week old C57BL/6 males were provided control iron diet(CID) or 2% carbonyl iron diet (IRD) and infected with 2.9-4.75 x10^8 CFU *C. rodentium* by oral gavage or fed diets only. **(B-C)** Colony forming units (CFU) were quantified by plating serially diluted homogenized samples on MacConkey agar. **(B)** *C.r.* fecal shedding from *C.r.*-infected mice fed CID or IRD over infection course. Data shown represents four pooled independent experiments (n=8-18 mice per group per day). **(C)** *C.r.* pathogen loads from homogenized organs harvested on dpi 6-8 from *C.r.*-infected mice fed CID or IRD. Dotted black lines represents limit of detection. Data shown represents one experiment (dpi 8 liver, SI, Colon) and three pooled independent experiments (dpi 6,8 Cecum) (n=5-17 mice per group per organ). **(D-G)** Gene expression analyses in proximal and distal colons from *C.r.*-infected and uninfected mice fed CID or IRD for 8 days: (**D)** *C.r.*-specific sigma factor (*rpoD);* **(E)** locus of enterocyte effacement (LEE) virulence genes (*map, tir,* espA) and non-LEE (*espI*) encoded virulence gene; **(F)** host innate inflammatory signaling genes and **(G)** antimicrobial peptide genes. Expression fold change was determined by normalizing gene expression to expression of host *Rps17* and subsequently normalizing to the lowest *gene:Rps17* value within each group. Data shown represents one independent experiment (n=5 per group). Data represent mean ±SEM. **P*<0.05, ***P*<0.01, ****P*<0.001, *****P*<0.0001. Related to **Supplemental Figure 3.3.2**

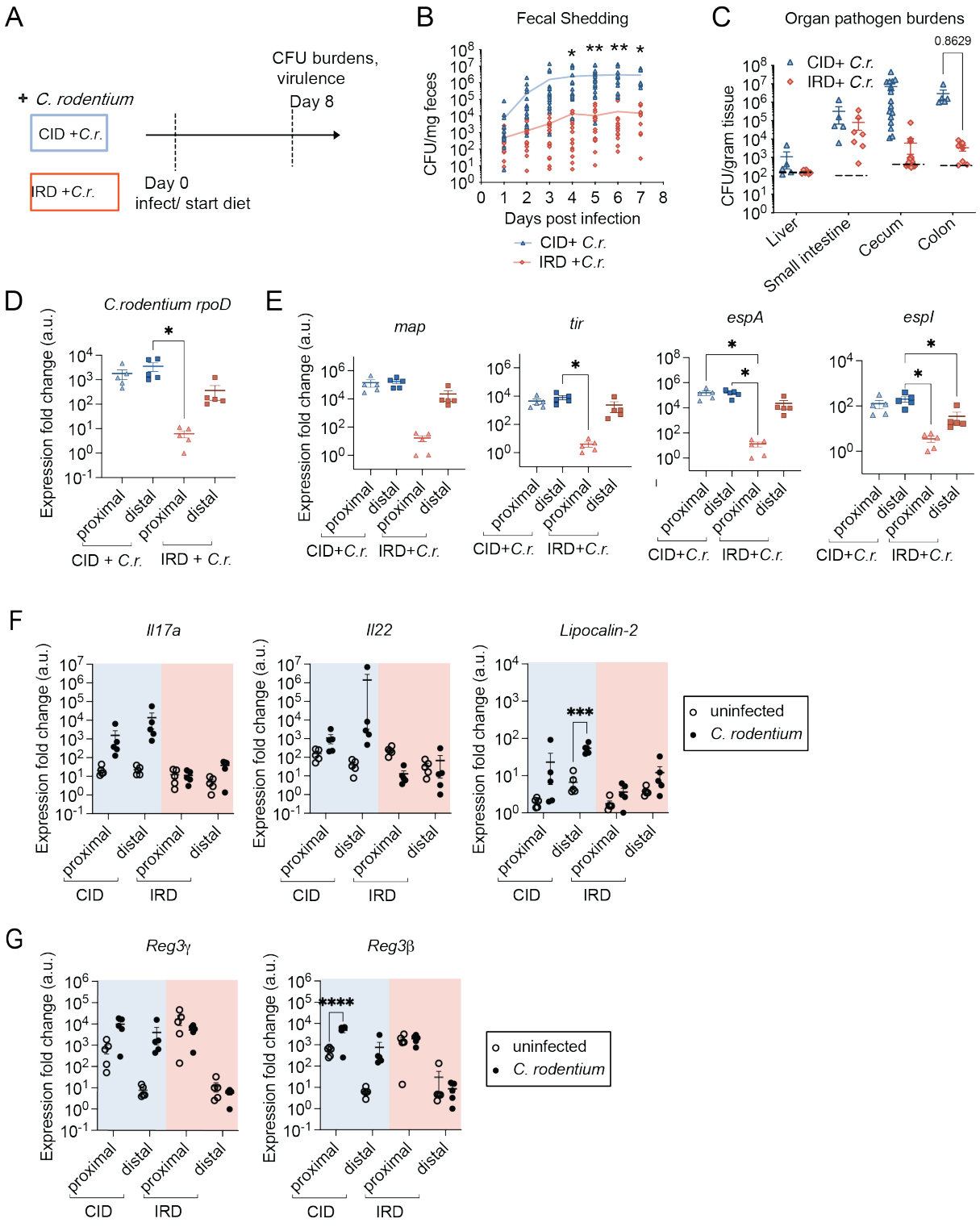
A
+ C. rodentium
CID +C.r.
IRD +C.r.
Day 0
infect/ start diet
CFU burdens,
virulence
Day 8
B
Fecal Shedding
CFU/mg feces
Days post infection
CID+ C.r.
IRD +C.r.
C
Organ pathogen burdens
0.8629
CID+ C.r.
IRD+ C.r.
CFU/gram tissue
Liver
Small intestine
Cecum
Colon
D
C.rodentium rpoD
Expression fold change (a.u.)
proximal
distal
CID + C.r.
IRD + C.r.
E
map
tir
espA
espI
CID+C.r.
IRD+C.r.
F
Il17a
Il22
Lipocalin-2
CID
IRD
uninfected
C. rodentium
G
Reg3γ
Reg3β

Figure 3.3.3 Dietary iron surplus induces lipolysis and fat wasting during *C. rodentium* infection

(A) Six-week old C57BL/6 males were provided control iron diet (CID) or 2% carbonyl iron diet (IRD) and infected with 4.3-4.75x10^8 CFU *C. rodentium* by oral gavage or fed diet only for 8 days. Food consumption and body mass was measured daily. **(B)** Fat composition of *C.r.*-infected and uninfected mice fed CID or IRD for 8 days. Fat mass was measured using Echo MRI and normalized to original body mass. Data shown represents two pooled independent experiments. (n=9-11 mice per group) **(C-E)** Tissue masses of white adipose tissue (WAT) depots: **(C)** inguinal (IWAT) **(D)** gonadal (GWAT) and **(E)** mesenteric (MWAT) from uninfected or *C.r.*-infected mice fed CID or IRD for 8 days**.** Data shown represents one independent experiment. (n=4-5 mice per group) **(F)** Lean composition of *C.r.*-infected and uninfected mice fed CID or IRD for 8 days. Lean mass was measured using Echo MRI and normalized to original body mass. Data shown represents two pooled independent experiments. (n=9-10 mice per group) **(G)** Muscle masses from hindlimb of uninfected or *C.r.*-infected mice fed CID or IRD for 8 days (Quad- quadricep; TA-tibialis anterior; Gastro-gastrocnemius). Data shown represents one independent experiment. (n=4-7 mice per group) **(H-I)** *Ex vivo* lipolysis assay measuring glycerol and free fatty acids (FFA) released from **(H)** IWAT **(I)** and GWAT of uninfected or *C.r.*-infected mice fed CID or IRD for 8 days**.** Data shown represents one independent experiment (n=4-5 mice per group). **(j)** Serum FFA and glycerol levels from uninfected or *C.r.*-infected mice fed CID or IRD for 8 days**.** Data shown represents one independent experiment (n=4-5 mice per group). Data represent mean ±SEM; **P*<0.05, ***P*<0.01, ****P*<0.001, *****P*<0.0001.

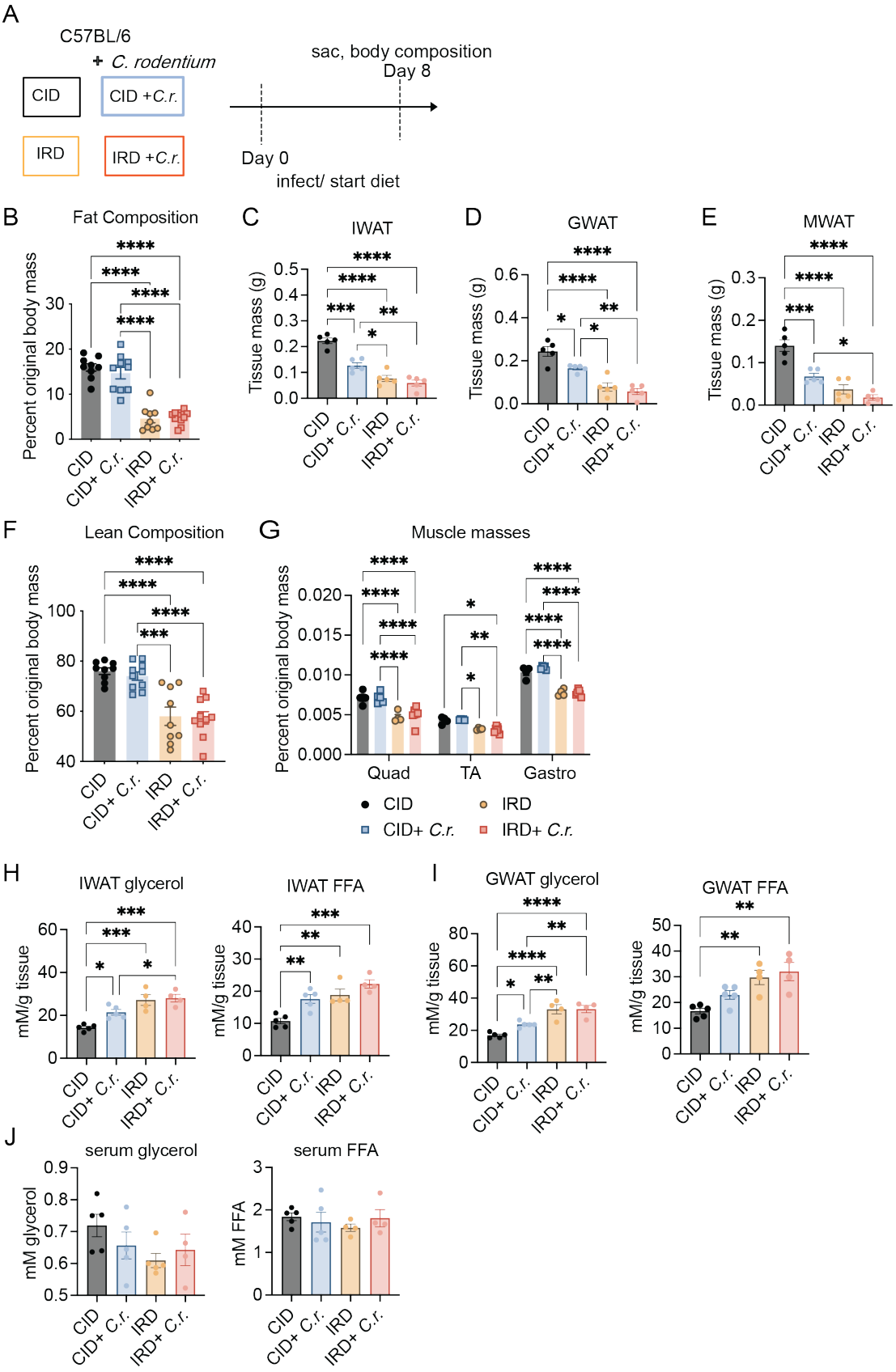
A
C57BL/6
+ C. rodentium
CID
CID +C.r.
IRD
IRD +C.r.
sac, body composition
Day 8
Day 0
infect/ start diet
B
Fat Composition
Percent original body mass
C
IWAT
Tissue mass (g)
D
GWAT
Tissue mass (g)
E
MWAT
Tissue mass (g)
CID
CID+ C.r.
IRD
IRD+ C.r.
F
Lean Composition
Percent original body mass
G
Muscle masses
Percent original body mass
Quad
TA
Gastro
CID
CID+ C.r.
IRD
IRD+ C.r.
H
IWAT glycerol
IWAT FFA
mM/g tissue
I
GWAT glycerol
GWAT FFA
mM/g tissue
J
serum glycerol
mM glycerol
serum FFA
mM FFA

Figure 3.3.4 Dietary iron-induced fat wasting, lipolysis and lipid utilization are dependent on fat-specific ATGL activity

(A) Littermate *Pnpla2* x Fabp4 cre- ($Pnpla2^{WT}$) and *Pnpla2* x Fabp4 cre+ ($Pnpla2^{WAT\ KO}$) males between six and eight-weeks old were provided control iron diet (CID) or 2% carbonyl iron diet (IRD) and infected with 3.58-6.3x10^8 CFU *Citrobacter rodentium* by oral gavage. Food consumption and body mass was measured daily. **(B)** Percent original weight over nine day infection period of $Pnpla2^{WT}$ and $Pnpla2^{WAT\ KO}$ mice fed CID or IRD. Black asterisks indicate comparisons between $Pnpla2^{WT}$ fed CID or IRD. Orange asterisks indicate comparisons between $Pnpla2^{WAT\ KO}$ fed CID or IRD. Data shown represent three pooled independent experiments (n=4-12 mice per group) **(C)** Fat composition using Echo MRI of *C.r.*-infected $Pnpla2^{WT}$ and $Pnpla2^{WAT\ KO}$ mice fed CID or IRD on dpi 9. Fat mass was normalized to original body mass. Data shown represents three pooled independent experiments (n=4-12 mice per group). **(D-F)** Tissue masses of **(D)** IWAT **(E)** GWAT and **(F)** MWAT from *C.r.*-infected $Pnpla2^{WT}$ and $Pnpla2^{WAT\ KO}$ mice fed CID or IRD on dpi 9**.** Data shown represents three pooled independent experiments (n=4-12 mice per group). **(G)** Lean composition using Echo MRI of *C.r.*-infected $Pnpla2^{WT}$ and $Pnpla2^{WAT\ KO}$ mice fed CID or IRD on dpi 9. Lean mass was normalized to original body mass. Data shown represents three pooled independent experiments (n=4-12 mice per group). **(H-I)** *Ex vivo* lipolysis assay measuring glycerol and free fatty acids (FFA) released from **(H)** IWAT **(I)** and GWAT of *C.r.*-infected $Pnpla2^{WT}$ and $Pnpla2^{WAT\ KO}$ mice fed CID or IRD on dpi 6**.** Data shown represents two pooled independent experiments (n=4-8 mice per group). **(J-K)** $Pnpla2^{WT}$ and $Pnpla2^{WAT\ KO}$ males between six and eight-weeks old were housed in comprehensive laboratory animal monitoring system (CLAMS) metabolic cages for 8 days. Mice were provided CID or IRD and infected with 3.58x10^8 CFU *C. rodentium* by oral gavage following a two day acclimation period. Food consumption and body mass was measured daily. **(J)** Respiratory exchange ratio (RER) and corresponding **(K)** area under the curve (AUC) analysis of RER for infection period (dpi 0-6). Data shown represents one independent experiment (n=4 mice per group). All CLAMS data plotted in zeitgeber time. White/black boxes on X axis represent 12-hr light/dark cycles of 24-hr day. AUC of CLAMS analyses taken from total average values per mouse. **(I)** Serum glycerol and FFA levels from *C.r.*-infected $Pnpla2^{WT}$ and $Pnpla2^{WAT\ KO}$ mice fed CID or IRD on dpi 9**.** Data shown represents three pooled independent experiments (n=4-12 mice per group). Data represent mean ±SEM. **P*<0.05, ***P*<0.01, ****P*<0.001, *****P*<0.0001. Related to **Supplemental Figure 3.3.4**

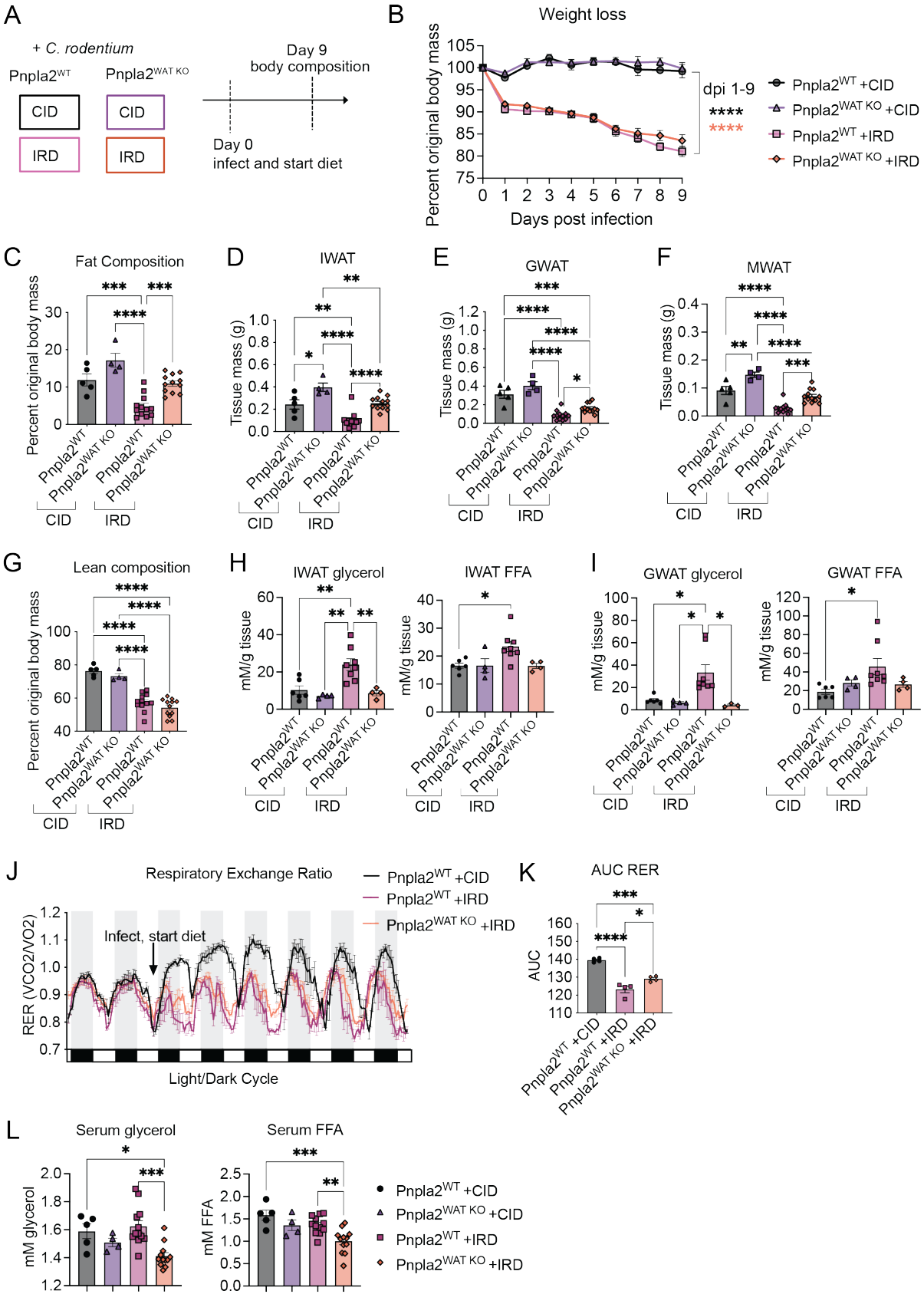
A
+ C. rodentium
Pnpla2WT
Pnpla2WAT KO
CID
CID
IRD
IRD
Day 9
body composition
Day 0
infect and start diet
B
Weight loss
Percent original body mass
Days post infection
dpi 1-9
****
****
Pnpla2WT +CID
Pnpla2WAT KO +CID
Pnpla2WT +IRD
Pnpla2WAT KO +IRD
C
Fat Composition
Percent original body mass
D
IWAT
Tissue mass (g)
E
GWAT
Tissue mass (g)
F
MWAT
Tissue mass (g)
CID
IRD
G
Lean composition
Percent original body mass
H
IWAT glycerol
IWAT FFA
mM/g tissue
I
GWAT glycerol
GWAT FFA
mM/g tissue
J
Respiratory Exchange Ratio
Infect, start diet
RER (VCO2/VO2)
Light/Dark Cycle
K
AUC RER
AUC
L
Serum glycerol
mM glycerol
Serum FFA
mM FFA

Figure 3.3.5 Dietary iron-induced lipolysis and fat wasting are dispensable for promoting resistance defenses against *C. rodentium*

(A) Littermate *Pnpla2* x Fabp4 cre- ($Pnpla2^{WT}$) and *Pnpla2* x Fabp4 cre+ ($Pnpla2^{WAT\ KO}$) males between six and eight-weeks old were provided control iron diet (CID) or 2% carbonyl iron diet (IRD) and infected with 3.58-6.3x10^8 CFU *C. rodentium* by oral gavage. **(B-C)** Colony forming units (CFU) were quantified by plating serially diluted homogenized samples on MacConkey agar. **(B)** *C.r.* fecal from *C.r.*-infected $Pnpla2^{WT}$ and $Pnpla2^{WAT\ KO}$ mice fed CID or IRD and CFU was normalized to pellet mass. Data shown represents two pooled independent experiments (n=4-8 mice per group). **(C)** *C.r.* pathogen loads from homogenized organs harvested on dpi 6 from *C.r.*-infected $Pnpla2^{WT}$ and $Pnpla2^{WAT\ KO}$ mice fed CID or IRD. Data shown represents one independent experiment (n=4 mice per group). **(D-F)** RNA was extracted from colons harvested on **(D)** dpi 6 or **(E,F,G)** dpi 9 and used for gene expression analyses via quantitative real time PCR. **(D)** Relative expression of *C.r.*-specific sigma factor (*rpoD)* in proximal and distal colon of infected $Pnpla2^{WT}$ and $Pnpla2^{WAT\ KO}$ mice fed CID or IRD on dpi 6. Gene expression was normalized to host *Rps17* expression. Data shown represents two pooled independent experiments (n=3-4 mice per group). **(E)** Expression fold change of *C. rodentium* locus of enterocyte effacement (LEE) virulence genes (*map, tir,* espA) and non-LEE (*espI*) encoded virulence gene and **(F)** host innate inflammatory signaling genes and **(G)** antimicrobial peptide genes in colons of infected $Pnpla2^{WT}$ and $Pnpla2^{WAT\ KO}$ mice fed CID or IRD on dpi 9. Expression fold change was determined by normalizing gene expression to expression of host *Rps17* and subsequently normalizing to the lowest *gene:Rps17* value within each group. Data shown represents two pooled independent experiments (n=4-8 mice per group). Data represent mean ±SEM. **P*<0.05, ***P*<0.01, ****P*<0.001, *****P*<0.0001. Related to **Supplemental Figure 3.3.5 and 3.3.6.**

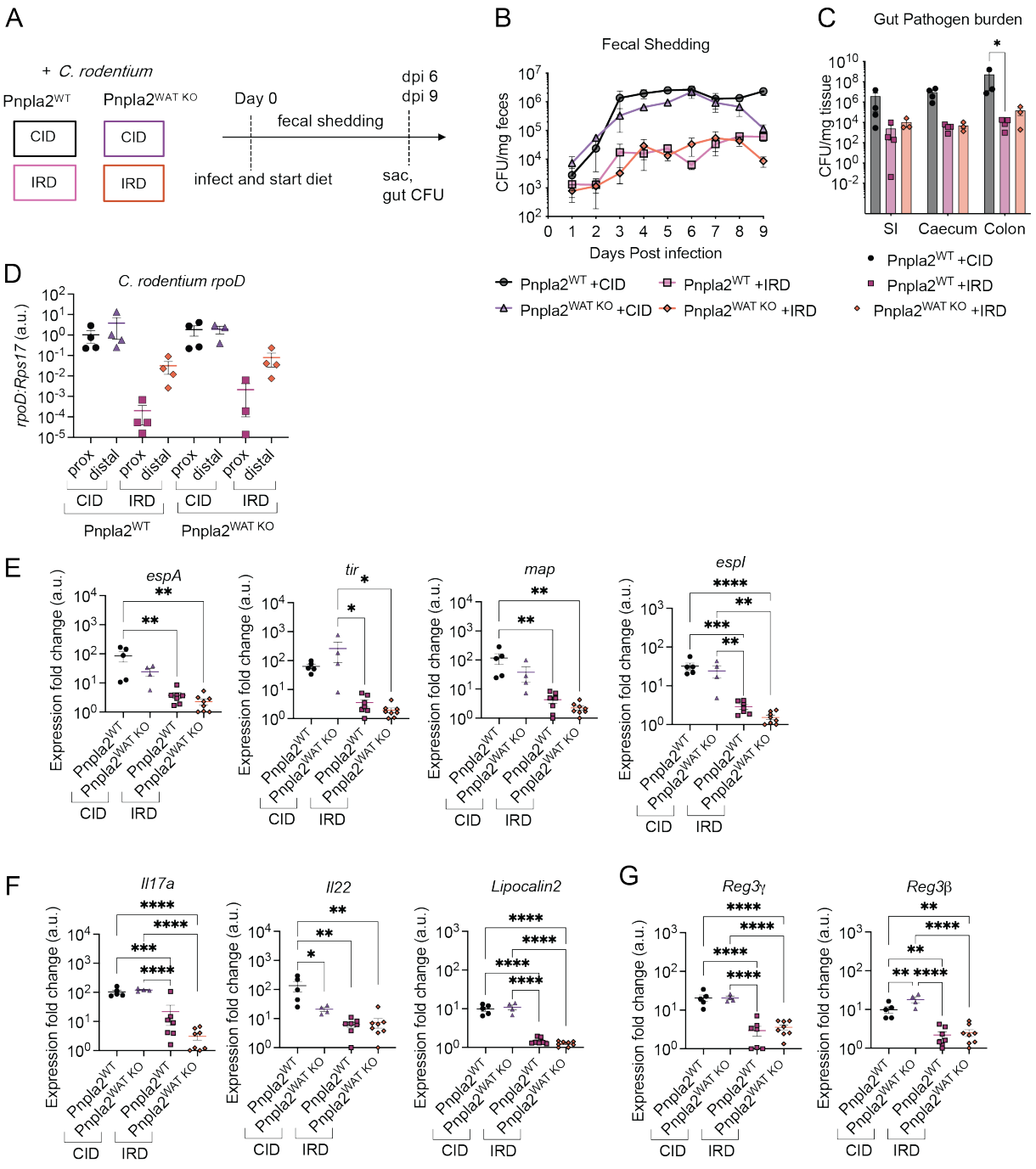
A
+ C. rodentium
Pnpla2WT
Pnpla2WAT KO
CID
IRD
Day 0
fecal shedding
dpi 6
dpi 9
infect and start diet
sac, gut CFU
B
Fecal Shedding
CFU/mg feces
Days Post infection
Pnpla2WT +CID
Pnpla2WT +IRD
Pnpla2WAT KO +CID
Pnpla2WAT KO +IRD
C
Gut Pathogen burden
CFU/mg tissue
SI
Caecum
Colon
D
C. rodentium rpoD
rpoD:Rps17 (a.u.)
prox
distal
E
espA
tir
map
espI
Expression fold change (a.u.)
F
Il17a
Il22
Lipocalin2
G
Reg3γ
Reg3β

Figure 3.3.6 Iron-induced lipolysis and fat wasting are necessary to prevent *C. rodentium*-induced colon shortening and remodeling

(A) Littermate *Pnpla2* x Fabp4 cre- ($Pnpla2^{WT}$) and *Pnpla2* x Fabp4 cre+ ($Pnpla2^{WAT\ KO}$) males between six and eight-weeks old were provided control iron diet (CID) or 2% carbonyl iron diet (IRD) and infected with 3.68-6.8 $x10^8$ CFU *C. rodentium* by oral gavage. **(B)** Representative images of dissected cecum and colons from *C.r.*-infected $Pnpla2^{WT}$ and $Pnpla2^{WAT\ KO}$ mice fed CID or IRD for 6 days (metric ruler for scale) and **(C-D)** corresponding colon lengths on **(C)** dpi 6 and **(D)** dpi 9. **(E)** Spleen mass of *C.r.*-infected $Pnpla2^{WT}$ and $Pnpla2^{WAT\ KO}$ mice fed CID or IRD for 9 days. Data shown for panel **C** represents five pooled independent experiments (n=4-21 mice per group). Data shown for panel **D** and **E** represents three pooled independent experiments (n=4-12 mice per group). **(F)** Representative images of H/E-stained colon sections and **(G)** corresponding total pathology scores of colonic mucosal damage from *C.r.*-infected $Pnpla2^{WT}$ and $Pnpla2^{WAT\ KO}$ mice fed CID or IRD for 6 days. Data shown represents one independent experiment (n=3-5 mice per group) **(H)** Representative images of H/E-stained distal muscularis and **(I)** corresponding thickness values of distal muscularis layer from *C.r.*-infected $Pnpla2^{WT}$ and $Pnpla2^{WAT\ KO}$ mice fed CID or IRD for 6 days. Data shown represents one independent experiment (n=3-5 mice per group). Data represent mean ±SEM. **P*<0.05, ***P*<0.01, ****P*<0.001, *****P*<0.0001. Related to **Supplemental Figure 3.3.7.**

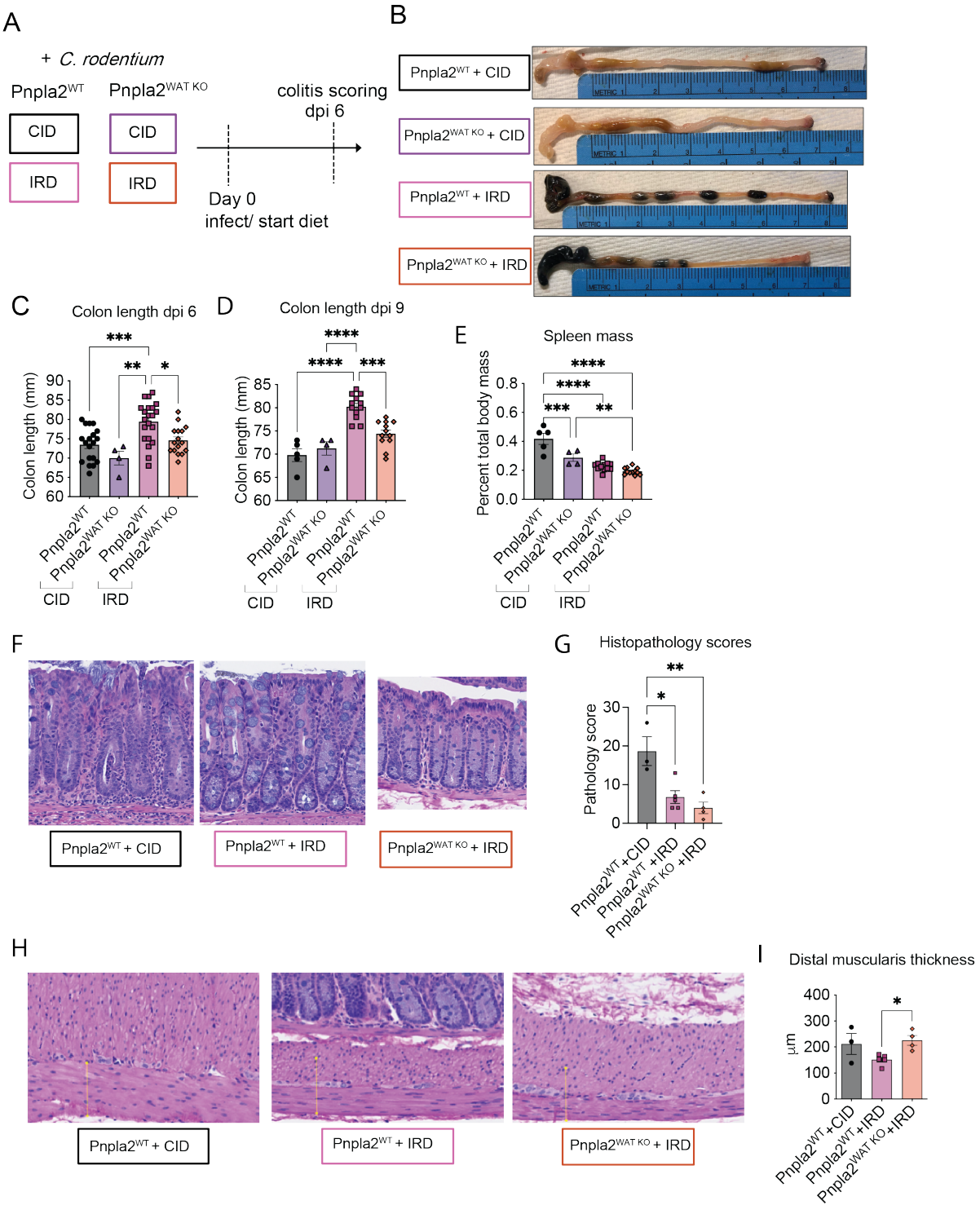
A
+ C. rodentium
Pnpla2WT
Pnpla2WAT KO
CID
IRD
CID
IRD
colitis scoring
dpi 6
Day 0
infect/ start diet
B
Pnpla2WT + CID
Pnpla2WAT KO + CID
Pnpla2WT + IRD
Pnpla2WAT KO + IRD
C
Colon length dpi 6
Colon length (mm)
D
Colon length dpi 9
Colon length (mm)
E
Spleen mass
Percent total body mass
F
Pnpla2WT + CID
Pnpla2WT + IRD
Pnpla2WAT KO + IRD
G
Histopathology scores
Pathology score
Pnpla2WT +CID
Pnpla2WT +IRD
Pnpla2WAT KO +IRD
H
Pnpla2WT + CID
Pnpla2WT + IRD
Pnpla2WAT KO + IRD
I
Distal muscularis thickness
µm
Pnpla2WT +CID
Pnpla2WT +IRD
Pnpla2WAT KO +IRD

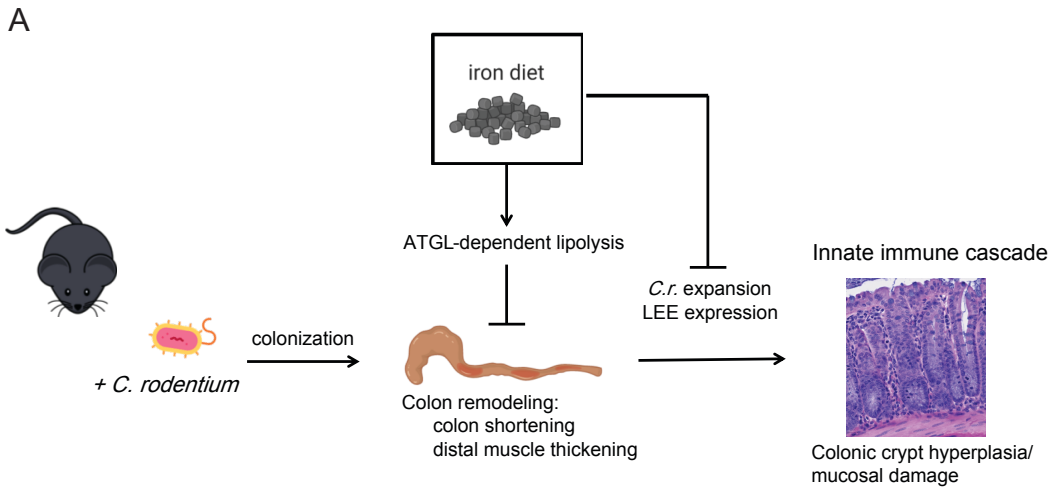

Figure 3.3.7 Iron drives global metabolic rearrangements that uncouple hallmarks of infectious colitis

(A) Dietary iron supplementation protects against colon pathology and non-inflammatory colon remodeling during *C. rodentium* infection through inducing resistance and initiating lipolysis in an ATGL dependent manner to prevent non-inflammatory colon remodeling.

Supplemental Figure 3.3.1 Iron rich diet prevents pathology during *C. rodentium* infection

Six-week old C57BL/6 males were provided control iron diet (CID) or 2% carbonyl iron diet (IRD) and infected with 2.9-4.75 x10^8 CFU *C. rodentium* by oral gavage or fed diet only. **(A)** Lengths of colons on day 8 or dpi 8 analyzed by histopathology in **Figures 1 F-H** and **Supplemental Figures 3.3.1 B,C**. Data shown represents two pooled independent experiments (n=4-5 mice per group). **(B)** Categorial scores for colon histopathology for hyperplasia, epithelial damage, mononuclear cell infiltration and neutrophil inflammation/crypt abscesses. Data shown represents two pooled independent experiments (n=4-5 mice per group). **(C)** Thickness of mucosal layer and central muscularis layer of colons analyzed by histopathology. Data shown represents two pooled independent experiments (n=4-5 mice per group).**(D)** Absolute body mass over 6-8 day dietary regimen or infection of mice fed CID or IRD. Gold asterisks indicate comparisons between CID and IRD. Red asterisks indicate comparisons between CID + *C.r.* and IRD + *C.r.* . Data shown represents four pooled independent experiments (n=14-22 mice per group). **(E)** Average daily food consumption over 8 day period of dietary regimen or infection. Data shown represents two pooled independent experiments (n=9-12 mice per group). Data represent mean ±SEM. **P*<0.05, ***P*<0.01, ****P*<0.001, *****P*<0.0001. Related to **Figure 3.3.1**

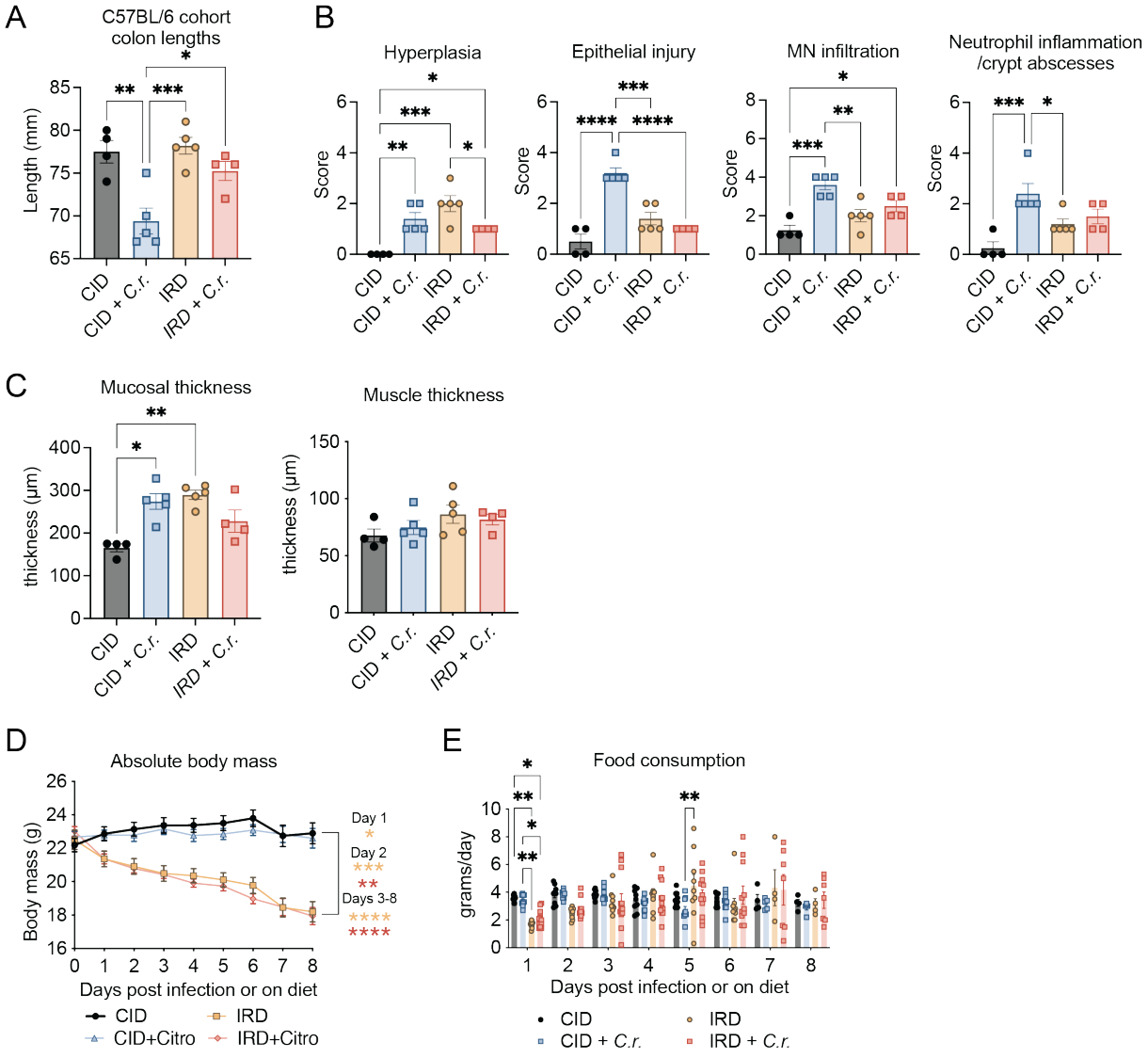
A
C57BL/6 cohort colon lengths
Length (mm)
CID
CID + C.r.
IRD
IRD + C.r.
B
Hyperplasia
Epithelial injury
MN infiltration
Neutrophil inflammation /crypt abscesses
Score
C
Mucosal thickness
Muscle thickness
thickness (µm)
D
Absolute body mass
Body mass (g)
Days post infection or on diet
Day 1
Day 2
Days 3-8
CID
IRD
CID+Citro
IRD+Citro
E
Food consumption
grams/day
Days post infection or on diet
CID
CID + C.r.
IRD
IRD + C.r.

Supplemental Figure 3.3.2 Iron rich diet alters basal and infection-induced inflammatory gene expression in colon

Six-week old C57BL/6 males were provided control iron diet (CID) or 2% carbonyl iron diet (IRD) and infected with 2.9-4.75 x10^8 CFU *C. rodentium* by oral gavage or fed diets only. **(A-D)** Gene expression analyses in proximal and distal colons from *C.r.*-infected and uninfected mice fed CID or IRD for 8 days: (**A)** *C.r.*-specific sigma factor (*rpoD);* **(B)** locus of enterocyte effacement (LEE) virulence genes (*map, tir,* espA) and non-LEE (*espI*) encoded virulence genes; **(C)** host innate inflammatory signaling genes and **(D)** antimicrobial peptide genes. Gene expression was normalized to host *Rps17* expression. Data shown represents one independent experiment (n=5 per group). Data represent mean ±SEM. **P*<0.05, ****P*<0.001, *****P*<0.0001. Related to **Figure 3.3.2**

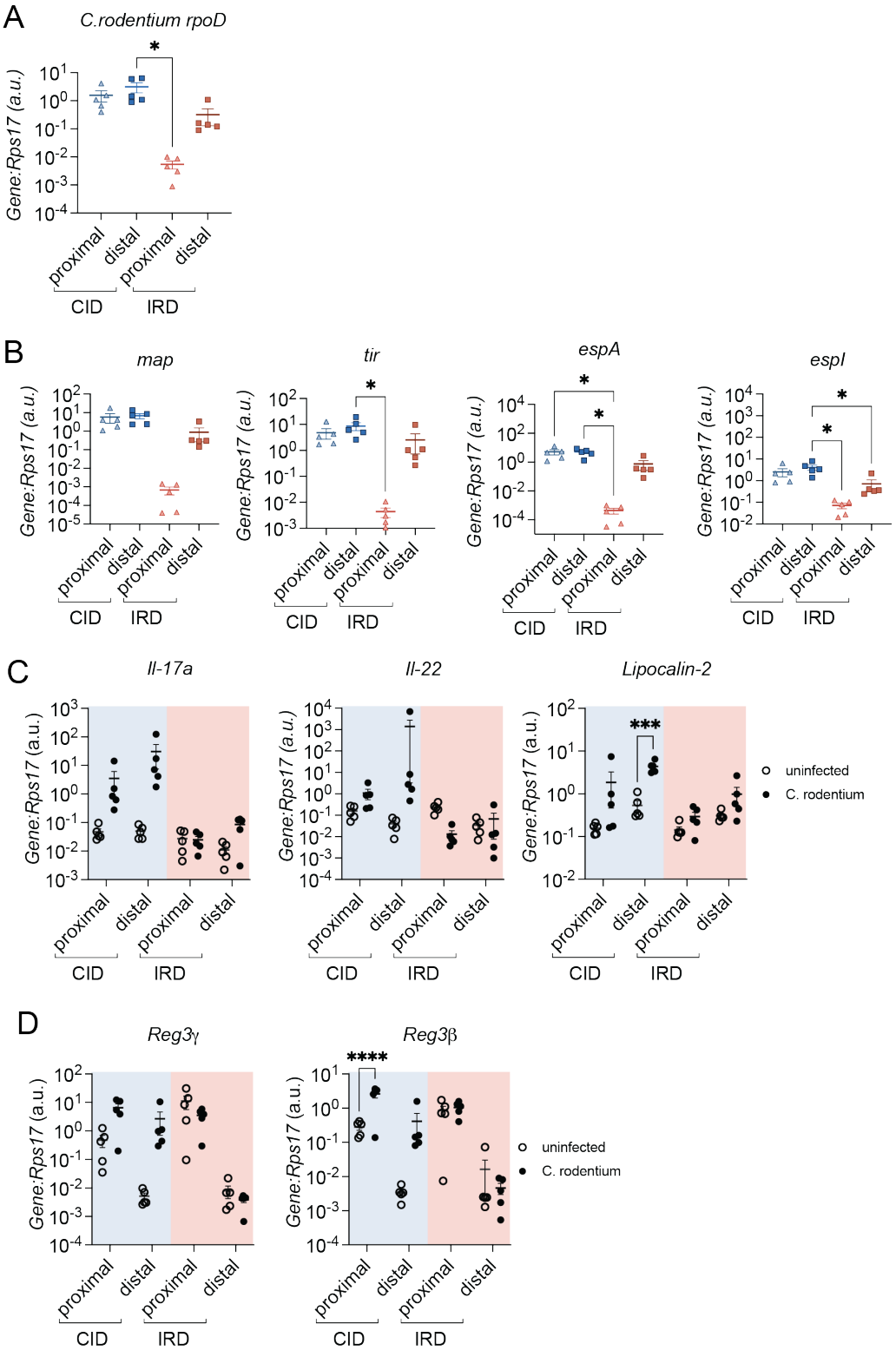
A
C.rodentium rpoD
Gene:Rps17 (a.u.)
proximal
distal
proximal
distal
CID
IRD
B
map
tir
espA
espI
C
Il-17a
Il-22
Lipocalin-2
uninfected
C. rodentium
D
Reg3γ
Reg3β

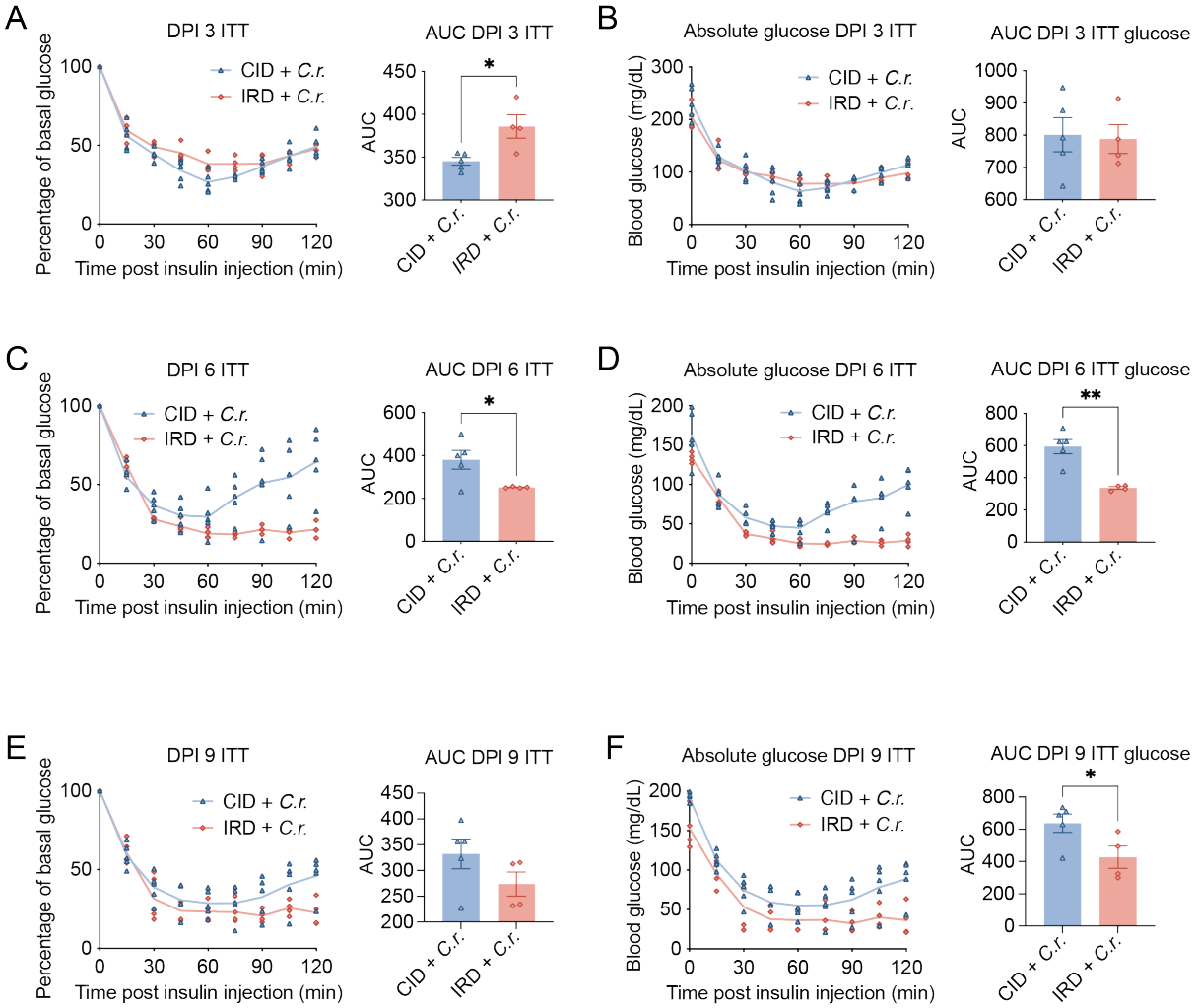

Supplemental Figure 3.3.3 Dietary iron supplementation does not influence insulin sensitivity during *C. rodentium* infection

(A-F) Insulin tolerance tests performed on six-week old C57BL/6 mice infected with $6.55x10^8$ CFU *C. rodentium* by oral gavage and fed control iron diet (CID) or 2% carbonyl iron diet (IRD). **(A,C,E)** ITT glucose values and area under the curve (AUC) analyses for glucose normalized to baseline glucose and (**B,D,F**) absolute glucose values for ITT performed on (**A, B)** dpi 3, **(C, D)** dpi 6 and **(E, F)** dpi 9. Data shown represents one independent experiment (n=4-5 mice per group). Data represent mean ±SEM. **P*<0.05. , ***P*<0.01.

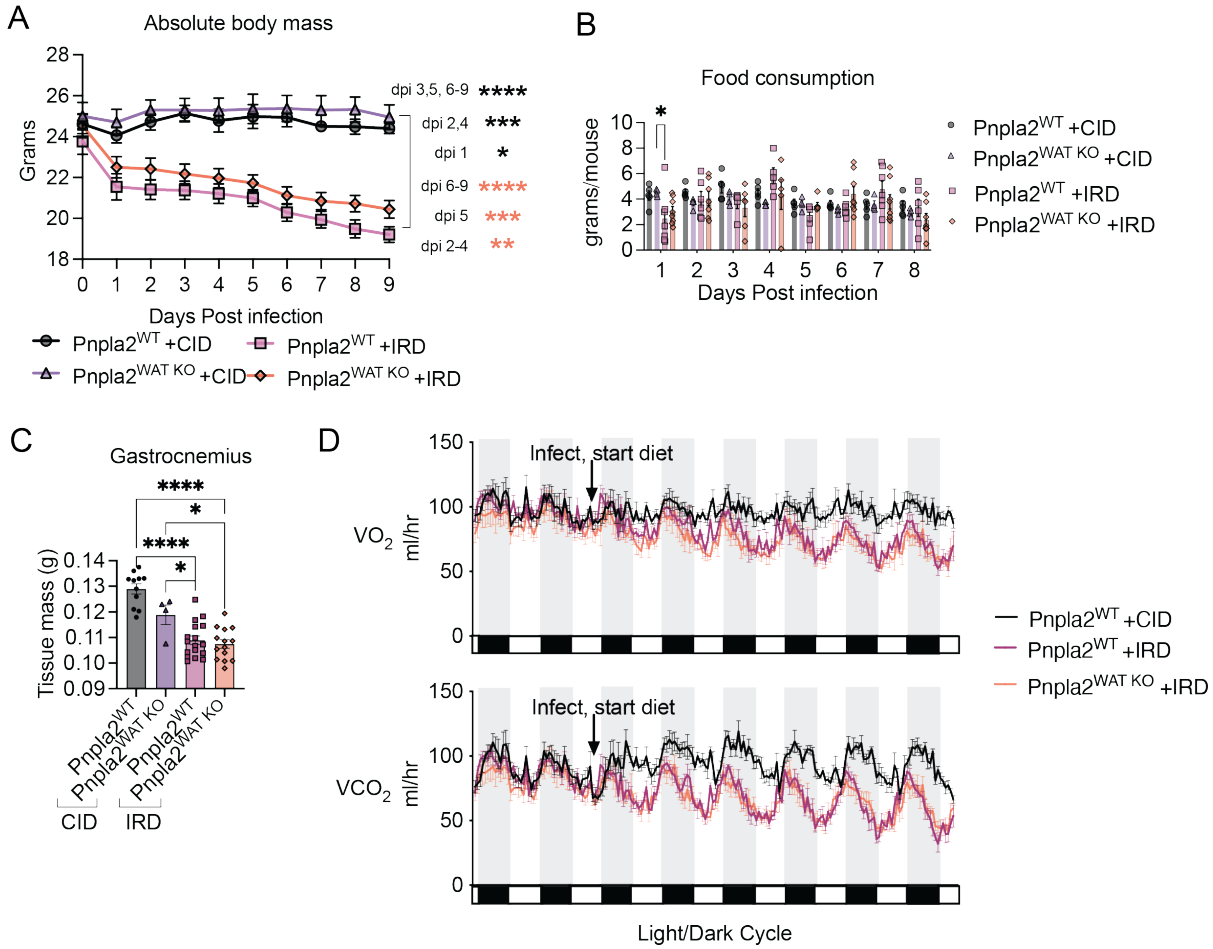

Supplemental Figure 3.3.4 Adipose-specific ATGL does not influence net energy balance during *C. rodentium* infection

Littermate *Pnpla2* x Fabp4 cre- (Pnpla2^{WT}) and *Pnpla2* x Fabp4 cre+ (Pnpla2$^{WAT\ KO}$) males between six and eight-weeks old were provided control iron diet (CID) or 2% carbonyl iron diet (IRD) and infected with 3.58-6.3x10^{8} CFU *Citrobacter rodentium* by oral gavage. Food consumption and body mass was measured daily. **(A)** Absolute body mass over 9 day infection period of Pnpla2^{WT} and Pnpla2$^{WAT\ KO}$ mice fed CID or IRD. Black asterisks indicate comparisons between Pnpla2^{WT} fed CID or IRD. Orange asterisks indicate comparisons between Pnpla2$^{WAT\ KO}$ fed CID or IRD. Data shown represent three pooled independent experiments (n=4-12 mice per group). **(B)** Average daily food consumption over 9 day infection period. Data shown represents two pooled independent experiments (n=4-8 mice per group). **(C)** Gastrocnemius muscle mass from hindlimb on dpi 6. Data shown represents two pooled independent experiments (n=4-17 mice per group). **(D)** Average hourly gas exchange volumes of O_2 consumed and CO_2 respired. VO_2 and VCO_2 rates were used to calculate RER in **Figure 3.3.4J**. Data shown represent one independent experiment (n=4 mice per group)**.** All CLAMS data plotted in zeitgeber time. White/black boxes on X axis represent 12-hr light/dark cycles of 24-hr day. Data represent mean ±SEM. **P*<0.05, ***P*<0.01, ****P*<0.001, *****P*<0.0001. Related to **Figure 3.3.4**

Supplemental Figure 3.3.5 Adipose-specific ATGL does not influence anti-virulence defenses

Littermate *Pnpla2* x Fabp4 cre- ($Pnpla2^{WT}$) and *Pnpla2* x Fabp4 cre+ ($Pnpla2^{WAT\ KO}$) males between six and eight-weeks old were provided control iron diet (CID) or 2% carbonyl iron diet (IRD) and infected with 3.58-6.3x10^8 CFU *C. rodentium* by oral gavage. RNA was extracted from colons harvested on **(A)** dpi 9 or **(B)** dpi 6 and used for gene expression analyses via quantitative real time PCR. **(A)** Expression of *C. rodentium* locus of enterocyte effacement (LEE) virulence genes (*map, tir,* espA) and non-LEE (*espI*) encoded virulence gene normalized to host *Rps17* expression. Data shown represents two pooled independent experiments (n=4-8 mice per group). **(B)** Expression of *C. rodentium* LEE virulence genes (*map, tir,* espA) and non-LEE (*espI*) encoded virulence gene in proximal and distal colons of infected $Pnpla2^{WT}$ and $Pnpla2^{WAT\ KO}$ mice fed CID or IRD on dpi 6. Gene expression was normalized to host *Rps17* expression. Data shown represents two pooled independent experiments (n=3-4 mice per group). Data represent mean ±SEM. **P*<0.05, ***P*<0.01, ****P*<0.001. Related to **Figure 3.3.5**

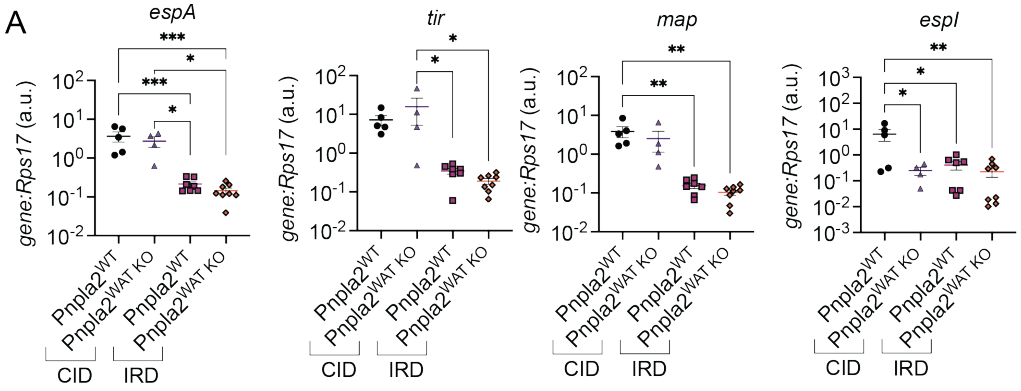
A
espA
tir
map
espI
gene:Rps17 (a.u.)
Pnpla2WT
Pnpla2WAT KO
CID
IRD

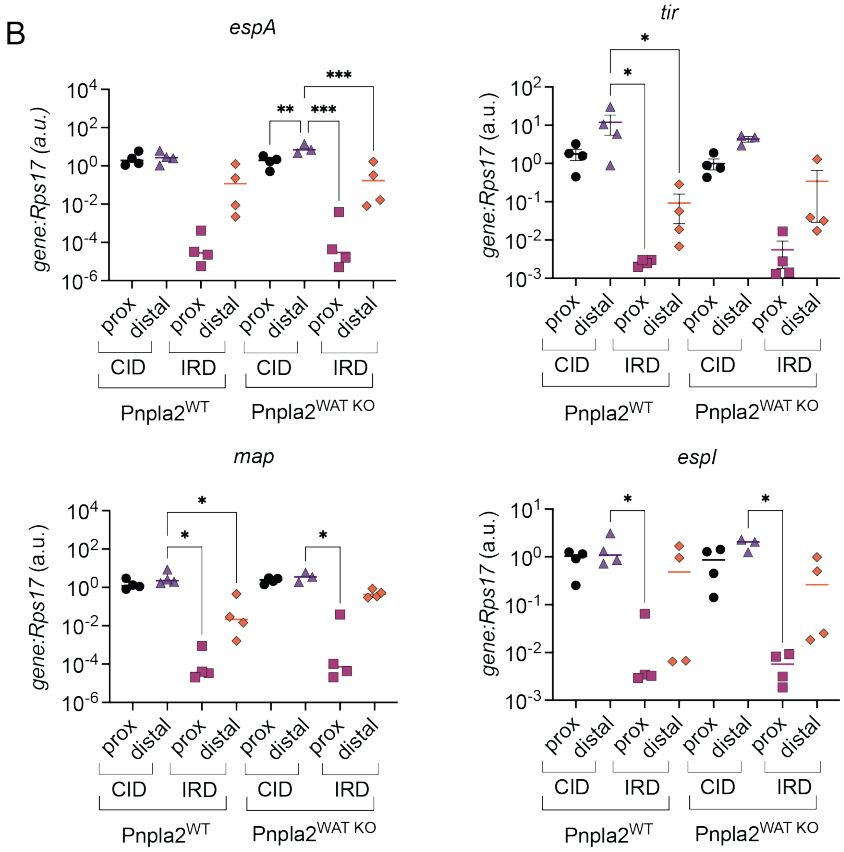
B
espA
tir
map
espI
gene:Rps17 (a.u.)
prox
distal
CID
IRD
Pnpla2WT
Pnpla2WAT KO

Supplemental Figure 3.3.6 Adipose-specific ATGL does not influence expression of innate inflammatory signaling cascade during *C. rodentium* infection
Littermate *Pnpla2* x Fabp4 cre- ($Pnpla2^{WT}$) and *Pnpla2* x Fabp4 cre+ ($Pnpla2^{WAT\ KO}$) males between six and eight-weeks old were provided control iron diet (CID) or 2% carbonyl iron diet (IRD) and infected with 3.58-6.3x10^8 CFU *C. rodentium* by oral gavage. RNA was extracted from colons harvested on **(A, B)** dpi 9 or **(C, D)** dpi 6 and used for gene expression analyses via quantitative real time PCR. **(A, B)** Expression of **(A)** host innate inflammatory signaling genes and **(B)** antimicrobial peptide genes in colons of infected $Pnpla2^{WT}$ and $Pnpla2^{WAT\ KO}$ mice fed CID or IRD on dpi 9. Gene expression was normalized to host *Rps17* expression. Data shown represents two pooled independent experiments (n=4-8 mice per group). **(C, D)** Expression of **(C)** host innate inflammatory signaling genes and **(D)** antimicrobial peptide genes in proximal and distal colons of infected $Pnpla2^{WT}$ and $Pnpla2^{WAT\ KO}$ mice fed CID or IRD on dpi 6. Gene expression was normalized to host *Rps17* expression. Data shown represents two pooled independent experiments (n=3-4 mice per group). Data represent mean ±SEM. **P*<0.05, ***P*<0.01, ****P*<0.001, *****P*<0.0001. Related to **Figure 3.3.5.**

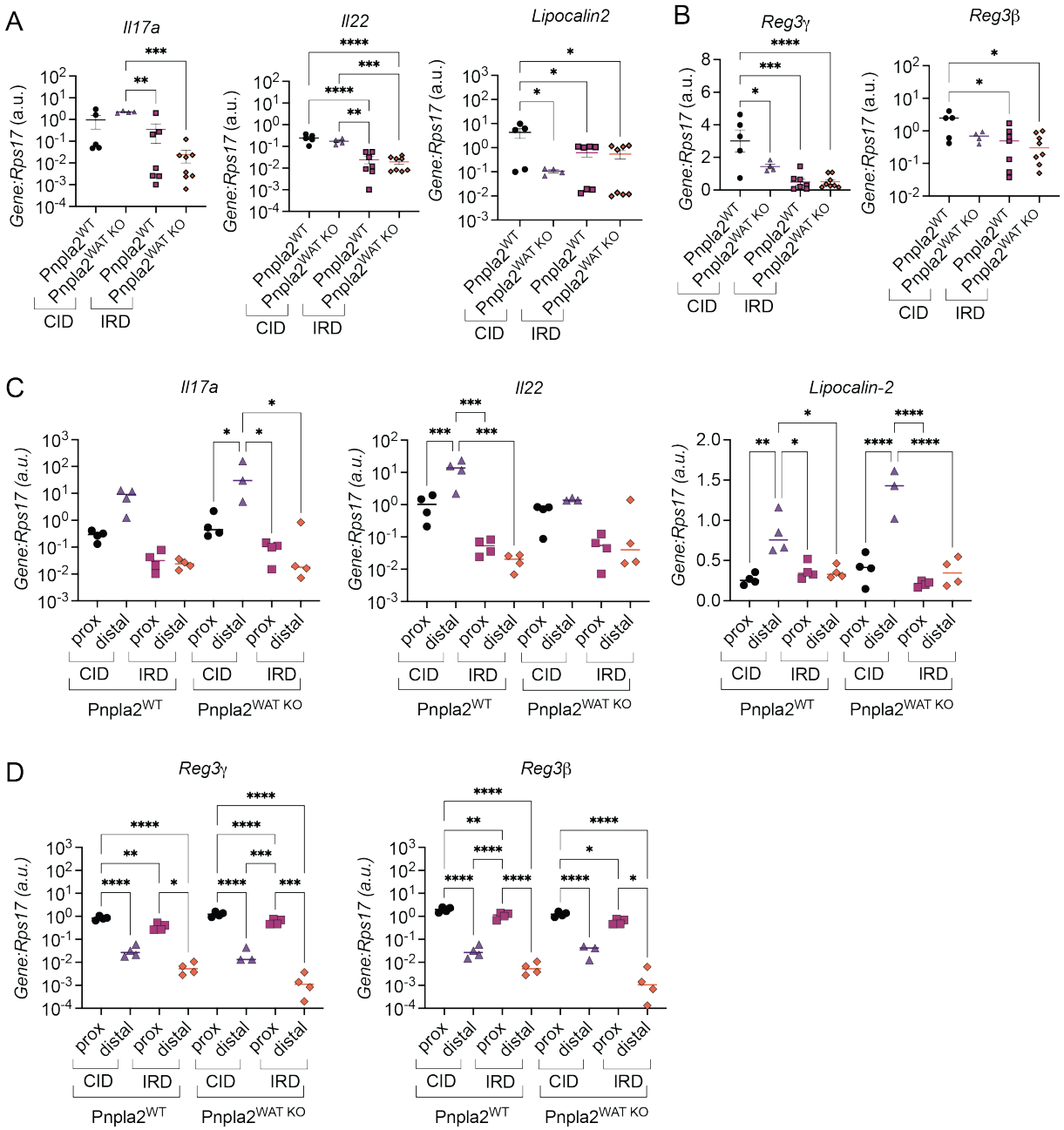
A
Il17a
Il22
Lipocalin2
B
Reg3γ
Reg3β
Gene:Rps17 (a.u.)
Pnpla2WT
Pnpla2WAT KO
CID
IRD
C
Il17a
Il22
Lipocalin-2
prox
distal
Pnpla2WT
Pnpla2WAT KO
D
Reg3γ
Reg3β

Supplemental Figure 3.3.7 Adipose-specific ATGL prevents *C. rodentium*-induced colonic remodeling

(A) Lengths of colons from uninfected Pnpla2^{WT} and Pnpla2$^{WAT\ KO}$ mice fed CID or IRD. Data shown represents four pooled independent experiments (n=6-13 mice per group). Colons were harvested from mice fed CID or IRD for 3, 6, 7, or 9 days. **(B-D)** Littermate *Pnpla2* x Fabp4 cre- (Pnpla2^{WT}) and *Pnpla2* x Fabp4 cre+ (Pnpla2$^{WAT\ KO}$) males between six and eight-weeks old were provided control iron diet (CID) or 2% carbonyl iron diet (IRD) and infected with 6.8 x10^{8} CFU *C. rodentium* by oral gavage. **(B)** Lengths of colons from dpi 6 analyzed by histopathology in **Figures 3.3.6 F-I** and **Supplemental Figures 3.3.7 C,D**. **(C)** Categorial scores for colon histopathology for hyperplasia, epithelial damage, mononuclear cell infiltration and neutrophil inflammation/crypt abscesses. Data shown represents one independent experiment (n=3-5 mice per group). **(D)** Thickness of mucosal layer and central muscularis layer of colons analyzed by histopathology. Data shown represents one independent experiment (n=3-5 mice per group). Data represent mean ±SEM. **P*<0.05, ***P*<0.01, ****P*<0.001. Related to **Figure 3.3.6.**

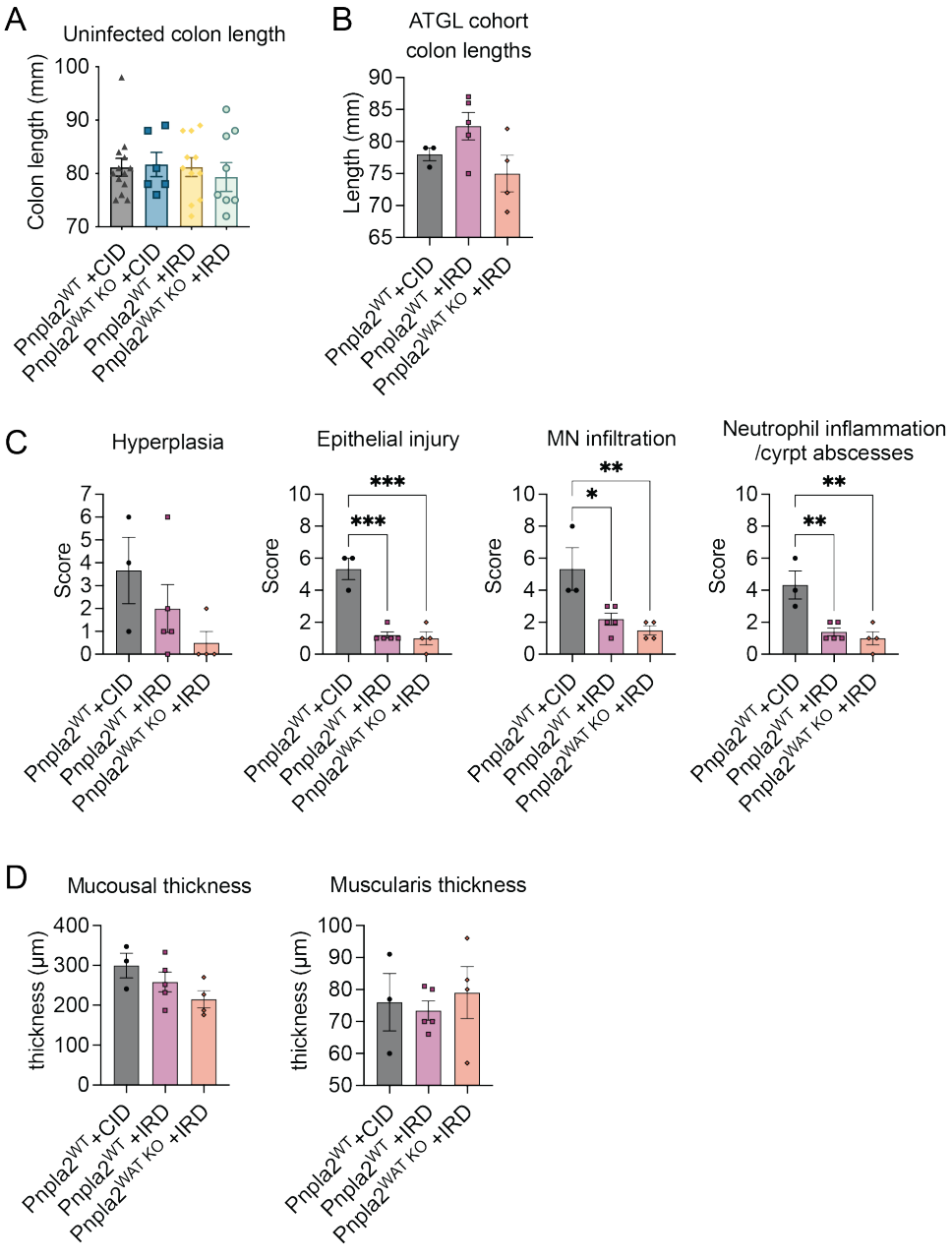
A
Uninfected colon length
Colon length (mm)
100
90
80
70
Pnpla2WT +CID
Pnpla2WAT KO +CID
Pnpla2WT +IRD
Pnpla2WAT KO +IRD
B
ATGL cohort
colon lengths
Length (mm)
90
85
80
75
70
65
Pnpla2WT +CID
Pnpla2WT +IRD
Pnpla2WAT KO +IRD
C
Hyperplasia
Epithelial injury
MN infiltration
Neutrophil inflammation
/cyrpt abscesses
Score
***
**
*
Pnpla2WT +CID
Pnpla2WT +IRD
Pnpla2WAT KO +IRD
D
Mucousal thickness
Muscularis thickness
thickness (µm)
400
300
200
100
0
90
80
70
60
50
Pnpla2WT +CID
Pnpla2WT +IRD
Pnpla2WAT KO +IRD

Chapter 4: Conclusion and Closing Remarks

4.1 Conclusion and Closing Remarks

The irony of research in biology is that while any given component of life can appear miniscule and inconsequential in the landscape of a biological system, said component is either directly or tangentially linked to every other component of a biological system through a few degrees of relationships. The scientific process allows us to uncover and describe concealed relationships that in turn, enable the discovery of more. My goal as a trainee aimed to uncover one such relationship by disrupting a small component of a biological system and highlighting the indisputable significance of said component in the function of a biological system. In this regard, my thesis work reexamined the causality of iron in modulating 1) organismal metabolism and 2) host defenses during an enteric infection. My work identified a mechanism for physiological and metabolic changes induced by dietary iron supplementation and corresponding effects on host defense and pathology during an enteric infection in mice. But of equal importance, this work has raised numerous questions regarding the etiology of disease pathology during infection, and the phenomena of non-inflammatory organ remodeling as a host defense response.

In Chapter 2, we describe the relationship linking iron metabolism to nutrient absorption and organismal energy balance. In unchallenged mice, we found that adipose triglyceride lipase (ATGL) mediates lipolysis and fat wasting in response to dietary iron-induced negative energy balance. We demonstrated that dietary iron overload causes negative energy balance in mice by disrupting nutrient absorption and a lack of adipose-specific ATGL leads to increased lean wasting and cachexia. We utilized this system of iron-mediated negative energy balance in Chapter 3 to explore the consequences and role of iron-induced lipolysis during an enteric infection with *Citrobacter rodentium* and found a

surprising role for iron in host defense and the etiology of colitis itself. Contrary to the historical view that iron exacerbates negative outcomes of infection, we found that dietary iron supplementation enhances resistance defenses against *C. rodentium* and protects mice from infectious colitis and inflammation. In investigating the role of iron-induced fat wasting and lipolysis in this phenotype, we found that iron affords protection from disease through two independent routes that span antagonistic and cooperative defenses. First, iron supplementation promotes antagonistic defenses during *C. rodentium* infection by disrupting colonization and expansion of *C. rodentium*—presumably through direct or indirect modulation of the gut microbiota which promotes colonization resistance. Reduced burden and expansion of *C. rodentium* dampens the induction of inflammatory cascades and mucosal damage in the colon, protecting from infection-induced colitis. However, we found that iron-induced fat wasting is dispensable in promoting resistance defenses against *C. rodentium*. We were surprised to discover that iron-induced lipolysis protects mice from non-inflammatory colon remodeling, including colon shortening and distal muscularis thickening—features that have been traditionally coupled to inflammation and mucosal damage observed during infectious colitis. Thus, this work describes a mechanism for iron in modulating host physiology and reveals a novel adipose-gut axis in host defense against enteric infection.

In summary, this thesis work expands on the traditional role for iron in metabolism and host defenses, demonstrating that iron can be beneficial and protect from pathology during an infection. Further, we have dissociated inflammation from non-inflammatory colon remodeling in infectious colitis and shown that inflammation and mucosal damage are dependent on the expansion of *C. rodentium* during infection. As colon remodeling occurs in

the presence of *C. rodentium* and is ablated by iron-induced fat wasting, we have revealed a novel axis between adipose tissue and colon ultrastructure.

As our findings overlap with current knowledge and span novel territory in the etiology of colitis, we look forward to future investigations of iron and adipose tissue in modulating host defense outside the traditional context of antagonism and nutritional immunity. We hope that an extension of this thesis work may address the following questions:

In regards to iron-induced resistance: Does iron supplementation promote resistance through enhancing colonization resistance? And does Reg3 induction, iron-induced intestinal damage, or iron content itself alter microbiome composition or promote colonization resistance?

In regards to colon remodeling and adiposity: How does an infectious agent induce non-inflammatory remodeling of organs? Does non-inflammatory organ remodeling serve a beneficial function in host defense? Does this phenomena exist in other sites of disease and in the context of other infections? Does adiposity contribute to the signal for organ modeling or do endogenous lipolysis products reduce the signal for or induction of organ remodeling?

Altogether, the most exciting finding of this work lies in the phenomena of infection-induced, non-inflammatory organ remodeling. The implications of which contribute to the idea that infectious disease modulates biological systems independent of traditional inflammatory signaling cascades. Thus, infection-induced organ remodeling is presumably mediated

through pathways that are currently implicated in other disease contexts. The overlap of such systems with infectious challenge has widespread implications for the etiology of both infectious and non-infectious disease pathology. Further, the existence of such relationships adds another potential role for the microbiome in health and development—for instance, our finding essentially shows that a microbe can promote colon remodeling. Thus, it is not a stretch to imagine that other members of the normal flora influence organ form and structure, including skin and other regions of the gastrointestinal tract. Of course, this phenomena has been demonstrated in invertebrates, like the Hawaiian bobtail squid, where specific phenotypic variants of *Vibrio fischeri* are selected to colonize the light organ and enable development of juvenile to adult squid. Of note, our work does not address how colon remodeling affects the function of the gastrointestinal system, the long-term consequences or if it is reversible. We propose that such a striking change in structure is likely to affect function and contribute to host defenses. As adiposity is related to colon remodeling, we also posit that fat tissue and/or lipid metabolism may also be involved with development or structure of peripheral organs during disease. It will be exciting to witness the progression of this work and related phenotypes in mammalian systems. We have uncovered a glimpse of a striking biological phenomena serendipitously through modulation of the micronutrient iron—which shows that novel systems and relationships await discovery even in well-trodden biological paths.